Public of Iraq
Ministry of Higher Education & Scientific Research
Middle Technical University
Engineering Technical College – Baghdad

Investigation of Solar-Driven PV Cooling and Brackish Water Membrane Desalination

A Thesis Submitted to

The Council of the Middle Technical University, Engineering Technical College-Baghdad, in a Partial Fulfillment of the Requirements for the Master's Degree of Technology in Thermal Engineering Technology

By

Hussian A. Abdul Kareem

Supervised by

Dr.Abdul Hadi N. Khalifa	**Dr.Ahmed J. Hamad**
Prof.	**Prof.**
July	Dhu al-Hijjah
2023	1444

بِسۡمِ ٱللَّهِ ٱلرَّحۡمَٰنِ ٱلرَّحِيمِ

وَقُل رَّبِّ أَدۡخِلۡنِى مُدۡخَلَ صِدۡقٍ وَأَخۡرِجۡنِى مُخۡرَجَ صِدۡقٍ وَٱجۡعَل لِّى مِن لَّدُنكَ سُلۡطَٰنًا نَّصِيرًا

صدق الله العظيم

سورة الاسراء اية (80)

SUPERVISOR CERTIFICATION

We certify that this thesis was prepared under our supervision in partial fulfillment of requirements for the degree Master of Technology in Thermal Engineering Technology.

Signature:	Signature:
Name: ***Dr. Abdulhadi N. Khalifa***	Name: ***Dr. Ahmed Jasim Hamad***
Professor	***Assist. Professor***
Date: / / 2023	Date: / / 2023

Linguist Certification

I certify that I have read this thesis entitled " **INVESTIGATION OF SOLAR-DRIVEN PV COOLING AND BRACKISH WATER DESALINATION** " by" **Hussian A. Abdul Kareem**" and I examined the language of the thesis; in my opinion, it is adequate as a thesis for degree Master of in thermal engineering technology.

Signature:

Name: ***Mouayed Hassan Ziada AL-Toki***
Title: ***Lecturer***
Date: / / 2023

Signature:

Name: ***Dr. Hameed A. Hussien***

Title: ***Professor***

(Head of the Engineering Power Mechanics Department)

Date: / / 2023

In view of the available recommendation, I forward this thesis for debate by the Examining Committee.

Signature:

Name: ***Dr. Sabah Khammass Hussein***

Title: ***Professor***

Deputy Dean for Scientific Affairs and Postgraduate Studies

Date: / / 2023

COMMETTE CERTIFICATION

We certify that we have read this thesis entitled" **INVESTIGATION OF SOLAR-DRIVEN PV COOLING AND BRACKISH WATER DESALINATION "** by " **Hussian A. Abdul Kareem**" and, as an Examining Committee, examined the student in its contents and that in our opinion, it meets the standard of a thesis for The **Master Degree** of in Thermal Engineering Technology.

Chairman

Signature:

Name: ***prof. Dr.Qasim Saleh Mahdi***

Date: / / 2023

Member	**Member**
Signature :	Signature
Name : ***Dr.Fawziea M.Hussien***	Name: ***DR.Hussein M. Sadeq***
Date: / / 2023	Date: / / 2023

Supervisor

Signature:	Signature:
Name: ***Dr. Abdul Hadi N Khalifa***	Name: ***Dr. Ahmed Jasim Hamad***
Professor	***Assist. Professor***
Date: / / 2023	Date: / / 2023

The dean

Signature:

Name: ***Dr. Nabil J. Yasin***

Professor

(Dean of the Engineering Technical College – Baghdad)

Date: / /2023

DEDICATION

To my mother

To my father

To my Brother

To my Sister

Hussian A. Abdul Kareem

2023

ACKNOWLEDGEMENTS

In the name of Allah the Merciful

First, thank God. I want to commend and thank the mighty God. My sincere gratitude and thanks go to my first supervisor, **Prof. Dr. Abdul Hadi N**. **Khalifa**, my second father. It was my inspiration and motivation during the hard times I went through. He taught me the love of life, tolerance, and the aspiration for the best, and his guidance and advice significantly impacted producing this research in the best way and content. The enthusiasm and encouragement he gave me during the study and his support of this study, and thanks to him, I completed this thesis. I appreciate his patience and humanity while writing and reviewing this study.

I sincerely thank the supervisor, **Dr.Ahmed Jassim**; he was my inspiration and motivation during the difficult time and the encouragement he gave me in studying. I appreciate your patience and humanity while writing and reviewing this study.

I want to thank my professors at the college for being a supportive group, especially **Dr. Johain Jawdet Faraj**. And **Dr.Fawziea Huseien.**

I would particularly like to thank **Mr. Thabet Jamel and Mr. Maula** Twoma, who have given me most of their science.

My thanks and appreciation to the Deanship, the teaching staff, and the staff of the Technical College _ Baghdad

Hussian A. Abdul Kareem

2023

ABSTRACT

Solar panels are usually cooled passively without taking advantage of the heat stored in the cell. This is one of the active methods in which the cells are cooled by water while obtaining potable water from the coolant water.

The current study consists of three steps to find the best geometry, coolant mass flow rate, and two membrane materials with different pore sizes of flow photovoltaic membrane distillation (PMD). The first step is a theoretical simulation of the PMD using COMSOL Multiphysics 5.6 software, in which a 160×160 mm solar panel is integrated with the PMD unit that consists of 7 layers, the first and the last aluminum plates, two polymers mesh, hydrophobic membrane, evaporator, and condenser layers. The space thickness, membrane thickness, fins height, fins number, and temperature of inlet water are studied to find the best geometry of the PMD. The second step is the indoor test, carried out on a small-scale rig of 165 × 140 mm solar panel with seven layers to construct the PMD rig. Five rigs are built; the first is a PV panel without a cooling system, and the other four rigs are different from each other by the pore size of the membrane. Where four pores sizes are used, such as; 0.45, 1, 3, and 5 μm. From the indoor test, the best pore size is selected. The final step is to build a full-scale solar panel integrated with the PMD unit of membrane pore size of 0.45 μm. The outdoor unit is tested under different mass flow rates of coolant water. The weather data are derived from Meteonorm V8.

It is found that the best geometry of the PMD when the space between the evaporation and membrane is 2.5 mm, the membrane thickness is 100 μm, and fin height is 20 mm, the number of fins is 5, and the best temperature of water inlet is 30 ^{o}C. The geometry of the PMD mentioned above achieved freshwater productivity of 0.651 kg/m$^{2}\cdot$h and a temperature difference between the uncooled and cooled

panels of 10 ^oC. While from the indoor test, it is found that the best membrane pore size is 0.45 μm and the best supply water flow rate is 0.865 kg/m^2h, which can produce 0.774 kg/m^2h of fresh water, and the temperature difference between the uncooled and cooled panel of 14^oC when the solar intensity is 600 W/m^2. From the outdoor test, contrary to previous studies, the current study showed that increasing the supply water flow rate leads to a rise in cell temperature and increased water productivity. The best mass flow rate of the supply water is 0.829 $kg/m^2.h$, which gives a 7 ^oC temperature difference between uncooled and cooled cells and water productivity of 0.102 $kg/m^2.h$. The maximum solar panel efficiency is at noon, equal to 15.3% for cooled panels and 9.93% for uncooled panels. The efficiency of uncooled panels decreases with the increase of solar radiation.

The deviation between the previous and current work for the membrane coefficient is about 8%. Good agreement for the cell temperature distribution with the previous work. The comparison between the theoretical results of the cell temperature with and without cooling with that of the experimental results showed a good agreement.

TALE OF CONTENTS

Chapter Four

Chapter Five

Chapter Six

NOMENCLATURE:

Symbols	Meaning	Units
A	Area of the solar cell	m^2
c_p	Specific heat capacity	kJ/kg.K
c_m	Membrane coefficient	$kg/m^2.h.pa$
C_f	Feed concentration	$kg/m^2.h$
C_{fm}	Concentration at the surface membrane	$kg/m^2.h$
dx	Element in $x-$ diraction	m
dy	Element in $y-$ direction	m
dz	Element in $z-$ diraction	m
G	Solar radiation	W/m
g	Gravity	m/s^2
h	Heat transfer coefficient by natural convection	W/m^2K
h_{in}	Enthalpy of inlet flow	kJ/kg
h_{out}	Enthalpy at outlet flow	kJ/kg
I	Output current	A
J	Vapor flux across the membrane	kg/m^2h
J_S	The bleeding water flow rate	kg/m^2 h
J_W	Source water flow rate	kg/m^2 h
J_c	clean water production rate	kg/m^2 h
k	Thermal conductivity	W/m.K
k_A	Thermal conductivity of air	W/m.K
k_f	Thermal conductivity of the fluid	W/m.K
k_m	Thermal conductivity of the membrane material	W/m.K
kn	The Knudsen number	-
l	Mean path of the water vapor molecule	m

M	The molecular weight of the water	kg/mol
$\dot{m}_{in}$	mass flow rate at the inlet flow	kg/s
$\dot{m}_{out}$	mass flow rate at outlet flow	kg/s
p	Vapor pressure	bar
P_{sat}	Vapor-saturated pressure	bar
p_{atm}	atmosphere pressure	bar
Q	Heat source	W
Q_{conv}	Convection heat transfer from the cell surface to the ambient	W
Q_h	Heat is converted into a heat flux and delivered to the thermal system	W
r	The pore size of the membrane	µm
R_o	Gas constant	kJ/mol.K
Q_{rad}	Radiation heat transfer from the cell surface to the ambient	W
T_{amb}	Temperature of ambient	K
T_{cell}	Solar cell temperature	K
T_{fm}	Feed bulk temperature (K)	K
T_{pm}	Permeate temperature	K
T_{TP}	Temperature polarization	K
t	Time	s
u	Velocity in $x-$direction	m/s
V^o	Wind speed	m/s
V	The voltage drop across the solar cell	V
v	Velocity in $y-$direction	m/s
w_1	Membrane's dry weight	kg

w_2	Membrane's wet weight	kg
W	The power produced by the solar cell	W
w	Velocity in $z - \text{diracion}$	m/s
X	liquid-phase mole fraction	-
y	Vapor-phase mole fraction	-
Z	The vapor that passes through the membrane	Kg/s
	Greek Symbol	
α	Solar absorptance	-
τ	Solar transmissivity	-
β	The intensity of the light	-
δ	The thickness of the membrane	m
ε	The emissivity of the material.	-
ϵ	Membrane porosity	-
μ	Dynamic viscosity	pa. sec
ρ	Density	kg/m^3
ρ_m	Density of membrane	kg/m^3
ρ_e	Density of ethanol	kg/m^3
φ(λ)	The wavelength of the light	-
σ	Stefan boltzmann constant	$W/m^2.K^4$
ω	Pore tortuosity	-
$\eta_{solar\ panel}$	Electricity efficiency	-

Chapter One
Introduction

Chapter One

Introduction

1.1 PREFACE

The massive consumption of fossil fuels for industrial, agricultural, transport, and electric power generation sectors, as well as due to the negative impact of burning fossil fuels on the environment through ozone layer depletion and global warming. The world has turned to search for renewable and clean energy that is environmentally friendly. Among renewable energies, solar energy, especially Photovoltaic (PV) solar systems, is the most promising alternative to conventional energy. Figure (1.1) shows an exponential increase in the installation of PV solar systems, which increased from 3.7 GW in 2005 to 750 GW in 2020. One of the reasons for the increasing installation of the PV solar system is the decrease in the price of one produced Watt from $3/W in 2013 to 1.36. $/W in 2020. A more significant reduction in 2030 is expected to reach 0.89 $/W, as shown in Figure (1.2)[1].

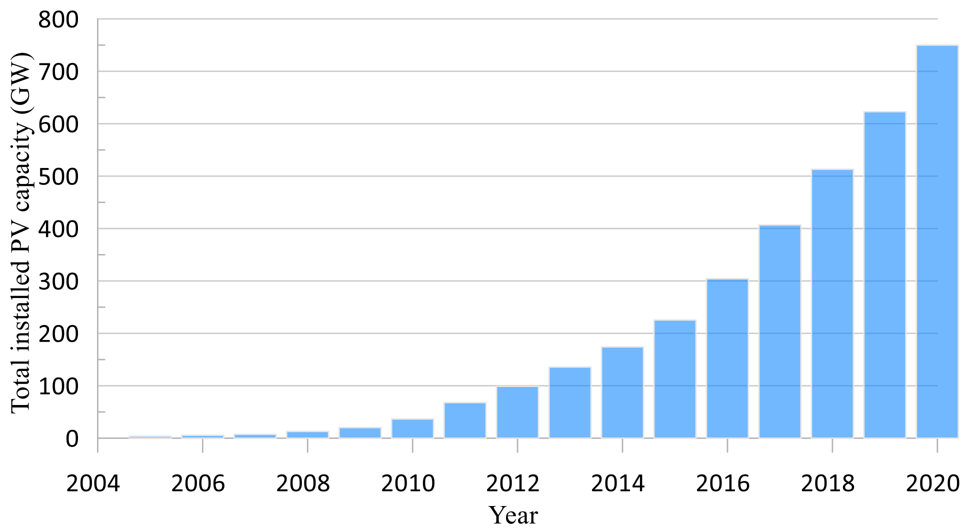

Figure (1.1): PV solar system world cumulative installed capacity[1].

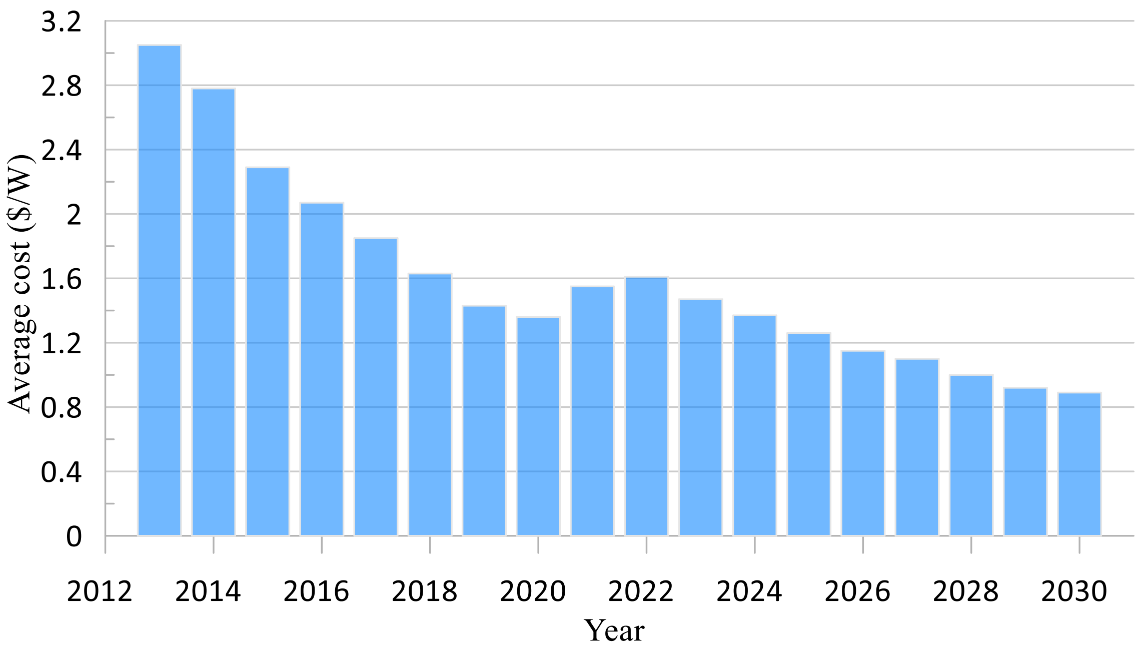

Figure (1.2): Cost of Watt produced for rooftop PV solar system [2].

1.2 EFFECT OF CELL TEMPERATURE ON THE PANEL PERFORMANCE

The conversion of solar radiation into power in solar cells is shallow and is about 14 to 18%; the rest of the solar radiation that has not been converted into energy is stored in the solar cell, leading to a rise in temperature. The high cell temperature leads to a negative impact on cell performance, reducing the cell's short life span. Figure (1.3) shows the effect of a PV panel's temperature on the panel's productivity. The figure shows a decrease in the produced power from 53.8 W at 10^{o}C to 39.8 W at 70 ^{o}C. The deviation from the standard operating conditions of the cell, the efficiency of PV panel conversion is decreased by 0.4 to 0.5% per 1 ^{o}C [2].

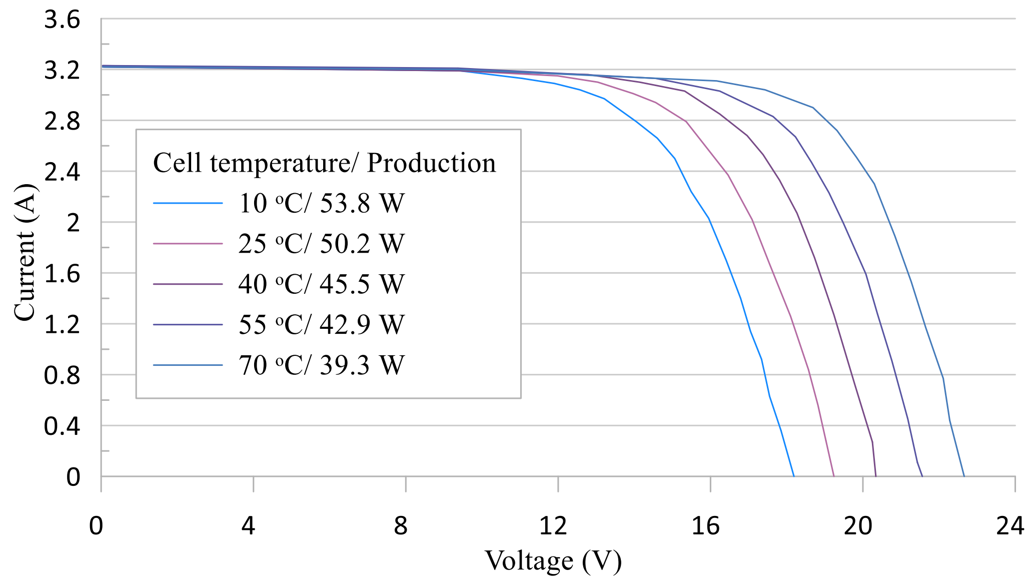

Figure (1.3): The effect of cell temperature on the characteristic of the PV panel at 1000 W/m^2 [3].

1.3 COOLING OF PV PANELS

Iraq is located in the middle east (33.2232° N, 43.6793° E); Baghdad, the capital, receives enormous solar radiation around the year; the maximum monthly solar radiation is 220 kWh/m^2 in June. The minimum is 80 kWh/m^2 in December, as shown in Figure (1.4a); the average daily sunshine duration is about 11 hrs in June and reduces to about 4hrs in December, as shown in Figure (1.4b). The minimum and maximum average daily temperatures in June are 47 ºC at noon and 28 ºC, as shown in Figure (1.4c). As mentioned above, the temperature of the PV panels in the summer in Iraq is high because of their exposure to high-intensity solar radiation for a long time and at high temperatures. The operating of PV panels at a high temperature indeed leads to a negative impact on the solar system's performance due to the high temperature of the surface of the solar panel. The problem of high cell temperature can be solved by cooling the solar cell using water, the heat withdrawn from the cell can be used to evaporate part of the cooling water, and then the vapor passes through thin membranes to condense on a cold surface. Thus the cell is cooled, and drinking water is obtained. The device that can cool the solar cell and produce freshwater is a photovoltaic-membrane distillation. The device shown in Figure (1.5) is a single-stage photovoltaic-membrane distiller consisting of multi-layers connected directly to the back panel. The first layer is a hydrophilic layer, in which salty water is pumped or sucked by the capillary force. The salty water passes through the first hydrophilic layer, cools the cells, and evaporates. The vapor produced is transported either through an air gap or a hydrophobic membrane. The passed vapor then condenses on the second hydrophilic as fresh water. Many stages can be used to cool and produce fresh water.

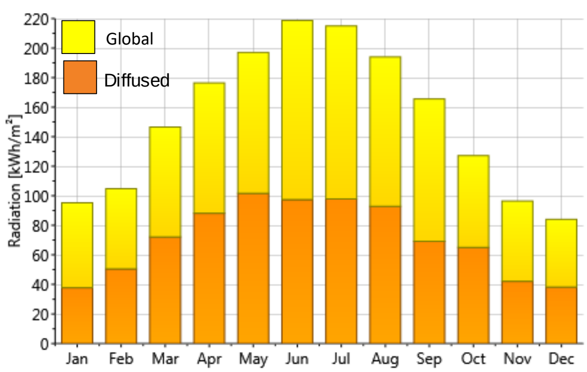

a. Monthly average Solar radiation

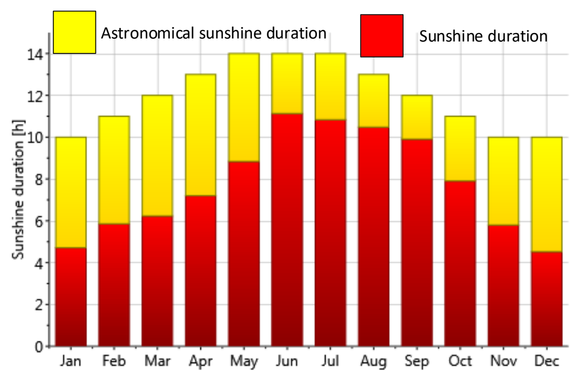

b. Daily average sunshine duration

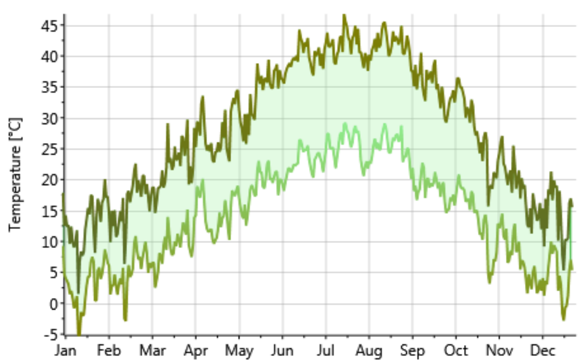

c. daily average minimum and maximum temperature

Figure (1.4): Iraqi weather data[4].

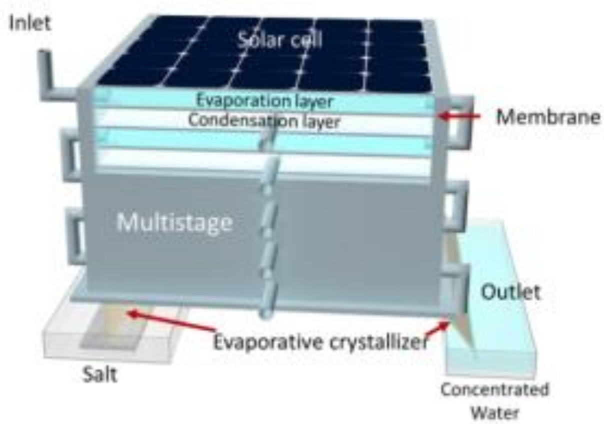

Figure (1.5): Single stage of photovoltaic-membrane distiller[5].

1.4 WATER DESALINATION METHODS

Desalinating water is a physical process in which dissolved salts are removed to convert salt water into drinkable water. Desalination is costly because of the high startup, operating, and maintenance expenses and the process's significant energy consumption. Since distillation facilities are often situated close to saltwater sources, extra payments are associated with moving and pumping desalinated water to residential areas. Multistage flash (MSF), multi-effect distillation, humidification/ dehumidification (HDH), vapor compression, freezing and melting, and solar distillation are used to produce potable water from salty water [6]. Figure (1.6) shows the types of distillation systems. Since the current work is concerned with using solar energy in water desalination, the focus will be on solar energy in water desalination in reviewing water desalination.

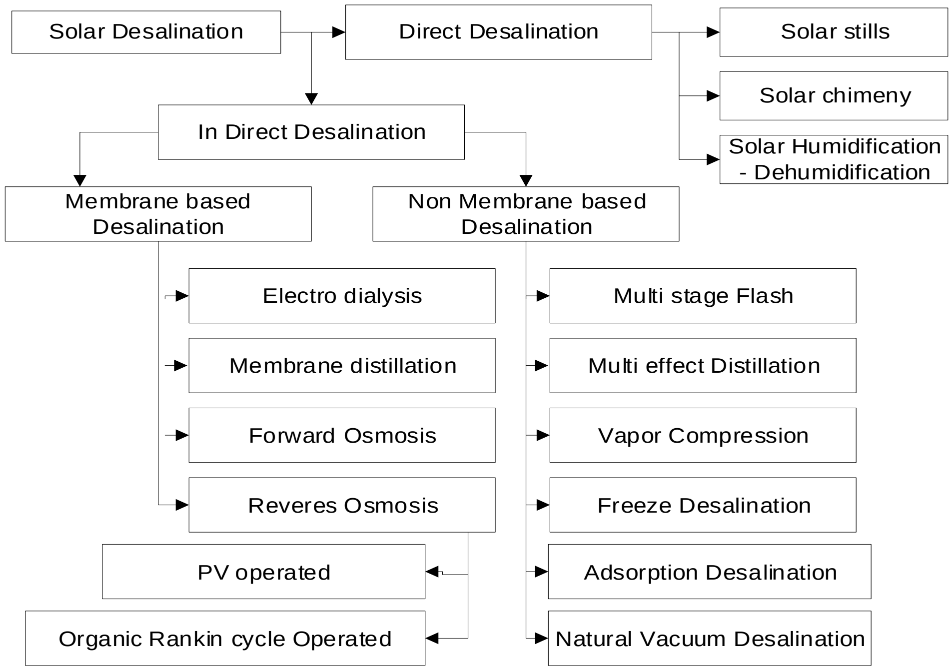

Figure (1.6): Classification of Solar Desalination Systems [7].

1.5 SOLAR DISTILLATION

In the solar distillation process, solar energy is directly used to heat the salty water and evaporates the water. The vapor is then forced to condense on a cold surface. In another technology, the vapor is separated from water using a membrane called membrane distillation (MD). MD comes from membrane contactors, which provide non-dispersive contact through microporous membranes with significant interfacial area for gas/liquid or liquid/liquid contacting activities[8]. Compared to traditional methods carried out in towers, columns, or mixer-settlers, membrane contactors promise to give a considerable process intensification for separation processes, including absorption, liquid-liquid extraction, and distillation[9]. Water vapor is passed across a membrane during membrane distillation, where the water on the other side has a lower partial pressure and evaporates through the membrane. [10]. The Solar driven membrane distillation system is classified as shown in Fig (1-6).

1.5.1 Membrane Distillation Systems

Membrane distillation (MD) is a thermal process; the main driving force across the membrane is the pressure difference between the two sides of the membrane. A waterproof membrane uses a continuous water supply without penetrating through the microporous membrane. When the system is exposed to heat, the water evaporates, penetrates through the porous membrane, and condenses on a specific surface on the second side of the membrane, as shown in Figure (1.7).

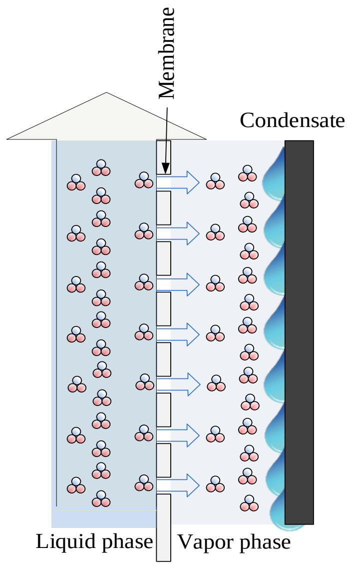

Figure (1.7): Membrane distillation process [11].

Flat sheet and hollow fiber membranes are the two kinds of membrane structures used in MD. Hollow fiber membranes often have a lower flux while having a larger specific surface area than flat sheet membranes owing to their poor flow dynamics [12]. The dual-layer hydrophilic-hydrophobic fibers, for example, are high-flux hollow fiber membranes due to recent advancements[13]

Depending on the cold side, MD is divided into four basic types, namely, direct contact membrane distillation (DCMD), air gap membrane distillation

(AGMD), feed gap membrane distillation (FGMD), and feed gap air gap membrane distillation (FGAGMD), as shown in Figure (1.8).

1.5.1.1 Direct Contact Membrane Distillation(DCMD):

Although the energy efficiency of DCMD is low, it is the most widely used because of its ease of design and operation. In DCMD, the microporous membrane separates the flow of the hot liquid from the cooled permeate, and the flow between the two fluids is opposite, as in Figure (1.8a). The temperature difference between the hot and the cold fluid is the catalyst that drives the steam to move from the hot side to the cold side through the microporous membrane and then condenses on entering the permeate stream. This type is suitable when the water salinity is low and characterized by increased fluid flow due to the low membrane resistance to flow since the number of barriers is small [14].

1.5.1.2 Air Gap Membrane Distillation(AGMD):

In the AGMD, the coolant is separated from the distillate channel by a thin layer of polymer. The heat recovery inside the AGMD is achieved when the feed solution is used to cool the condensation layer, as shown in Figure (1.8b). The heat transfer coefficient in this type is low due to the air gap, which adds additional thermal resistance to the heat transfer, leading to a delay in water evaporation due to impeding heat transfer, thus reducing the productivity of drinking water compared to the DCMD. In the AGMD, a vacuum can be used to control the diffusion molecular of air or/ and separate the air at low pressure to drain the distillate water altogether [15].

1.5.1.3 Feed Gap Membrane Distillation (FGMD):

In the FGMD, the feed solution passes through the last air gap. The polymer film separates the heating solution into the former coolant channel from the feed solution. On the membrane's cold side, the permeate is also circulated as coolant, and the vapors condense in the coolant channel in identification with the DCMD, as shown in Figure (1.8c). FGMD, as in the DCMD, suffers from the internal recovery of the heat due to the low vapor pressure and, thus, the need for an external heat exchanger to recover the lost heat from the channel outlet [16].

1.5.1.4 Feed Gap Air Gap Membrane Distillation (FGAGMD):

The FGAGMD permeate channel is separated from the cooling stream, and the heating stream is separated from the solution, as shown in Figure (1.8d). The heat transfer coefficient in this configuration is very low due to adding two polymer layers. The transfer of the sensible heat from both FGMD and FGAGMD configurations depends on the temperature and physical properties of the feed solution, as well as on the flow rate of the feed solution. Suppose this exiting heat is to be recovered. In that case, this must be considered in the overall system design of a potential FGMD or FGAGMD system.

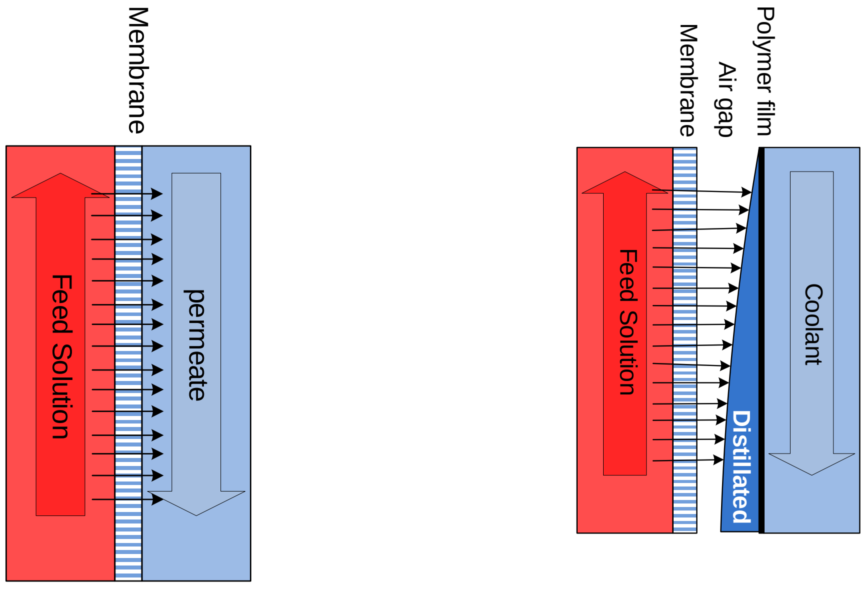

a. DCMD b. AGMD

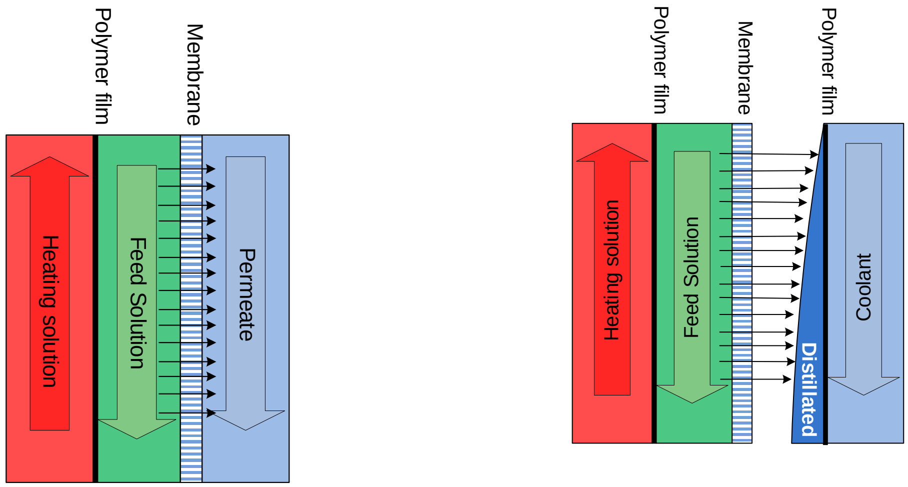

c. FGMD d. FGAGMD

Figure (1.8): MD configurations [17]

1.5.2 Membrane Characteristics:

Generally speaking, the membrane utilized in the MD system should have low thermal conductivity and low mass transfer resistance to reduce heat loss across the membrane. The membrane should also be highly resistant to chemicals, such as acids and bases, and exhibit strong thermal stability in a wide range of temperatures. Consequently, the following characteristics of membranes should be present for membrane distillation [18]:

a. High hydrophobicity,is the ability of metal to repel water form its surface

b. Low thermal conductivity. High thermal conductivities increase sensible heat transfer and reduce vapor flux due to reduced interface temperature difference.

c. High porosity membranes have weak mechanical properties and often break or collapse when subjected to little pressure, degrading membrane function.

*1.5.2.1 Advantages of membrane**:***

a. Ions, macromolecules, colloids, and other non-volatiles are all (theoretically) rejected 100%.
b. Decreased operating temperatures compared to traditional distillation.
c. Low sensitivity to process changes, such as pH and salt levels.
d. Favorable to exceptional mechanical and chemical resistance characteristics.
e. Possibly less expensive capital expenditures than RO (Reverse Osmosis)

1.5.2.2 Disadvantages of membrane:

a. The expansive energy intensity (although a low-grade heat might be used).
b. Low yield in continuous mode
c. Surfactant sensitivity

1.5.2.3 Membrane materials

The most frequently utilized materials for MD membranes are poly-tetrafluoroethylene (PTFE), poly (propylene) (pp), and polyvinylidene-fluoride (PVDF)[19]. The membranes porosity ranges from 0.60 to 0.95, their pore size is between 0.2 and 6.0 µm, and their thickness is between 0.04 and 0.25 mm [20] and [21]. Table (1-1) provides information on these materials' surface energies and thermal conductivities. PTFE has the most hydrophobicity (most considerable contact angle with water) of these materials and the best chemical and thermal stability and oxidation resistance. However, it also has the highest conductivity, increasing heat transfer via PTFE membranes. PVDF is readily formed into membranes with various pore configurations using various preparation techniques and has strong hydrophobicity, heat resistance, and mechanical strength. Additionally, PP has strong chemical and heat resistance[22].

Table (1. 1): Surface energy and thermal conductivity are the most common materials used in MD[18].

Membrane Material	Surface Energy ($\times 10^{-3}$ N/m)	Thermal Conductivity (W /m. K)
PTFE	9–20	~0.25
PP	30.0	~0.17
PVDF	30.3	~0.19

1.6 Motivation

In the past and present, a passive method is used to cool the PV cell, where the heat generated in the cell is rejected to the outside using several fluids such as water or air. The current work deals with the issue actively as the heat stored in the cells is withdrawn for two purposes, the first is to cool the solar panel, and the second is to desalinate brackish water.

1.7 OBJECTIVES of THIS STUDY:

1. Performing numerical analysis for the PV-membrane distiller(PMD) performance using COMSOL – Software.
2. Built a pilot model of the (PMD) using a small panel of dimension 14 ×16.5 cm and 2 W power.
3. Use two types of membrane material (PTFE and PVDF)
4. Study of several membrane porosities to select the best pore size.
5. After choosing the best membrane porosity, the performance of a field PMD of dimensions of 67 × 54 cm and 50 W is studied.

Chapter Two

Literature Review

Chapter Two

Literature Review

2.1 INTRODUCTION

The chapter introduces a literature review of the theoretical and experimental studies relating to membrane distillation and cooling PV Panels. The idea of producing freshwater and electricity simultaneously to maximize the use of solar energy has lately received much attention due to its proven potential in various situations.

2.2 EXPERIMENT WORKS

At Fraunhofer Institute for Solar Energy Systems Germany (51°N, 09°E), Koschikowski *et al.*, 2009 [23] introduced a six-compact solar distillation system of 100 to 500 l/day and another extensive capacity system of 10 000 *l*/day. The thermal energy is supplied by a thermal solar collector, while the power needed to operate the pumps and valves is powered by PV solar system. Membrane technology is used in the distillation process. The temperature difference across a hydrophobic, microporous membrane is the driving force of the vapor. The productivity of the fresh water in January 2005 was 150 l/day for the six compact systems.

In China (35°N, 105°E), Wang *et al.*, 2015 [24] studied a prototype desalination system that combines a vacuum tube solar heat collection (SHC) unit with a vacuum membrane distillation (VMD). Before employing solar heat to study the whole system, the parametric sensitivity of the VMD unit performance was analyzed using an electric heater as the heat source. The membrane properties are: pore size of 0.2µm, porosity between 0.5-0.6, and thickness are 0.210mm. The best conditions for high trans-membrane flow were hot feed temperatures at more than

65 $^{\circ}$C and cold side absolute pressures of less than 0.02 MPa. The VMD unit demonstrated excellent compatibility with erratic solar energy and the intermittent off-and-on operating mode by running intermittently for 305 hours over five months, alone or in conjunction with the solar heat system. The transmembrane flux was approximately 4 kg/m^2 h, and the specific heat consumption was close to 750 kWh/m^3

In India (22°N, 77°E), Selvi and Baskaran, 2015 [25] developed a small-scale solar PV distillation system driven by MD. The system is built from a membrane of pore size o.2 µm and an area of 5.6 m^2, a solar PV array, and a steam evaporator. The principal work of the system is that the pressure differential transfers the evaporation at the feed-membrane surface across the membrane to the permeate side, where it condenses within the membrane module. Based on the mass transfer of vapor transferred due to the difference in vapor pressure, the hydrophobic membrane is used as a barrier to remove pollutants. The exact process for traditional MD without solar PV panels is employed by delivering a 230 V AC current. They found that for the solar PV-driven MD, the permeate flow was 0.502 l/m^2 h, the specific thermal heat consumption was 1030 kJ/h, and the power consumption was 0.285 kW. The product distillate was 63 l/day

In China (35°N, 105°E), Yang *et al.*, 2017 [26] studied the ability of generated power from the evaporation of interfacial water using solar energy. A prototype hybrid solar system built from two pieces of Ag/AgCl electrode plate of dimensions 10 ×10 cm, one piece of Nafion membrane layer of measurements 10 × 10 cm, and a piece of carbon nanotube (CNT)modified filter paper of sizes 10 × 10 cm with two tails structure 1 × 2 cm.Applying an ion-selective membrane. They found that the maximum thermal efficiency of the hybrid system was 75%, and it can produce 1 W/ m^2 of interfacial water under one sun illumination.

In China (35°N, 105°E), Li *et al.*, 2018 [27], Demonstrated that storing and reusing the heat obtained through the steam generation process can generate clean water and power simultaneously. Using the heat of evaporation of the water during condensation can generate pure water at the chamber's output. In contrast, the steam's energy is retained in the chamber to maintain its high temperature. They improved the work by using thermoelectric modules to generate extra generate power. The findings showed that the efficiency of solar-to-steam energy transfer reached 72% when additional electrical power was used.

In Italy (12°E,42°N), Chiavazzo *et al.*, 2018[28] developed a ten-stage passive, high-yield distill seawater using the vapor pressure differential across a tiny gap between two hydrophilic thin layers. The device consists of aluminum plates and hydrophilic microfibre of an area of 12×12 cm^2, and the thickness is 1mm. As a result, this process is effectively run at a maximum temperature of 65 °C and a thermal power density of less than 1 kW/ m^2. Under laboratory settings, the device that performs the best may produce a specific mass flux of the entire distillate up to almost 3 l/m^2 .h. Theoretically, theoretical modeling suggests a potential of up to 6 l m^{-2} h^{-1}.

In Canada (60°N, 95° W) Manuscript, 2018 [29] demonstrated a salt-rejecting evaporation structure that can produce vapor continually while floating in a salty body of water, such as an ocean. The salt-rejection evaporation structure was made to float atop salty bodies of water, collect and convert incoming solar energy into thermal energy, transport this heat to the water for vapor formation, and reject excess salts to the water below. The system consisted of several layers in the evaporation structure. The top layer is a hydrophilic black cellulose fabric that absorbs solar radiation and water. Water evaporation is accelerated by heating a small amount of water, which causes excess salt ions to rise. The results showed that the daily production of drinking was 2.5 *l* / m^2 per day.

In Saudi Arabia (24°N,45°E), Aleid, 2019 [30] studied three multistage MDs; each stage consisted of four layers, namely a stainless steal plate as a thermally conductive layer, a hydrophilic porous layer worked as an evaporation layer, a hydrophobic layer membrane, and a hydrophilic porous layer for condensation of steam. The area and thickness of each layer were 5×5 cm^2 and 0.1mm, respectively. The membrane porosity is 0.84, and the pore size of 0.45 μm.To improve the system's thermal efficiency, the recycled latent heat generated by the solar cell can be reused. The results showed high performance of a water production rate of 2.66 kg/m^2 h and a relatively low temperature of the solar cells, 47 to 48°C.

In Saudi Arabia (24°N,45°E), Wang *et al.*, 2019[31], Built a photovoltaic-membrane distillation (PV-MD) device that can produce clean water and power simultaneously from solar energy with excellent energy efficiency. A solar cell receives solar energy and transforms it into power and heat; the heat generated within the PV panel can be used to produce fresh water by multistage membrane distillation. The single-stage unit consisted of aluminum nitride as a heat conduction layer, a porous hydrophobic membrane as an evaporating layer, and a condensation layer. During the seawater desalination, the thermally conductive, hydrophobic layer membrane and hydrophilic layer dimensions for the condenser and evaporator were 4.0 ×4.0 cm. The results demonstrate that under one solar irradiation, it can reliably produce clean water of more than 1.64 kg/m^2.h from seawater and improve the solar PV system efficiency by more than 11% and solar cell temperature of less than 58°C.

In China (35°N, 105°E), Li and Lu, 2020 [32] developed a novel solar-powered stand-alone sweeping gas membrane desalination system. A solar thermal collector was installed for thermal energy collection, and a PV solar array was installed for generated AC power. The unit was modeled mathematical, and test results were conducted in actual meteorological circumstances to verify the model. The system's main parts are the solar thermal collector, PV array, hollow-fiber membrane module, and dehumidification unit. The results showed that the production of freshwater is between 9.98 and 23.26 kg/day

In Saudi Arabia (24°N,45°E), Wang, 2020 [5] tested a multistage membrane distillation device (MSMD) installed at the back of the solar pane. In each stage, the latent heat of steam condensation can be recycled. The hydrophobic membrane is 0.1 mm thick and has 0.86 porosity. Each stage consisted of a heat-conductive layer, a hydrophilic layer, and a membrane. Under one-sun radiation, the first-generation photovoltaic-membrane distillation (PV-MD) technology produces clean water at a rate of 1.64 kg/m^2 h when the PV cell temperature of 58 ^oC. They also tested a 5-stage PV-MD-EC system and showed that the productivity of such a system was around 2.45 kg/ m^2. h, with a lower solar cell temperature of 48^oC. The 5-stage system is the second generation of the PV- membrane distillation-evaporative crystallizer PV-MD-EC due to its lower cell and 8% more efficiency than PV-MD.

In China (35°N, 105°E), Deng *et al.*, 2020 [33] used the polyvinylidene fluoride hollow fiber membrane for a solar thermal-photovoltaic vacuum membrane distillation system (VMD). The VMD was modeled and optimized using the response surface approach. The membrane of a pore size of o.2 µm, a porosity of 0.6, and an area of 0.1 m^2. The system consisted of a PV panel, evacuated tube collector, vacuum fiber membrane distillation, circulation pump, two water tanks, electric heating wire, and collection bottle of condensate water. The experimental studies reveal that the actually penetrate flux, which was 6.26 *l*/m^2 h as opposed to the projected value of 6.05 *l*/m^2 h, is somewhat higher.

In Saudi Arabia (24°N,45°E), Wang et al., 2021 [34] designed a PV-membrane distillation-evaporative crystallizer (PME) system. The PME used the heat generated by the PV panel to produce fresh water, as well helping to cool the PV cells. A hydrophobic membrane with a thickness of 0.1 mm and porosity of 0.86 was selected for the fabrication of a five-stage PME device; the dimension of the stainless steel plate was 50×50 mm, the hydrophilic membrane was 55×55 mm, and the non-woven fabrics 40 × 150 mm. The results showed that the PME device could reduce the temperature of the solar cell to 46 ~47°C, compared to 61.2 ºC of the same solar cell working alone. The same PME produced freshwater from seawater at a rate of 2.35 to 2.45 kg/m^2. h.

In Saudi Arabia (24°N,45°E), Chen *et al.*, 2021 [35] proposed a decentralized water/electricity cogeneration system that combines concentrated PV/thermal (CPV/T) collectors with a vacuum multi-effect membrane distillation system. The system consisted of a series of CPV/T collectors, a hot water tank, a vacuum multi-effect membrane distillation (V-MEMD) module, a feed tank, and a distillate tank. The results showed that it could convert 70% of the solar irradiance into helpful energy. The annual productivity of electricity and distilled water are 562 kWh, and 5.25 m^3 of fresh water per m^2 of the solar collector area.

In China (35°N, 105°E), Liang *et al.*, 2021 [36] developed a combined thermal membrane distillation and solar concentrating system. As a result, the saltwater immediately absorbs the heat produced by the solar cells and concurrently evaporates to create water vapor. The water vapor went to the chamber to condense. It was found that, under 900 W/m^2 of radiation, the total efficiency evaluated under steady-state conditions is 0.42, which is about 5% less than the predicted result. The hourly water yield may reach 60.5 g with a water yield efficiency of 32.6%, and the hourly average output power can be 9.93 W with an electrical efficiency of 8.02%, according to experiments conducted in real-world weather conditions. The system's total effectiveness may reach 40.62%.

In France (46°N,2°E), Diaby *et al.*, 2021 [37] developed a heat pump for cooling and desalination of water using membrane distillation. The findings of this investigation clearly show the possibility of using an Air Gap Membrane Distillation (AGMD) unit connected to a heat pump since Membrane Distillation can function at low temperatures. The device consists of two parts a heat pump and AGMD. The heat pump consists of the compressor, condenser (tube in tube), expansion, and evaporator. The membrane has a 0.25 µm thickness, 55% porosity, and a 0.064 µm pore size. The linked prototype was tested using the equipment utilized for the earlier testing. Results showed that the estimated COP is 1.2. The water in the tank is at room temperature of 19 ± 1 ˚C for all tests performed. The feed flow rate of 2 *l*/h has been observed.

2.3 NUMERICAL WORKS

In Saudi Arabia (24°N,45°E), Baloch 2015 [38] investigated the cooling of the cell surface numerically. The simulation modeling by ANSYS-Fluent software 6.3. Thermal measurements for an uncooled PV showed a cell temperature as high as 71ºC while the cooled solar cell temperature was 45°C. The maximum percentage improvement in power output was 0.35, whereas the maximum percentage increase in the conversion efficiency was 0.36 compared to the performance of an uncooled PV system.

In Romania (46 ºN,25 ºE), Popovici et al. 2016 [39] This study used air-cooled heat sinks to reduce the photovoltaic panel's temperature. Numerically The heat sink was conceived as a ribbed wall, realized of a high thermal conductivity material. The numerical model was realized using ANSYS-Fluent software for turbulent flow. The operating temperature of the PV panel reaches about 56 °C if there is no heat sink. According to simulations, if using a heat sink, the temperature is reduced by at least 10 °C . The increase in the maximum power produced was from 6 to 7%.

In Egypt (30°N,31°E), Monjezi *et al.*, 2020 [40] modeled a 5 m^3/day of the Revers Osmose (RO) desalination unit using ROSA 9.1 software for distillation of fresh water from seawater. The required solar panel area with and without the cooling system is evaluated and compared for the same climatic conditions. The modeling results indicate that the proposed simulation leads to reduced about 0.12 kWh/m^3 in the power consumption rate of RO desalination, as well as improves the power generation of the PVT cells, thus decreasing the PV panels area by 6%

In China (35°N, 105°E), Zhao *et al.*, 2020 [41] studied a unique hybrid system with a photovoltaic module (PVM) and a direct contact membrane distillation (DCMD), in which the heat produced by the use of the DCMD's comparatively long wavelength sunlight is provided by the PVM. The PVM and DCMD models are mathematically defined and verified, and the hybrid system's performance is assessed by considering the advantages of including DCMD. The maximum energy efficiency (MEE) and maximum power density (MPD) of the hybrid system were predicted to be, respectively, 60.73% and 607.29 W/m^2, which are significantly higher than those of the single PVM, which are, respectively, 11.15% and 111.48 W m^2. These results are based on numerical calculations. It is established that the suggested hybrid system is a practical design for improving energy conversion efficiency. Extensive parametric studies are conducted to investigate how critical operational parameters, including feed water temperature, permeate water temperature, and feed water and permeate water flow velocities, impact the hybrid system's performance. Additionally, the individual performances of the hybrid system and DCMD are investigated at the maximum power condition.

In Egyptian (30°N,31°E) Rabie et al., 2022 [42] introduced the hybridization of high-concentrating photovoltaic (HCPV) with membrane distillation (MD). The study aims to keep the cell's temperature within the recommended temperature. The problem is that MD needs high thermal energy for heating the water. So, a microchannel was used within the PV panel cells to withdraw the heat absorbed by the cells. The proposed system was solved numerically using ANSYS 2020 software. The theoretical results showed that a coolant water flow rate of 370 ml/min could maintain the maximum cell temperature within the safe range. The results were supported by an experimental study and showed that the freshwater production was 46 kg/m^2.day

2.4 EXPERIMENT AND NUMERICAL WORKS

In UAE (25°N,55°E), Kumar, 2015 [43] introduced a solar distillation system to supply potable water to urban settlements by combining solar-powered hot water installations with water purification systems that use membrane distillation. The device consists of a single cassette mounted between two condensing aluminum plates and cooling ducts. The dimension of the two membranes, each of 0.1 m^2 surface area, pore size: 0.2 µm, and thickness:280 µm, are thermally welded onto a polypropylene cassette frame to fit into the module. Experimental investigations were conducted on this integrated system for the co-production of pure water around 15-25 l/day, along with hot water production equivalent to the needs of a family of five. A dynamic simulation model was developed in TRNSYS to analyze the optimum operating conditions of the system.

In China (35°N, 105°E), Xu *et al.*, 2020 [44] investigated a small-scale PV direct drive electrodialysis (Electrodialysis is a process with a long history of over half a century, which yields mature applications in the desalination of brackish water.) device for water desalination. MATLAB is used to solve the electrodialysis desalination model. The effects of voltage drop, flow rate, ion membrane area, and electrodialysis compartment size were studied using a mathematical model. The results showed that, on a sunny day, the PV panel could produce 30V, and the water salinity at the exit reaches 1000 ppm in 50 min and 20min sooner than on overcast and gloomy days. At 200 ml/h, 500 ml/h, 800 ml/h, and 1100 ml/h, the cumulative freshwater was 0.4 *l*, 1 *l*, 1.6 *l*, and 2.2 *l* after 120 minutes.

2.5 SCOPE OF THE CURRENT STUDY

The practical and theoretical investigations examined in this chapter looked into solar panels' membrane distillation and cooling—methods for desalinating salt water under various operational circumstances. The last researches used a small-scale solar panel, didn't use simulation software for cooling solar panels by membrane desalination, and did not use different types of membrane material and pore sizes. The scope of the current study can be summarized as follows:

1. Integrate cooling solar panels and water production
2. Build a theoretical model using the Comsol multiphysics software for the performance of the photovoltaic-membrane distillation (PMD) system.
3. Design and build the photovoltaic-membrane distillation (PMD) system depending on the thickness of membrane and pore size of the membrane
4. Study the performance of the PVM unit under Iraqi climate conditions.

Table (2.1): Summary of the Literature Review

Author/ Date	**Country (long., Lat.)**	**The porosity of the membrane and the number of stages**	**Result**
S. Aleid (2019)	Saudi Arabia **Long.** 45°E **Lat.** 24°N	3-stage, the porosity of 0.84 and the pore size of 0.45µm.	Water production rate of 3.67 kg/m^2 per hour and a relatively low temperature of the solar cells, 44°C~45°C.
W. Wang et al. (2019)	Saudi Arabia **Long.** 45°E **Lat.** 24°N	3-stage, the porosity of 0.85 and the pore size of 0.45µm.	Producing clean water (>1.64 kg $m^{-2}h^{-1}$) solar cell temperature of~58◦C temperature of solar cells.
Chiavazzo et al. (2018)	Italy (**Long.** 12°E **Lat.** 42°N)	Ten-stage 0.62 porosity, the pore size of either 0.1 µm or 3.0 µm.	It may produce a specific mass flux of the entire distillate up to almost 3 l m^2 h^{-1}.
W. Wang et al. (2021)	Saudi Arabia **Long.** 45°E **Lat.** 24°N	Five-stage the porosity of 0.86.	The solar cell to 46°C~47°C, compared to ~61.2◦C of the same solar cell working alone. Produced freshwater from 2.35~2.45 kg m^{-2} h^{-1}.
U. Kumar (2015)	In UAE **Long.** 55°E **Lat** 25°N	The dimension of the two membranes is 0.1 m^2 surface area, Pore size: 0.2 µm, and Thickness:280 µm.	Production of pure water (around 15-25 l/day) along with hot water production is equivalent to the needs of a family of five.

H. Deng *et* al. (2020)	In China **Long.**105°E **Lat** 35°°N	The characteristic of the membrane is a pore size o.2µm, a porosity of 0.6, and an area of 0.1 m^2.	Experimental studies reveal that the actual permeate flux, which is 6.26 L/m^2 h as opposed to the projected value of 6.05 L/m^2 h, is somewhat higher.
J.Koschiko (2009)	**In** Germany **Long.** 09°E **Lat** 51°N	The device's dimensions are 0.2 µm pore size, 450–800 mm height, 300–400 mm membrane diameter, and 7 m^2 solar thermal collector area.	The distillate production rate of the compact system is increased by the redesign of MD modules, as demonstrated in Freiburg, by up to 150 L/day.
P. Yang et al. (2017)	In China **Long.**105 **Lat** 35°	The prototype includes two pieces of Ag/AgCl electrode (10 cm ×10 cm), one piece of Nafion membrane (10cm ×10 cm), and a piece of CNT-modified filter paper (10 cm ×10 cm) with two tails structure(1cm ×2cm).	The results show achieving solar thermal efficiency of up to 75% and deriving electricity power of ~ 1 W m^{-2} under one sun.
Q. Chen et al., (2021)	Saudi Arabia **Long.** 45°E **Lat.** 24°N	The pore size of ~0.2 µm and a thickness of 0.12 mm.	The results can convert ~70% of the solar irradiance into helpful energy. The annual productivity of electricity and distilled water are 562 kWh and 5.25 m^3 per m^2 of the solar collector area.

S. Liang, H. (2021)	In China **Long.** 105°E **Lat.** 35°°N	The dimensions are 500 mm long, 321.87 mm wide, and 400 mm high.	The total efficiency is 0.42. The hourly water yield may reach 60.5 g with a water yield efficiency of 32.6%, and the hourly average output power can be 9.93 W with an electrical efficiency of 8.02%.
A. T.Diaby, (2021)	France **Long.** 46°N **Lat.** 2°E	The membrane characteristics have a 0.25 µm thickness, a 0.55 porosity, and a 0.064 µm pore size.	Results, as shown, The estimated COP is equal to 1.2. The feed flow rate of 2 *l*/h.
A. Manuscript, (2018)	Canada Long. 95° W Lat. 60°N	The top layer is a hydrophilic black cellulose fabric, and Underneath the black cloth is an insulating structure that helps to reject extra salts.	The result, as shown, creates enough freshwater to meet each person's daily requirements for drinking at a rate of 2.5 *l* m^{-2} day^{-1}.
W. Wang, (2020)	Saudi Arabia Lat.24°N, Long.45°E	The characteristics of the hydrophobic membrane with a thickness of 0.1 mm and porosity of 0.86 are examined. Each stage consists of a heat-conductive layer, a hydrophilic layer, and a membrane.	The first test produces clean water at a rate of 1.64 kg/m^2 h at a solar cell temperature of 58 ^oC—the second test is a 5-stage product of 2.45 kg m^{-2} h^{-1} with a lower solar cell temperature of 48^{o}C. Third, an eight-stage produced 3.61 kg/m^2 of clean water per hour for saltwater desalination.

Y. Wang, (2015)	In China **Lon.** 105 **Lat.** 35°	The membrane properties are: pore size of 0.2µm, porosity between 0.5-0.6, and thickness are 0.210mm.	In the studies of the SHC-VMD combination system, the transmembrane flux was approximately 4 kg/(m^2 h), and the specific heat consumption was close to 750 kWh/m^3.
S. R. Selvi (2015)	in India **lat.**22**long**. 77°	The properties of the membrane: pore size o.2 µm and area 5.6 m^2.	The product distillate was obtained at 63 *l*/day.
H. Xu, X. (2020)	In China **Long.**105 **Lat.** 35°	MATLAB is used to solve the electro-dialysis desalination model.	At 30V, the lowest and maximum salinities are 17.03 and 36.032 mol.m-3. 20V lowest salinity is 19.14 mol.m^3; the maximum is 38.424mol.m^3. 10V lowest salinity is 22.478 mol.m-^{3}; maximum is 39.572 mol.m-^{3}. freshwater was 0.4 *l*,1 *l*, 1.6 *l*, and 2.2 *l* after 120 minutes.

Author/ Date/	**Country(long., Lat.)**	**Software that uses**	**Result**
Monjezi *et al.*, (2020)	In Egypt **Long.** 31°E **Lat.** 30 °N	Simulated using ROSA 9.1 software	It was demonstrated that a reduction of 0.12 $kWh.m^{-1}$ in the specific energy consumption of the RO unit could be achieved using the proposed photovoltaic thermal cooling leading to a 6% reduction in the required solar panel surface area.
M. Rabie, M. F. (2022)	In Egypt **Long.** 31°E **Lat.** 30 °N	Ansys 2020 program	It was discovered that a coolant flow rate of at least 370 ml/min and a coolant outlet temperature of 68 ^{o}C were required to maintain a safe maximum cell temperature.
Q. Zhao, H. (2020)	In China **Long.** 105°E **Lat.** 35°°N	Numerical calculations	The maximum energy efficiency (MEE) and maximum power density (MPD) of the hybrid system are predicted to be, respectively, 60.73% and 607.29 W m^2, which are significantly higher than those of the single PVM, which are, respectively, 11.15% and 111.48 W m^2

Chapter Three

Modeling And Theoretical Analysis

Chapter Three

Modeling And Theoretical Analysis

3.1 INTRODUCTION:

The mathematical modeling and theoretical analysis of the photovoltaic-membrane distillation (PMD) system are discussed in this chapter. In addition, the thermal performance of the solar photovoltaic module with and without membrane has been investigated. The simulation model was solved numerically using COMSOL Multiphysics 5.6 software to predict the thermal characteristics of the solar photovoltaic module with a membrane distillation system.

3.2 MODELING OF THE PHOTOVOLTAIC MODULE-MEMBRANE

The PMD system commonly consists of single or multistage, where each stage includes several layers of hydrophilic membranes to work as an evaporator or condenser. The working principle of any stage for the PMD system is to minimize the distance between the thin hydrophilic layers; thus, the cycle of the evaporation and condensation processes is carried out at ambient pressure. Figure (3-1) shows a single-stage PMD, where the hydrophilic (evaporation layer) adheres directly to the aluminum plate, which is in direct contact with the back of the solar panel. The water is supplied to the PMD unit by pumping or gravity force; thus, the evaporator layer is wetted thoroughly due to the capillary force. The first aluminum plate transfers generated heat in the PV panel to the salty water. In contrast, the last aluminum layer comes into contact with the heat sink to dissipate the generated heat in the PV panel as latent heat of evaporation. As the salty water comes into contact with the first hot aluminum layer, part of the salty water evaporates and transfers through the steel mesh layer, then through the membrane, and finally reaches the condensing layer. In the condenser layer, the vapor begins to condensate to fresh water and lose the latent heat of evaporation to the aluminum plate for the multistage system or to the heat sink for the single-stage system. In any case, the heat sink is placed at the last cooling stage.

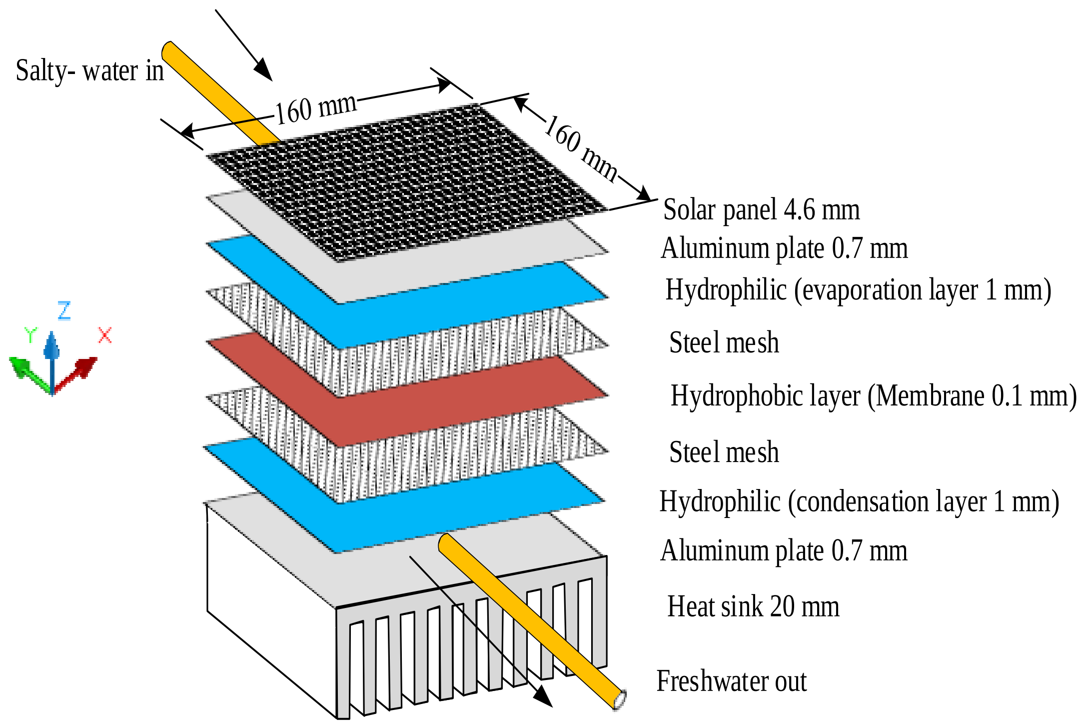

Figure (3-1): Schematic diagram of PMD system.

3.3 ENERGY BALANCE OF THE SOLAR PV PANEL AND MEMBRANE

In the photovoltaic-membrane distillation system, the latent heat released during the vapor condensation process in each PMD stage is reused as the energy source for the next PMD stage. Therefore, the heat generated by the PV-thermal component is thus reused for multiple evaporation–condensation cycles. When it is exposed to sunlight with an irradiance intensity of G, most of the solar energy is captured by the solar cell (Q_{abs}) depending on the solar absorptance (α) and transmissivity (τ) of the glass layer, and the rest is lost as the reflected solar radiation.

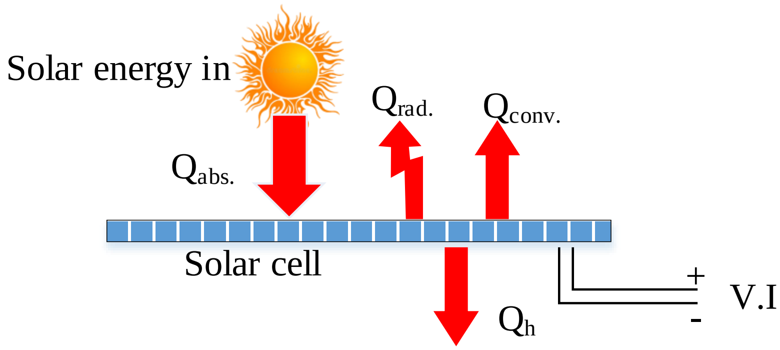

Figure (3.2): Solar thermal energy conversion system.

For the control volume of the solar PV cell depicted in Figure (3.2), the energy balance can be expressed by[45]:

$$\frac{dE}{dt} = \sum m_{in} * h_{in} - \sum m_{out} * h_{out} + \sum Q - W \qquad (3.1)$$

Taking a control mass to the solar cell and disregarding any heat transfer by radiation, equation 3.1 becomes:

$$0 = Q_{abs} + Q_{conv} + Q_h + Q_{red.} - W$$

$$Q_{abs} = G.A.\alpha\ .\tau \qquad (3.2)$$

G= solar radiation (W/m^2)

A= area of the solar cell (m^2)

Solar absorptance (α), which is defined as a weighted percentage between absorbed radiation energy and incoming solar radiation energy, is computed to determine the solar energy capture capacity of the solar cell using the following formula [46]:

$$\alpha = \int_{300}^{2500} \frac{\beta(\lambda) * \varphi(\lambda) d\lambda}{\beta(\lambda)\ d\lambda} \qquad (3.3)$$

The numerical value for the solar absorptance (α) and transmissivity (τ) of the glass layer is 0.87 and 0.90 [5].

Where:

α = solar absorptance

β = intensity of the light

$\varphi(\lambda)$ = wavelength of the light

$$Q_{conv} = h_c . A . (T_{cell} - T_{amb}) \quad (3.4)$$

Q_{conv}: convection heat transfer from the cell surface to the ambient (W)

h_c: heat transfer coefficient by natural convection ($W/m^2.K$).

The convection heat transfer coefficient can be written as [47]

$$h_c = 5.8 + 3.804 \, . V^{\circ} \quad (3.4a)$$

Where : V^{o}= wind speed (m/s)

T_{cell}= Solar cell temperature (K) , T_{amb} = Temperature of ambient (K)

Q_h = heat converted into a heat flux and delivered to the thermal system (W).

$$Q_{rad} = \varepsilon . A . \sigma . \left(T_{cell}^4 - T_{amb}^4\right) \quad (3.4b)$$

Q_{rad} = radiation heat transfer from the cell surface to the ambient

ε = emissivity of the material**.** The numerical value of the emissivity (ε) is 0.94 [31]

σ= stefan boltzmann constant value has value is $5.669 \times 10^{-8} \ \frac{W}{m^2K^4}$ [48]

W: power produced by the solar cell (W)

$$W = V . I \quad (3.5)$$

V: voltage drop across the solar cell (V)

I: output current (A)

3.3.1 Transfer mechanisms of membrane distillation (MD)

The membrane water distillation process involves simultaneous mass and heat transfer. Theoretical approaches to describe and model these transfer mechanisms have been essential to understanding and analyzing MD systems' behavior and performance [49]. This section discusses the commonly used transfer methods in Direct Contact Membrane Distillation (DCMD), assuming that typical MD operations occur without wetting, scaling, or fouling that restricts or disrupts the process and a complete salt rejection without liquid or salt entering membrane pores. As a result, it is assumed that water evaporation occurs at the feed side membrane surface, and the liquid/vapor contact is located at the pore entrance.

3.3.1.1 Heat transfer

Two phases involve heat transfer from the feed to the permeate side [50]. First, the heat transfers across the membrane from the hot to the cold side are sensible and latent heat to form the temperature difference between the boundary layer and bulk flow. Due to the temperature differential created by the first stage, heat convection is used to transport heat from the bulk flow of the feed to the boundary layer. In the first step, as shown in Figure (3.3), the sensible heat is conducted through the membrane to the cold side. The latent heat is carried by the water vapor, evaporating at the interface between the hot stream and membrane pores and condensing at the interface between the pores and cold stream for DCMD [51]. The thermal resistance of the heat transfer process in the DCMD is illustrated in Figure (3.5). Equation (3.6) represents the total heat flow across the membrane and includes the thermal energy for water evaporation and the term for thermal conduction [52].

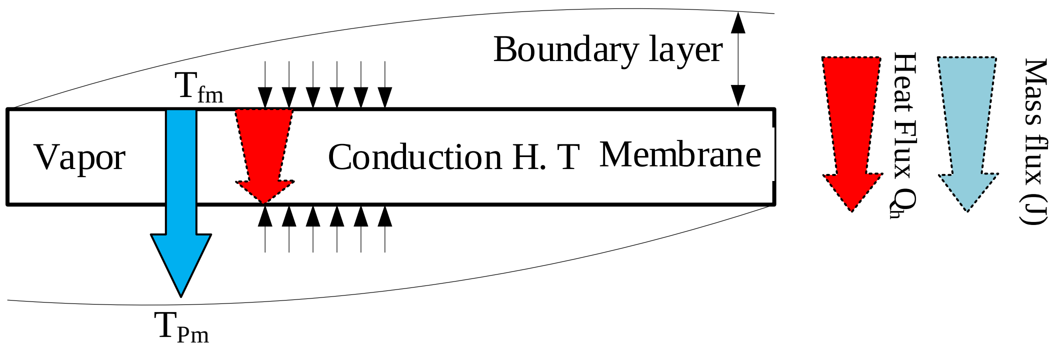

Figure (3.3): Heat and mass transfer through the membrane [53].

From the energy balance shown in Figure (3.4), the total heat flow across the membrane, including both the thermal energy for water evaporation and the term for thermal conduction, is expressed by Equation (3.6) [45]:

$$0 = \dot{m}_{in}.h_{in} + Q_h + Q_{Latent} + Q_t - \dot{m}_{out}.h_{out} \quad (3.6)$$

Where :

$\dot{m}_{in}$= mass flow rate at the inlet flow (kg/s)

h_{in}= enthalpy of inlet flow (kJ/kg)

$\dot{m}_{out}$= mass flow rate at outlet flow (kg/s)

h_{out}= enthalpy at outlet flow (kJ/kg)

Q_t= heat transfer by conduction (Watt)

$$Q_t = k.A.\frac{T_{fm} - T_{pm}}{\delta} \quad (3.7)$$

T_{fm} = feed bulk temperature (K)

T_{pm} = permeate temperature (K)

k = thermal conductivity of total air and membrane (W/m.K)

δ = thickness of the membrane (m)

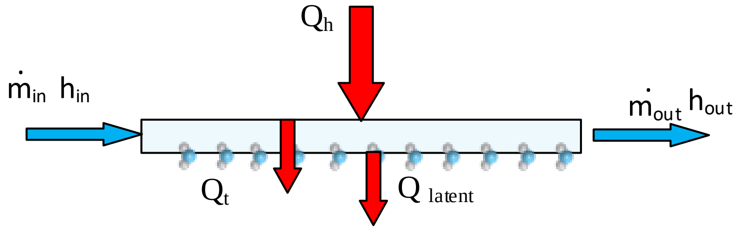

Figure (3.4): Energy balance of the evaporation layer (membrane)

The temperature polarization (T_{TP}) is generally used to measure the magnitude of the B.C layer resistance in relation to the heat transfer and calculated for the condensation and evaporation layer by Equation [5]:

$$T_{TP}=\left(\delta * \frac{W-Q_{abs}-Q_{rad}-Q_{conv}}{K}\right) \qquad (3.8)$$

3.3.1.2 Estimating the Thermal Conductivity

The thermal conductivity of the membrane is based on the thermal conductivity of both materials that the membrane made PTFE (polytetrafluoroethylene) and PVDF (polyvinylidene fluoride) k_m and air k_A. The following Equation is used to determine the thermal conductivity of the membrane [54]:

$$k = \frac{1}{\frac{\epsilon}{k_A}+\left(\frac{1-\epsilon}{k_m}\right)} \qquad (3.9)$$

Where: k_A: thermal conductivity of air (W/m.k)

k_m: thermal conductivity of the membrane material (W/m.k)

ϵ = porosity of the membrane

The thermal conductivity of PTFE and PVDFcan be estimated by[55]:

$$k_m = 0.253 + 4.86 \times 10^{-4}T \qquad (3.10)$$

3.3.1.3 Membrane Porosity

The gravimetric approach was used to determine the membrane porosity. If the dry weight of the membrane is (W_1), and the weight of the wet membrane after being immersed in ethanol for five minutes is (W_2). The membrane porosity is calculated as follows [56]:

$$\epsilon = \frac{(w_2 - w_1) * \rho_m}{\rho_m * (w_2 - w1) + w_2 * \rho_e} \qquad (3.11)$$

w_1: membrane's dry weight (kg).

w_2: membrane's wet weight (kg).

ρ_m: density of membrane (kg/m^3)

ρ_e: density of ethanol (kg/m^3)

The density of the membrane is 2200 kg/m^3[30], and for ethanol is 789 kg/m^3 [57]

3.3.1.4 Mass Transfer

The mass transfer resistances in the MD process may be compared to electrical resistances, as illustrated in Figure (3.5), similar to that for the heat transfer resistances. [58] The concentration boundary layer transitions from a salt value of concentration C_f to C_{fm} at the membrane surface and may also be used to describe the mass transfer on the feed side. If MD functions correctly without salt leaking into the permeate, there is no need to consider a concentration profile on the permeate side. In the DCMD process, the mass transfer occurs in three stages; first, the hot feed water vaporizes at the liquid/gas interface. Then, driven by the vapor pressure difference, the vapor travels through the pores from the hot interface to the cold interface, and finally, the vapor condenses onto the cold side [21]. As a result, two main variables affect mass transfer; membrane permeability and the differential in vapor pressure. Mass transfer over the membrane may be the limiting step for mass transfer in MD if the fluid dynamics parameters on both sides of the membrane are favorable [59].

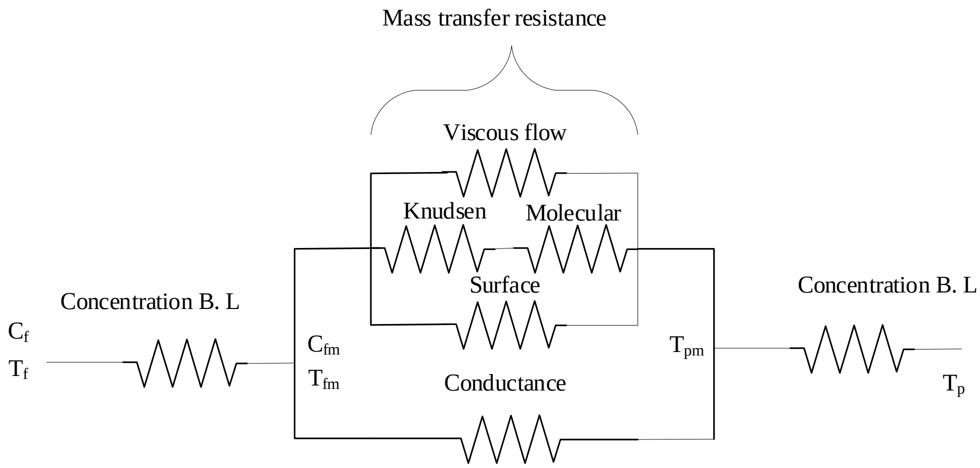

Figure (3.5): Heat and mass transfer resistances in the MD process[60].

Physical characteristics may affect membrane permeability in the following ways:

(1) Because the membrane is not entirely porous, the effective area for mass transfer is smaller than the total membrane area.

(2) The route for vapor transport is longer than the thickness of the membrane for most practical membranes, and the membrane holes do not pass directly through the membrane.

(3) By reducing the vapor molecules' momentum, the inside walls of the pores raise the diffusion barrier.

These three process models explain the relationship between mass transfer and collisions (molecule-molecule collisions or molecule-pore wall collisions).

Therefore, the distinction between these three models hinges on the relationship between the membrane's pore size (r) and the vapor's mean free path (l). Molecule-pore wall collisions predominate in the Knudsen (kn) zone (r <0.5 l) when the membrane's pore size is tiny. Molecule-molecule collisions predominate for continuous diffusion (r > 50 l) since the membrane's pore size is sufficient. This diffusion is referred to as transition diffusion if 0.5 l < r <50 l, at which point both continuum diffusion and Knudsen diffusion must be considered. The mean free path of the vapor for water desalination is calculated to be 137.7 nm at 40°C and 1 atm [61]. A membrane with smaller pores has a lower membrane coefficient because the molecule-pore wall diffusion may impede the flow of the vapor molecule. The membrane utilized often has larger pores than the Knudsen area. Liquid water may directly flow through the membrane when its pores are pretty big (r > 6 µm in the continuum area, for example).

$$kn = \frac{l}{r} \qquad (3.12)$$

l= is the mean free path of the water vapor molecule (µm)

The following Equation may be used to compute the membrane coefficient (c_m) since, in light of these factors, transition diffusion is more appropriate in this situation [61]:

$$c_m = \frac{1}{\frac{3}{2}*\frac{\omega*\delta}{\epsilon*r}*\left(\frac{\pi*R_O*T}{8M}\right)^{\frac{1}{2}}+\frac{\tau*\delta}{\in}*\frac{p_a}{pD}*\frac{R*T}{M}} \qquad (3.13)$$

Where:

c_m = membrane coefficient $\left(\frac{\text{kg}}{\text{m}^2\text{h Pa}}\right)$

M= molecular weight of the water (18.02 $\frac{kg}{mol}$)

R_o= is the gas constant, R_o =8.314 $\frac{\text{kJ}}{\text{mol K}}$

T=Temperature (K)

The following Equation may be used to compute the water-air PD and pore tortuosity [62]:

$$\omega = \text{pore tortuosity} = \left(\frac{2-\epsilon}{\epsilon}\right)^2 \tag{3.14}$$

$$\text{PD} = 1.895 * 10^{-5} * T^{2.072} \tag{3.15}$$

$$\text{J} = \Delta\text{p} * \text{c}_\text{m} \tag{3.16}$$

J = vapor flux across the membrane (kg/m^2h)

Δp =(Pa) the pressure difference between the evaporation and condensation layers.

The Antoine equation is used to determine the relationship between temperature and vapor pressure (P) in the condensation and evaporation layers [45]:

$$P = \exp(A - \frac{B}{C+T}) \tag{3.17}$$

Where A, B, and C for water are constants with values 23.238, 3841, and -45, respectively [15], vapor pressure is denoted by P (bar), and temperature is denoted by T (K).

$$\text{Q}_{\text{latent heat=}}\text{J.}\, \text{h}_{\text{fg}} \tag{3.18}$$

h_{fg}: latent heat of evaporation of water (kJ/kg)

3.4 FRESH WATER PRODUCTION

According to membrane distillation theory, the vapor flow across the porous hydrophobic membrane, also known as the clean water production rate, can be determined as follows. The two significant assumptions required to reduce Vapor / Liquid Equilibrium (VLE) calculations to Raoult's law are [63]:

1- The vapor phase is an ideal gas.

2- The liquid phase is an ideal solution.

The mathematical expression which reflects the two listed assumptions and gives a quantitative indication of Raoult's law is:

$$y.p = x.P_{sat} \tag{3.19}$$

Where :

x: is a liquid-phase mole fraction

y: is a vapor-phase mole fraction

P_{sat} Vapor-saturated pressure (bar)

P: atmosphere pressure (bar)

The liquid-to-vapor phase mole fraction is the same as pressure to the saturation pressure fraction as in Equation (3.20)

$$\frac{x}{y} = \frac{P}{P_{sat}} \tag{3.20}$$

Rearrange Equation (3.20) yields

$$x = \frac{P}{P_{sat}}.y \tag{3.20a}$$

The summation of the liquid and vapor phases is the unity

$$x + y = 1 \tag{3.21}$$

Substituted the liquid phase by the vapor phase and rearranging Equation 3.21 yields:

$$y = \frac{1}{\frac{p}{P_{sat}}+1} = \frac{1}{\frac{p}{\exp\left(A-\frac{B}{C+T}\right)}+1} \tag{3.22}$$

The vapor that passes through the membrane (Z) equals the water mass flow rate multiplicated by the vapor phase fraction:

$$Z = \dot{m}_{in}.\, y \tag{3.23}$$

From Equations (3.20a), (3.21), and (3.22), the value of x can be determined by:

$$x = \frac{p}{P_{sat}} \cdot \frac{1}{\frac{p}{P_{sat}}+1} \tag{3.24a}$$

$$x = \frac{P}{\exp\left(A-\frac{B}{C+T}\right)} \cdot \frac{1}{\frac{P}{\exp\left(A-\frac{B}{C+T}\right)}+1} \tag{3.24b}$$

Produced water = x .z (3.25)

3.4.1 Concentrated Water Production

The following Equation can calculate the concentrated water production rate:

$$J_s = J_W - J_C \tag{3.26}$$

Where:

J_S: the bleeding water flow rate (kg/m^2 h)

J_W *and* J_C: the source water flow rate and clean water production rate of the multistage membrane distillation system, respectively (kg/m^2 h).

3.5 MATHEMATICAL MODELING OF THE PMD SYSTEM

The governing equations, assumptions, and boundary conditions of the mathematical model of the photovoltaic-membrane distillation (PMD) system are discussed in this section. The simulation model is formulated based on the CFD approach and solved numerically using COMSOL Multiphysics -5.6 software. Figure (3.6) Shows the simulation procedures of the PMD. The meteorological data for Baghdad-Iraq, including global solar radiation, ambient temperature, and air velocity, is taken from Meteonorm software V8.0.3. Three temperatures are calculated for the PMD system; the back cell surface temperature (T_{Cell}), the hydrophilic evaporation layer temperature (T_{Evap}), and the hydrophilic condensation layer temperature (T_{Cond}), as shown in Figure (3.7).

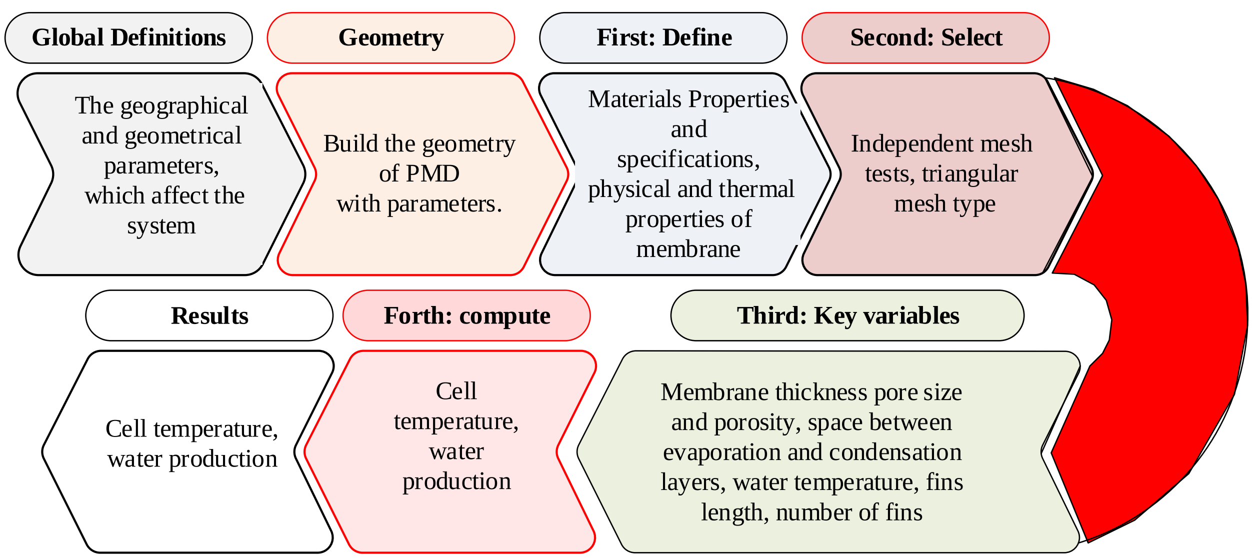

Figure (3.6): The structure of the COMSOL computation processes in detail.

3.5.1 Geometry

COMSOL Multiphysics-designed modeler is used to create the geometric parameters of the PMD model involving solar cell, Aluminum sheet, hydrophilic layer (evaporation), membrane, hydrophilic layer (condensation), aluminum sheet, and heat sink as shown in figure (3-7). Figure (3.8) shows the computational domain of the PMD model. The dimensions of the main parts of the PMD model are listed in Table (3.2).

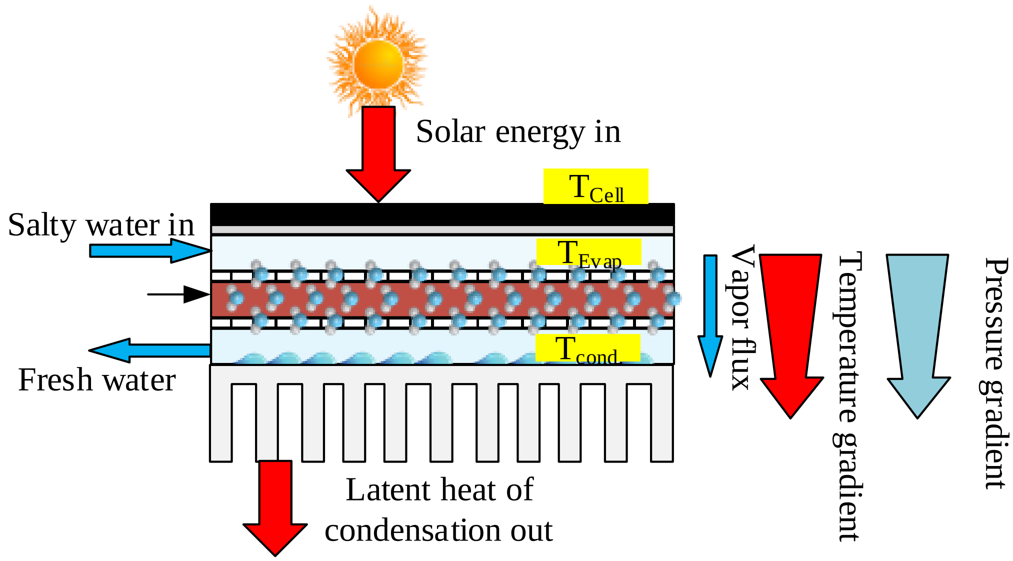

Figure (3.7): Photovoltaic-membrane distillation system.

Table (3.2): Dimensions of the main parts of the PMD model.

Shape	**Dimension**
Solar cell	16×16×0.46 cm
Aluminum sheet (two layers)	16×16×0.07 cm
Hydrophilic layer (evaporation)	16×16×0.1 cm
Steel mesh (two layers)	16 ×16× 0.25 cm
Hydrophobic layer membrane	16×16×0.01 cm
Hydrophilic layer (condensation)	16×16×0.1 cm
Inlet and outlet water tubes diameter	0.035 cm

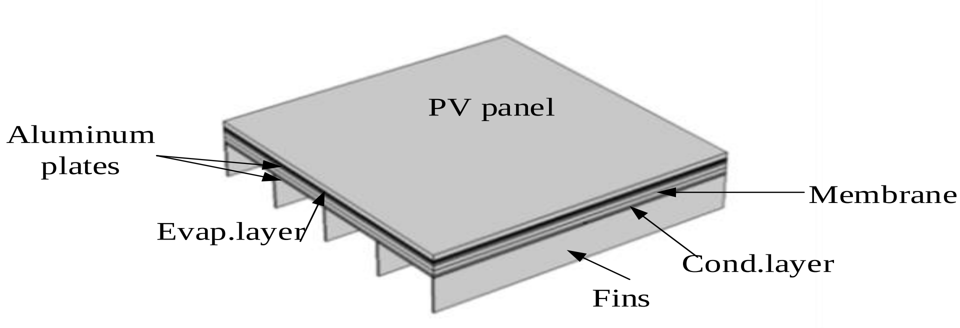

Figure (3.8): Computational domain of the PMD model.

3.5.2 Materials Properties and Specifications

The input physical characteristics of materials used in the PMD model are specified using the COMSOL database, and all the properties are in Table (3.3) as follows.

Table (3.3): Thermophysical properties of materials used in PMD [64].

NO.	Material	Thermal conductivity (W/m K)	Density (kg/m^3)	Specific heat (J/kg.K)
1	Water	0.625	991	4172
2	PTFE	0.25	2200	1050
3	Silicon	148	2330	677
4	EVA	0.35	960	2090
5	Glass	1.8	3000	500
6	TPT	0.2	1200	1250
7	Aluminum	238	2700	900

1- Solar panel consists of five layers, namely Glass covering, two layers of ethylene vinyl acetate (EVA), silicon, and Tedlar, as shown in figure (3.9). The input properties are thermal conductivity (k), density (ρ), and specific heat (C_p), and the dimensions of the main parts of the PV panel as shown in Table 3.4 [64]

Table (3.4): Dimensions of the main parts of the PV panel.

NO.	Material (layer)	Thickness (mm)
1	Glass covering	3.1
2	Two layers of EVA	0.5
3	Silicon	0.4
4	Tedlar	0.1

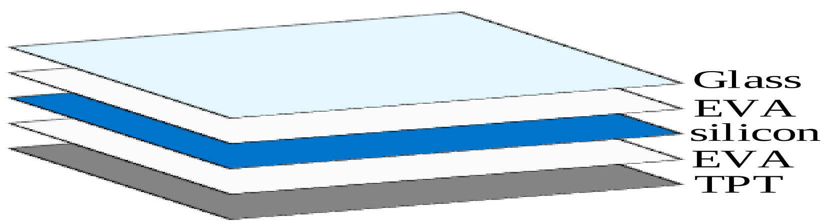

Figure (3.9): Layers of solar panel.

2- Water: for both the hydrophilic layer (evaporation) and the hydrophilic layer (condensation). The input properties are water density (ρ), water-specific heat (C_p), and thermal conductivity k.

3- PTFE: the material from which the membrane is made. The input properties are density(ρ), specific heat (C_p), and thermal conductivity (k).

4- Aluminium: the material that is used for conductive and heat sinks. The input properties are specific heat (C_p) and thermal conductivity (k).

3.5.3 Meshing of the Computational Domain

The meshing of the computational domain for the PMD model is generated by COMSOL Multiphysics-5.6. The User-controlled mesh in the sequence type list in the Settings of a Mesh node is selected, and the meshing sequence builds first. Three types of meshing are found in the software, namely Structured (quad element type), unstructured (triangular element type), or hybrid (a blend of unstructured and structured) components can all be used to interconnect computational domains. The choice of mesh element type depends on the physical characteristics (e.g., turbulent or laminar flows) and the geometry of the problem (e.g., curved or straight). Investigated are the effects of mesh type and density on the precision, effectiveness, and stability of the solution. Three independent triangle mesh tests are carried out for model PMD, from coarse to extra fine triangle mesh element sizes, as shown in Table 3.5.

Table (3.5): Mesh Density models.

No.	Type of element	Number of elements	RAM	Number of minimam elemant
1	Triangular Coarse	359399	1707 MB	0.00123
2	Triangular Normal	712760	3.85 GB	0.00345
3	Triangular Fine	2473531	4.95 GB	0.00596

Unstructured (triangular element type) is used in the current work. Using all domains same mesh takes a lot of time and memory from the computer. So the PVM model is divided into two parts between solid and fluid domains. An extra fine mesh is used for the domain of laminar flow and membrane, and solids such as (solar panels, aluminum, and fins), a normal mesh is used as shown in Fig (3.10).

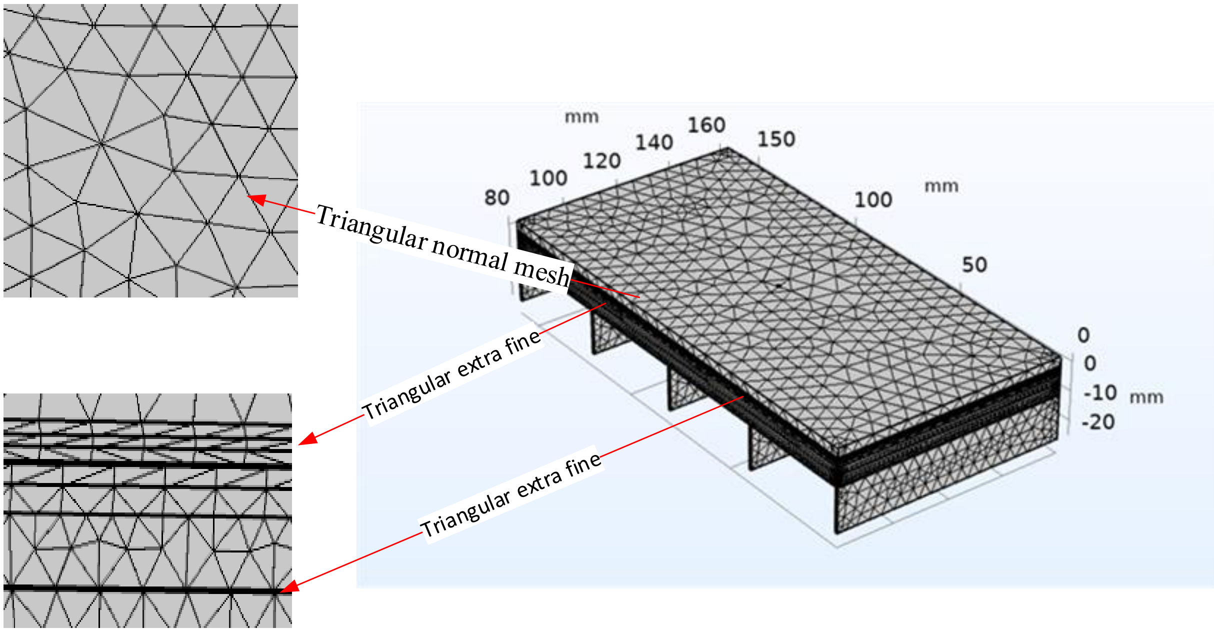

Figure (3.10): Types of meshing final meshing.

3.5.4 Assumptions

The following assumptions are considered in the formulation and solution of the present PMD simulation model:

1- Incompressible and laminar fluid flow through membrane channels.

2- Unsteady state condition with three-dimensional heat transfer for the computational domain.

3- Thermo-physical properties of the fluid are considered temperature-dependent.

4- The physical characteristics of the PTEF membrane, density, viscosity, heat capacity, and thermal conductivity, are assumed constant.

5- The vapor phase is an ideal gas, and the liquid phase is an ideal solution.

6- The temperature of the ambient and solar radiation is time-dependent.

7- The PMD system is perfectly insulated, and the energy loss is neglected.

3.5.5 Governing Equations

The conservation equations of mass, momentum, and energy are the foundation for the governing equations used to determine velocity, pressure, and temperature distributions in the computational domain of the PMD simulation model. These equations can be written as follows [63] and [66]:

I- Continuity equation:

$$\frac{\partial \rho}{\partial t} + \rho\left(\frac{\partial u}{\partial x} + \frac{\partial v}{\partial y} + \frac{\partial w}{\partial z}\right) = 0 \tag{3.26}$$

II- Momentum equation:

$$\rho\frac{\partial u}{\partial t} + \rho(u\frac{\partial u}{\partial x} + u\frac{\partial v}{\partial y} + u\frac{\partial w}{\partial z}) = \mu(\frac{\partial^2 u}{\partial x^2} + \frac{\partial^2 u}{\partial y^2} + \frac{\partial^2 u}{\partial z^2}) + \rho g - \frac{\partial P}{\partial x} \tag{3.27}$$

$$\rho\frac{dv}{dt} + \rho\left(v\frac{\partial u}{\partial x} + v\frac{\partial v}{\partial y} + v\frac{\partial w}{\partial z}\right) = \mu\,(\frac{\partial^2 v}{\partial x^2} + \frac{\partial^2 v}{\partial y^2} + \frac{\partial^2 v}{\partial z^2}) + \rho g - \frac{\partial P}{\partial y} \tag{3.28}$$

$$\rho\frac{\partial w}{\partial t} + \rho(w\frac{\partial u}{\partial x} + w\frac{\partial v}{\partial y} + w\frac{\partial w}{\partial z}) = \mu(\frac{\partial^2 w}{\partial x^2} + \frac{\partial^2 w}{\partial y^2} + \frac{\partial^2 w}{\partial z^2}) + \rho g - \frac{\partial P}{\partial z} \tag{3.29}$$

III- Energy equation:

For fluid flow and solar PV panels.

$$\rho\, C_P\ \frac{\partial T}{\partial t} + \rho\, C_p\left(u\ \frac{\partial T}{\partial x} + v\ \frac{\partial T}{\partial y} + w\ \frac{\partial T}{\partial z}\right) = k\ \left(\frac{\partial^2 T}{\partial x^2} + \frac{\partial^2 T}{\partial y^2} + \frac{\partial^2 T}{\partial z^2}\right) + Q_{IN} \tag{3.30}$$

$$\frac{\rho Cp}{k}\frac{\partial T}{\partial t} = \frac{\partial^2 T}{\partial x^2} + \frac{\partial^2 T}{\partial y^2} + \frac{\partial^2 T}{\partial z^2} \tag{3.31}$$

The conservation equations inside the porous media (membrane and microchannels) through the layers of the PMD system can be expressed by[45]:

I- Continuity equation:

$$\frac{1}{\epsilon}\frac{\partial\rho}{\partial t} + \rho\left(\frac{\partial u}{\partial x} + \frac{\partial v}{\partial y} + \frac{\partial w}{\partial z}\right) = 0 \qquad (3.32)$$

II- Momentum equation:

$$\frac{1}{\epsilon}\rho\frac{\partial u}{\partial t} + \frac{1}{\epsilon^2}\rho\left(u\frac{\partial u}{\partial x} + v\frac{\partial u}{\partial y} + w\frac{\partial u}{\partial z}\right) = -\frac{\partial p}{\partial x} + \frac{\mu}{\epsilon}\left(\frac{\partial^2 u}{\partial x^2} + \frac{\partial^2 u}{\partial y^2} + \frac{\partial^2 u}{\partial z^2}\right) - \frac{\mu}{K}u - \frac{\rho_f Cf}{\sqrt{K}}|u|u \qquad (3.33)$$

$$\frac{1}{\epsilon}\rho\frac{\partial v}{\partial t} + \frac{1}{\epsilon^2}\rho\left(u\frac{\partial v}{\partial x} + v\frac{\partial v}{\partial y} + w\frac{\partial v}{\partial z}\right) = -\frac{\partial p}{\partial y} + \frac{\mu}{\epsilon}\left(\frac{\partial^2 v}{\partial x^2} + \frac{\partial^2 v}{\partial y^2} + \frac{\partial^2 v}{\partial z^2}\right) - \frac{\mu}{K}v - \frac{\rho_f Cf}{\sqrt{K}}|v|v \qquad (3.34)$$

$$\frac{1}{\epsilon}\rho\frac{\partial w}{\partial t} + \frac{1}{\epsilon^2}\rho\left(u\frac{\partial w}{\partial x} + v\frac{\partial w}{\partial y} + w\frac{\partial w}{\partial z}\right) = -\frac{\partial p}{\partial z} + \frac{\mu}{\epsilon}\left(\frac{\partial^2 w}{\partial x^2} + \frac{\partial^2 w}{\partial y^2} + \frac{\partial^2 w}{\partial z^2}\right) - \frac{\mu}{K}w - \frac{\rho_f Cf}{\sqrt{K}}|w|w \qquad (3.35)$$

III- Energy equation:

$$\rho\, c_p\, \epsilon\frac{\partial T}{\partial t} + \rho\, c_p\left(u\frac{\partial T_1}{\partial x} + v\frac{\partial T}{\partial y} + w\frac{\partial T}{\partial z}\right) = k_{f,eff}\left(\frac{\partial^2 T}{\partial x^2} + \frac{\partial^2 T}{\partial y^2} + \frac{\partial^2 T}{\partial z^2}\right) + h_{sf}\, a_{sf}\,(T_s - T_f) \qquad (3.36)$$

Where μ is dynamic viscosity, ρ is density, and u, v, and w are velocity components in x, y, and z directions, respectively.

3.5.6 Operating Parameters and Boundary Conditions

3.5.6.2 Boundary Conditions:

Based on the computational domain shown in Figure (3.11), the boundary conditions for fluid and solid wall are as follow:

1. Fluid flow:
   - Inlet: V_{in}=7.8*10^{-8}, T_{in}=25℃, ρ_{in} =981 kg/m^3, and C_p =4.2kJ/kg for water.
   - Outlet: outlet pressure is identified at the water outlet.
2. Solid surface (Walls):
   - No slip condition on solid walls (u= 0, v= 0, w= 0).
   - No thermal jump on the wall.
   - Adiabatic condition for insulated surfaces (q= 0, or dq= 0).
3. Membrane:
   - The boundary walls are non-slip conditions and the sides of the membrane
   - layers are assumed to be thermally insulated.
   - The interfaces between the membrane and the channels are considered coupled interfaces.
4. Solar PV panel:
   - The PV panel's top surface is subjected to solar radiation G (W/m^2).
   - Convection and radiation heat transfer occur at the top surface of the PV panel.
   - Conductive heat transfer occurs through the layers of solar PV panels, with neglected thermal contact resistances between the panel layers.

- The aluminum sheet attached to the back surface of the solar PV panel is assumed to be a heat sink, and it is in perfect contact with the back of the PV panel.

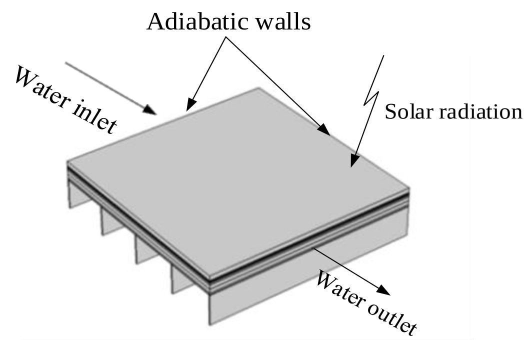

Figure (3.11): Boundary conditions of the PVM model computational domain.

3.5.6.2 The critical variables under study

Many key variables affect the performance of PMD. The variables are geometric conditions, namely, membrane thickness, space between membrane and evaporation layer, fin thickness, and the number of fins. The second key variables are the operation conditions, namely, water temperature. Figure (3.12) shows the flow chart of the theoretical simulation. The range and steps of the mentioned variables are:

1. Membrane thickness in the range of 0.1 to 1mm, step 0.1 mm.
2. Space between membrane and evaporation layer in the range of 1 to 3 mm, step 0.5 mm.
3. Fins height in the range of 1 to 4 Cm, step 0.5 Cm.
4. Number of fins, namely 5, 11, and 16
5. Water inlet temperature 20 to 40 ^oC, step 10 ^oC.

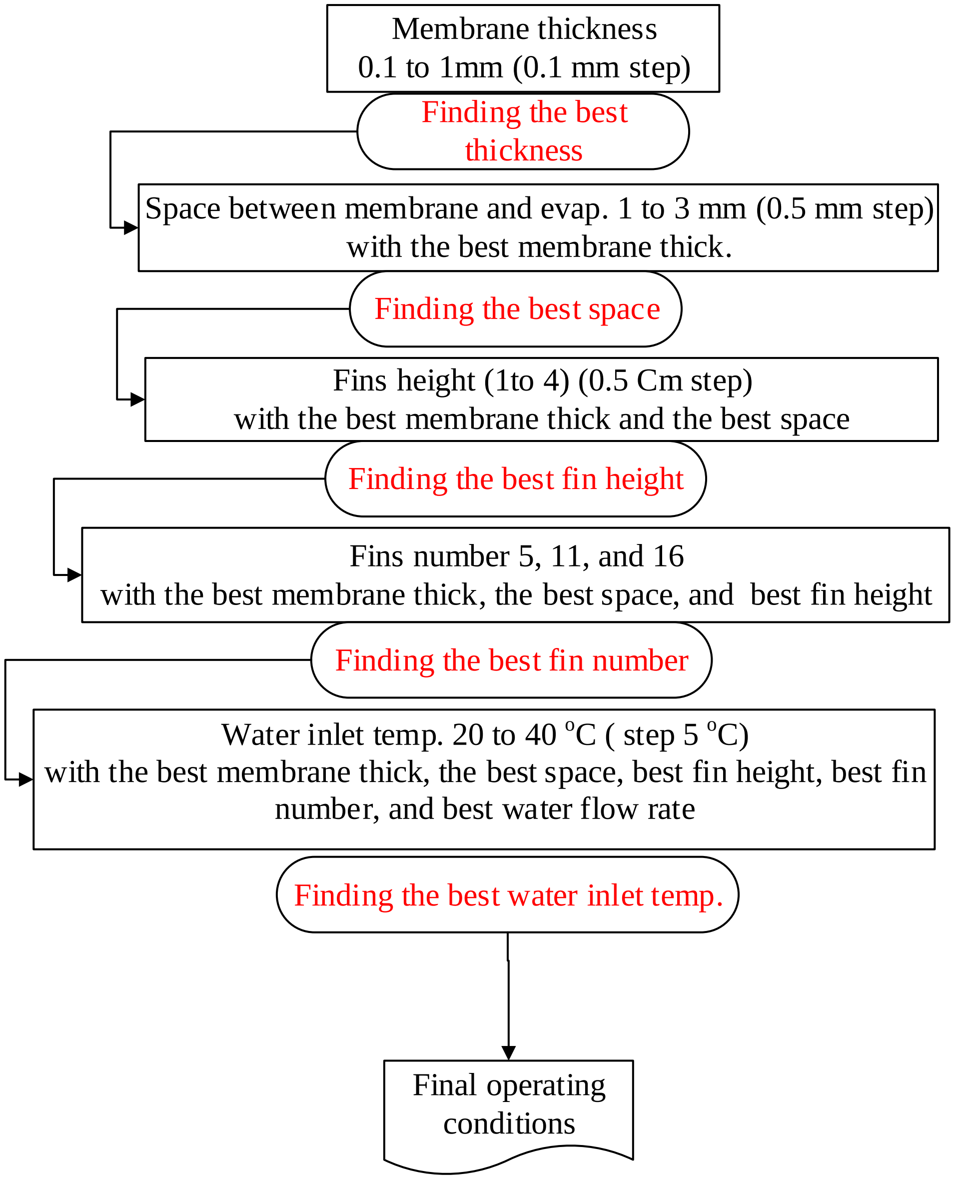

Figure (3.12): Flowchart of the theoretical simulation.

3.6 FINITE ELEMENT METHOD

As illustrated in Fig. 3.13, the significant stages of the finite solution methodology are stated below to summarize how the finite element method works briefly. Fig. 3.13: The algorithm of the present numerical investigation.

1. Transforming the conservation physics from a partial differential equation perspective into a matrix for the finite element approach.

2. Distributing the physical properties as a function of reference conditions introduced as a data table or polynomial.

3. Locate the characteristics of the element. The mesh-dependent analysis comes after the boundary conditions based on operational circumstances.

4- The study type selection if it is steady state (stationary) or transient (time-dependent.

3.7 ITERATIONS NUMBER AND CONVERGENCE CRITERION

To ensure the calculation advancement is going in the appropriate direction, iteration convergence should be checked as one of the key indications of the simulation calculation to get the desired results. The solution is stopped by the COMSOL Multiphysics-5.6 solver when the residuals reach their specified values or after iterations. In the present analysis, the solution is considered converged when the residuals are under a set tolerance limit of 10 ^{4} for velocity and pressure and temperature for 10^{-8}, as shown in Figure (3.14). It can be observed that the monitoring residuals for each variable are stable, which proves a steady state for the numerical solution results. The step time is 30 min.

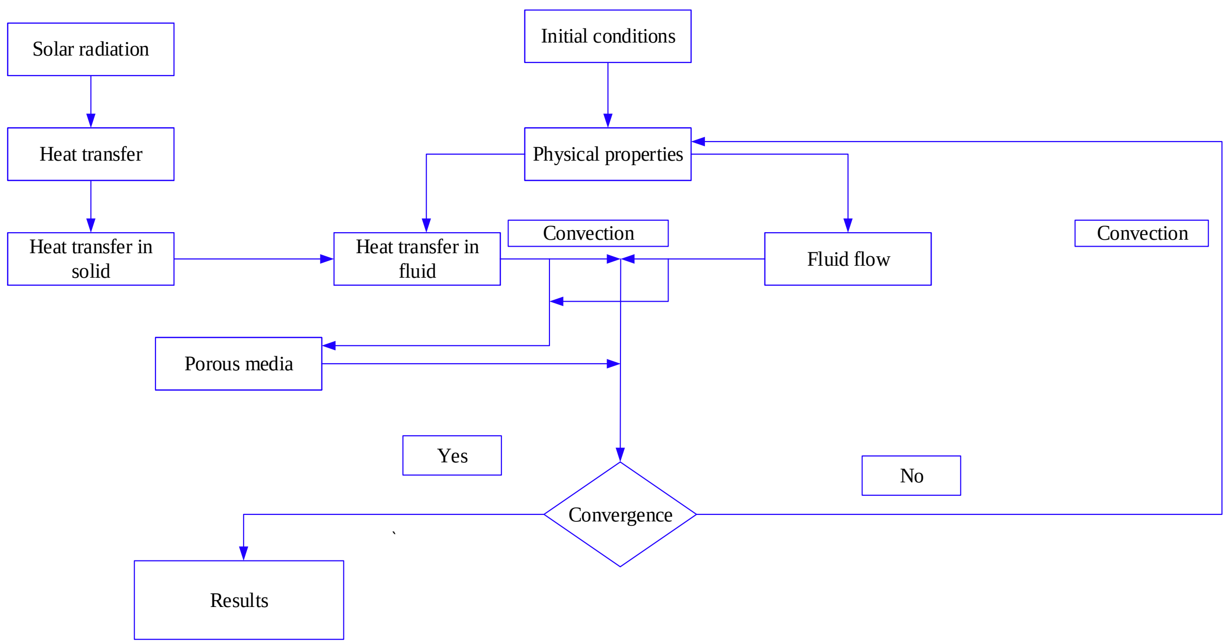

Figure (3.13): The main steps of the numerical solution.

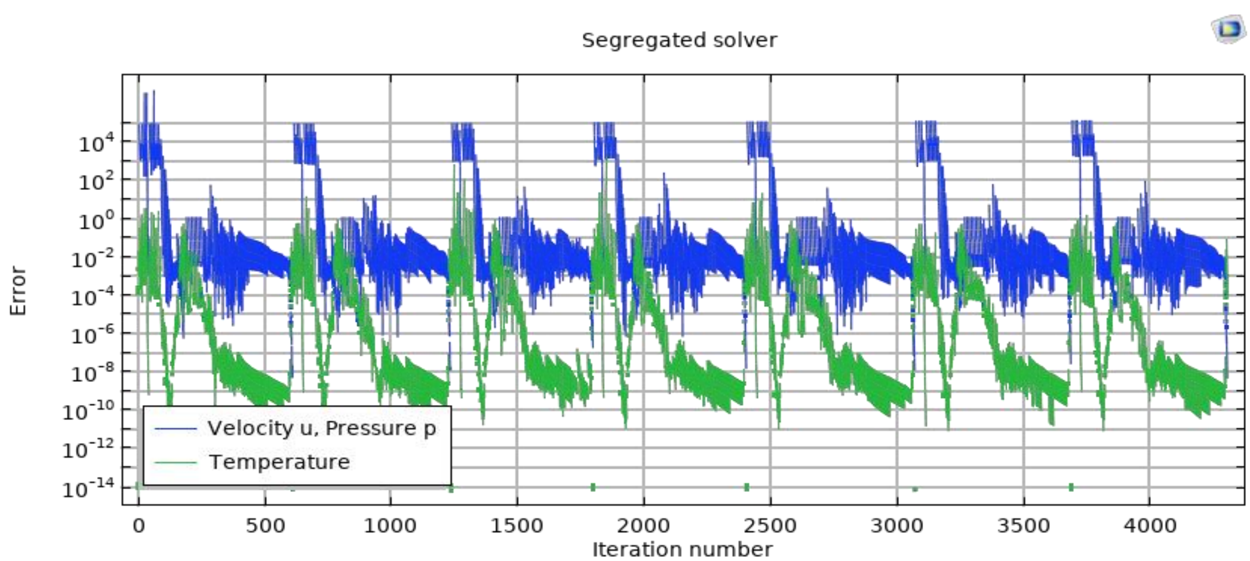

Figure (3.14): Residuals for the converged numerical solution.

Chapter Four
Experimental Work

Chapter Four

Experimental Work

4.1 INTRODUCTION

From an economic point of view, it is recommended to conduct preliminary experiments in two tracks. The first is the numerical simulation discussed in chapter three of the current thesis. The second branch is the indoor test, carried out on a small-scale rig to find the best operating condition PMD system. After finding the best operating condition, moving to the field test is possible, through which the best case is studied on a full-scale rig. In this chapter, the indoor and field PMD rigs are explained.

4.2 The INDOOR PROTOTYPE PMD SYSTEMS

Five indoor prototypes of the PMD system are manufactured. The first is a standard PV solar system without any cooling devices; the other four rigs are integrated with a PMD system. The difference between the other four rigs is the pore size of the membrane used.

4.2.1 The prototype single-stage PMD

The prototype single-stage PMD shown in Figures (4.1), (4.2), and (4.3) is built from the following components from top to bottom. The first layer is a 140 × 165× 17 mm PV solar panel of type ST2-2W; the rated maximum power is 2W, and the current and voltage at maximum power are 222 mA, and 9V, respectively. The short circuit current and the open circuit voltage are 245 mA and 0.8 V, respectively. Figure (4.4) shows the PV panel and Table 4.1 shows the specification of the PV panel. It is worth noting that all the variables that affect the temperature of the cells and the water productivity are studied simultaneously, so five rigs are manufactured;

that is, it requires the use of five solar panels of the mentioned PV solar panel. The second and last layer is the aluminum plate used to enhance the contact between the membrane and the solar panel for the second layer and to improve heat rejection in the last layer. The dimensions of the aluminum plate are 110× 140× 0.7 mm. The third layer is the hydrophilic layer (a stainless steel mesh) used as an evaporation layer of dimensions of 110 × 140× 1 mm. The water used to cool the solar cell diffuses to moisten this layer, which facilitates the evaporation of water. A hydrophobic membrane of dimensions 110× 140× 0.1 mm is separated from the third layer by a polymer mesh of 2.5 mm thickness; this layer is used to permit only the water vapor to transfer from the evaporation layer. Another polymer layer separates the membrane from the condensation layer, where the water vapor condenses on this layer. Finally, the last aluminum plate rejects the latent heat of condensation.

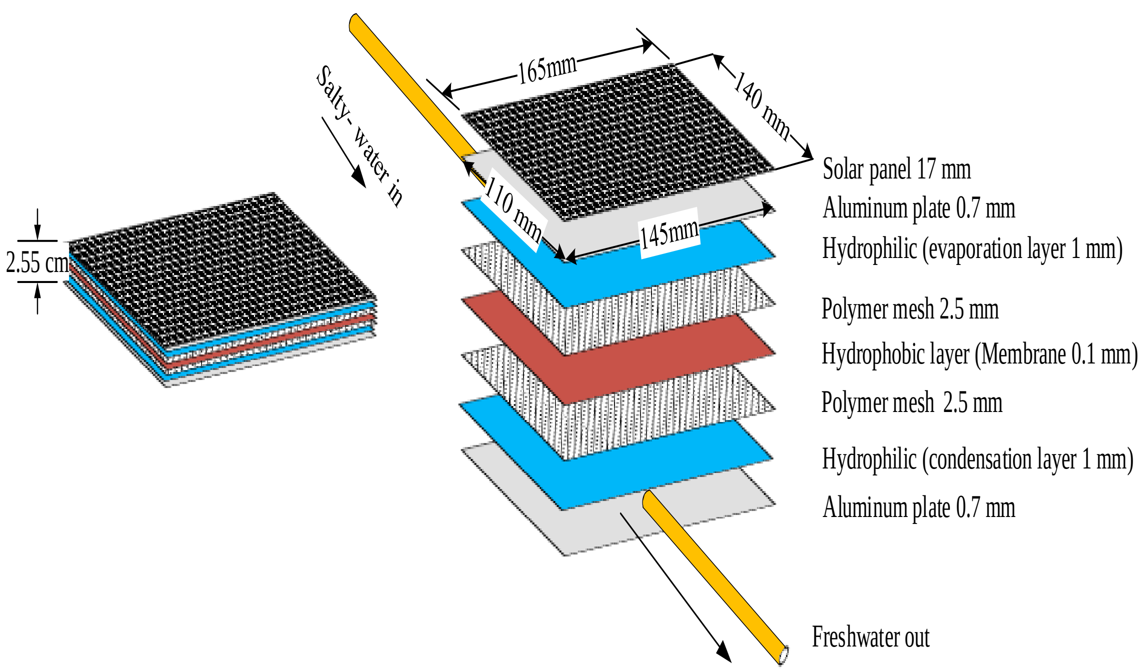

Figure (4.1): The layers of the PMD system.

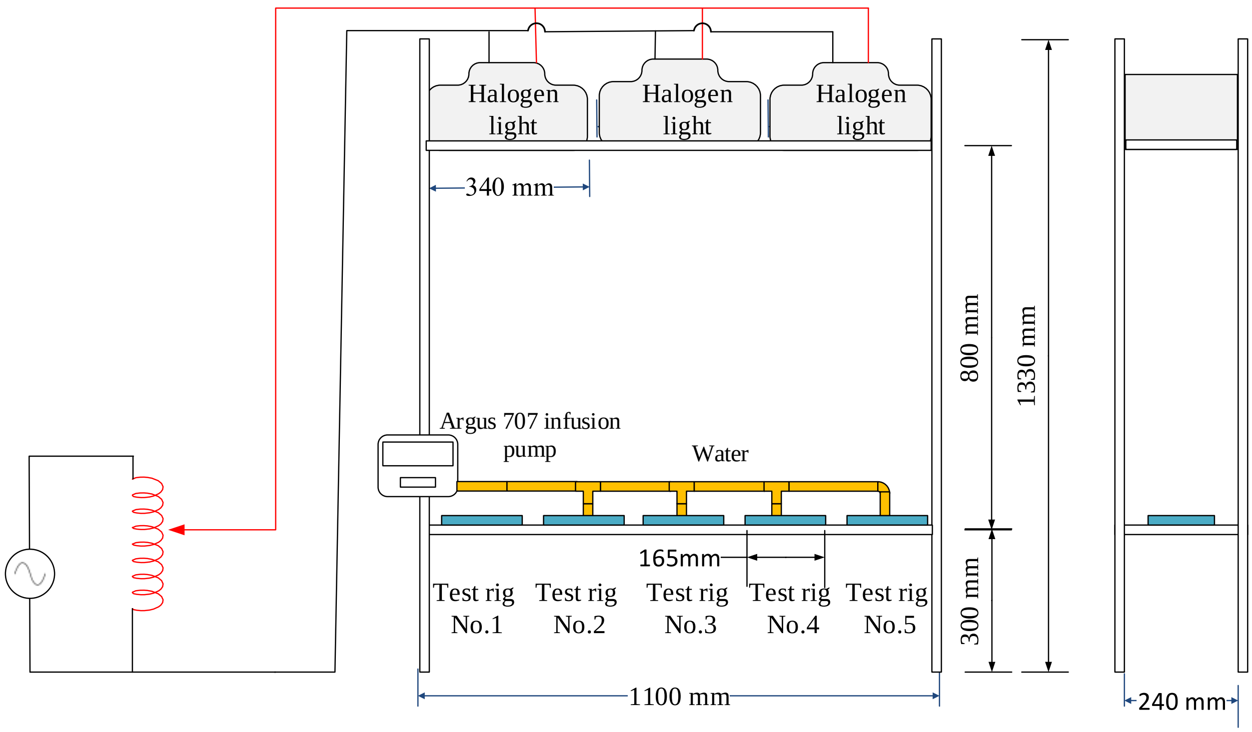

Figure (4.2): Schematic diagram of the indoor test rig.

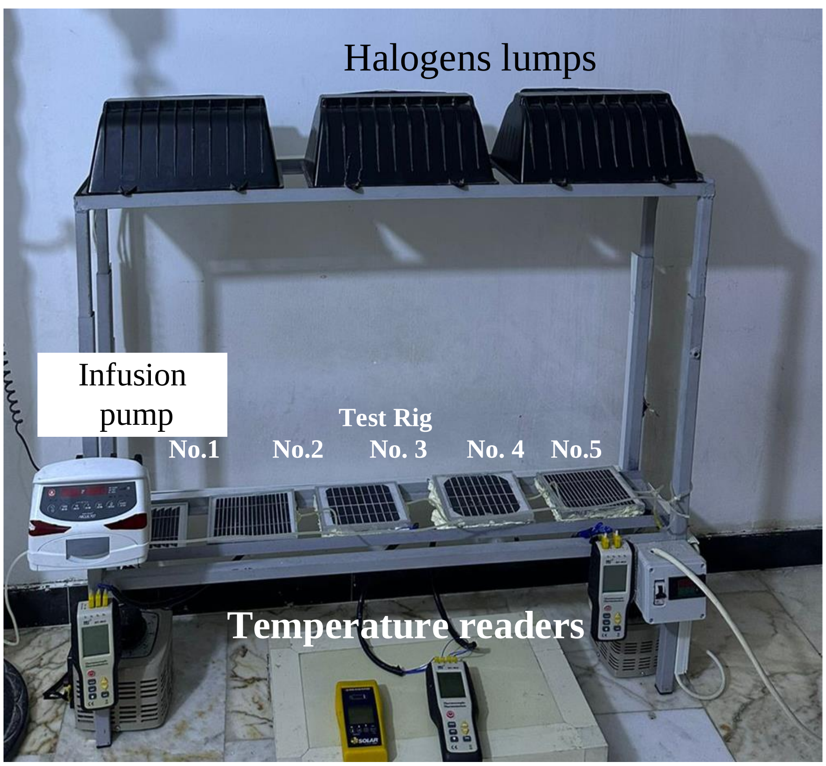

Figure (4.3): Photograph of the indoor test rig.

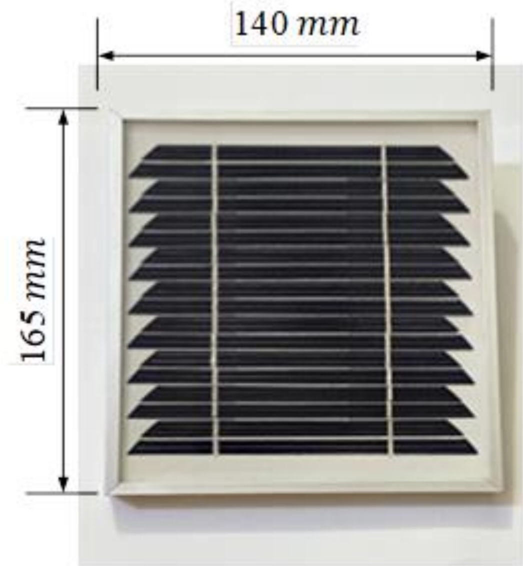

Figure (4.4): The PV solar panel used in the indoor test.

Table (4.1): Specifications of the PV solar panel used in the indoor test.

Model	**ST2-11-011475 L**
Rated maximum power (p_{max})	2W
Current at Pmax (I_{mp})	222mA
The voltage at Pmax(V_{mp})	9V
Short Circuit Current (I_{sc})	245 mA
Open Circuit Voltage (V_{oc})	10.8 V

4.2.2 Halogen lights and variac

Three 500 W power generate halogen lumps each are used to simulate the solar radiation. The lumps are in the wavelength range of 360- 2500 nm and radiate at the black body's temperature of 3200 K; thus, it coincides with the sunlight spectrum, especially in the thermal radiation region [67]. A halogen lamp's components—a tungsten lamp, a glass cover, and an integrated reflector made from an aluminum plate, ensure safe operation and minimize irradiance losses. The specification of the Halogen modules is shown in Table 4.2. The intensity of the lumps is controlled using two Voltage regulators (Variacs) in the voltage range of 0 to 300 V, with an Accuracy+/- 2 Volte. Input frequencies 50Hz, 60Hz, and up to 2000 Hz can be accommodated. Figures 4.5 and 4.6 show the halogen lamp and the variac.

Figure (4.5): The halogen lump.

Figure (4.6): The variac.

Tabel (4.2): Specification of light halogen.

Model	**IP44**
Wattage	500W
Voltage	220-240 v
Frequency	50-60 Hz
Light bulb technology	Halogen
Body material	Aluminium

4.2.3 Infusion pump

Water is used to cool the solar panel cells, so the water flow rate should be controlled to benefit from the heat withdrawn from the solar cells to evaporate the water. Since the area of the solar panel used in the indoor test is very small, it requires control of the water flow rate to the panel, and at first, a valve was used to control the water flow rate, but the use of the valve was insalfied, so an infusion pump was used. An infusion pump of type ARGUS 707 with a flow rate of 0.1 to 999.9 ml/h is used. The water flow rate is controlled by controlling the pump's ON/OFF, of 0:01 to 99:59 hours, in a time step of one minute. The Infusion pump is powered by a rechargeable battery of 2 V DC. Figure (4.7) shows the Infusion pump. The specification of the Infusion pump is shown in Appendix A.

Figure (4.7): The infusion pump.

4.2.4 Membranes

The primary variable under study for the current work is the membrane material type, where four pore sizes of membranes are tested. The first two types are polytetrafluoroethylene polymer (PTFE) membranes with pore sizes of 0.45 and

1μm and Porosity of 0.84-0.86, while the second type is Polyvinylidene fluoride (PVDF) membranes with pore sizes of 3 and 5μm. For each membrane size, a test rig is fabricated in addition to a rig containing a solar cell that works without cooling. As mentioned previously, five laboratory devices are operating simultaneously. Table (4.3) shows the properties of the membranes. Each type of membrane is scanned using scanning electron microscopy (SEM), as shown in Figures (4.8) to (4.12). The figures indicate the pore size and the fiber diameter.

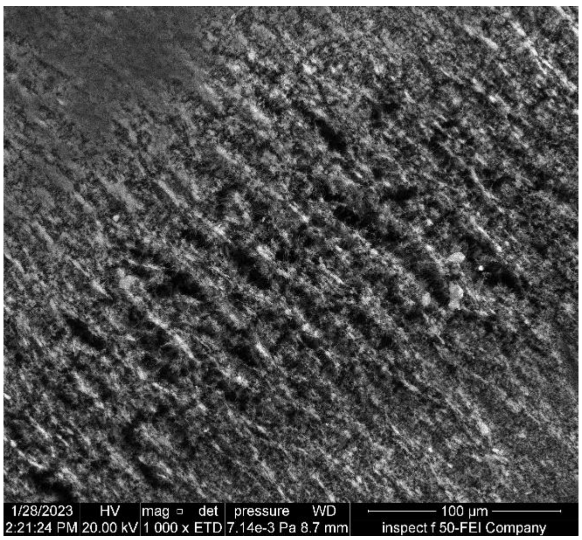

a. 100 μm inspect, 0.45 μm pore size

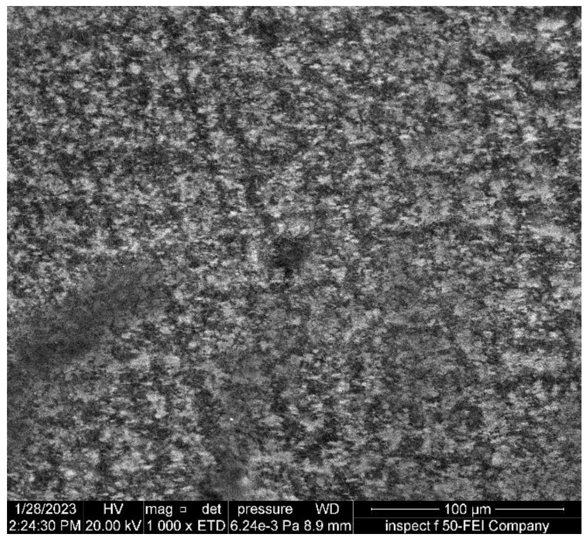

b. 100 μm inspect, 1 μm pore size

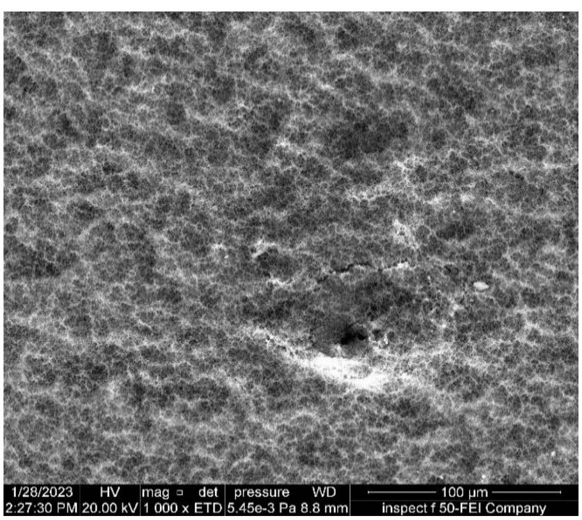

c. 100 μm inspect, 3 μm pore size

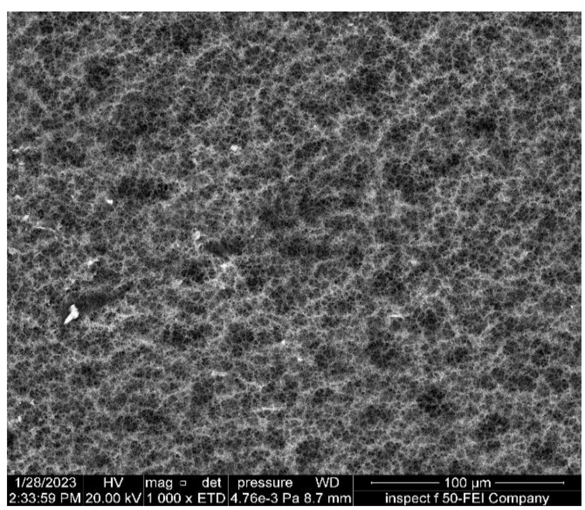

d. 100 μm inspect,5 μm pore size

Figure (4.8): Surface SEM images of Membrane Types, 100 μm inspect.

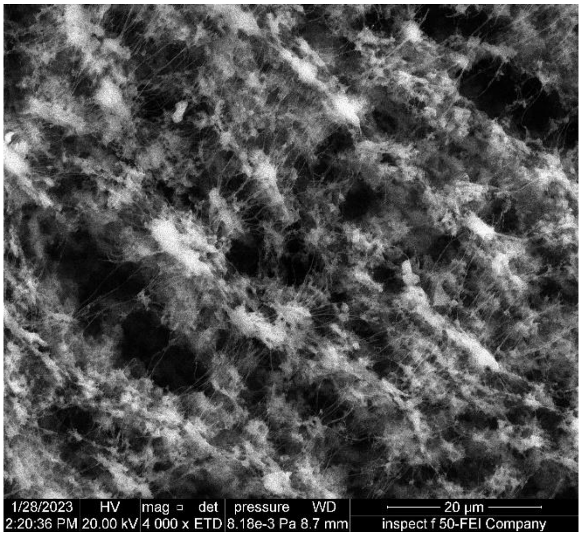

a. 20 μm inspect, 0.45 µm pore size

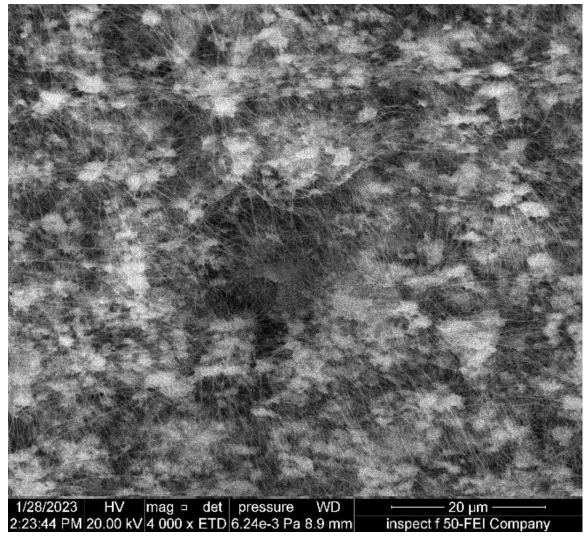

b. 20 μm inspect, 1 µm pore size

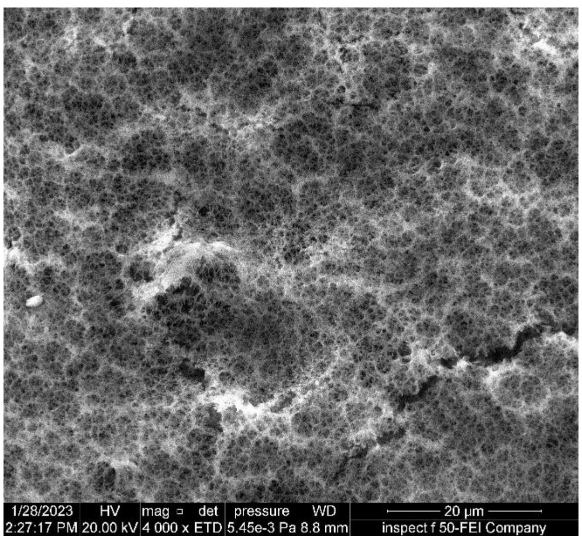

c. 20 μm inspect, 3 µm pore size

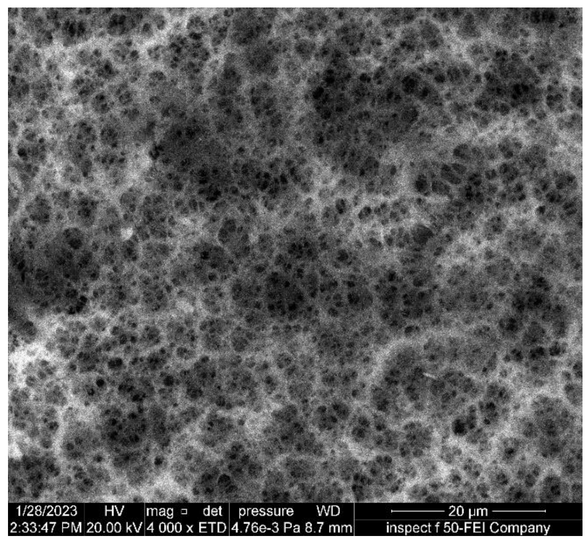

d. 20 μm inspect,5 µm pore size

Figure (4.9): Surface SEM images of membrane types, 20 μm inspect.

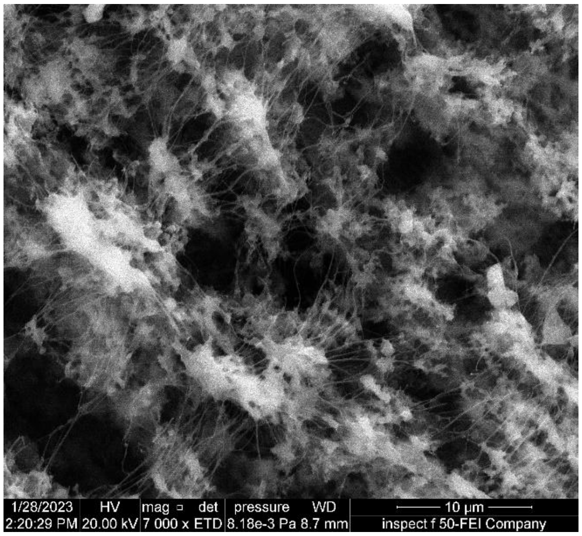

a. 10 μm inspect, 0.45 µm pore size

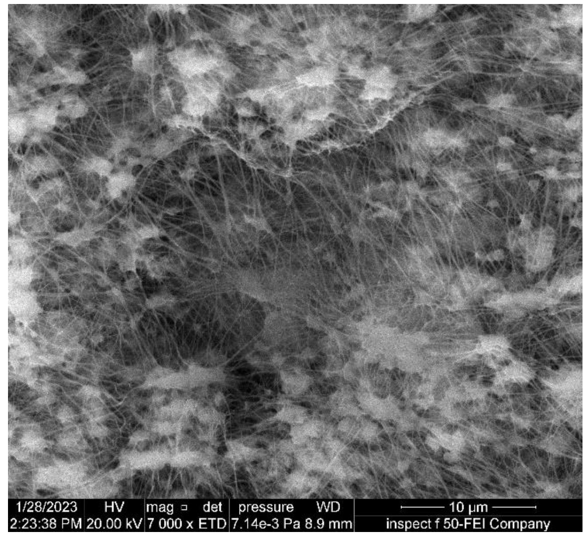

b. 10 μm inspect, 1 µm pore size

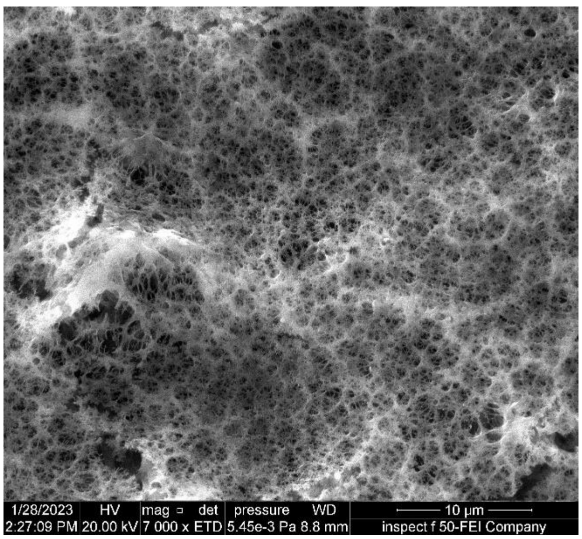

c. 10 μm inspect, 3 µm pore size

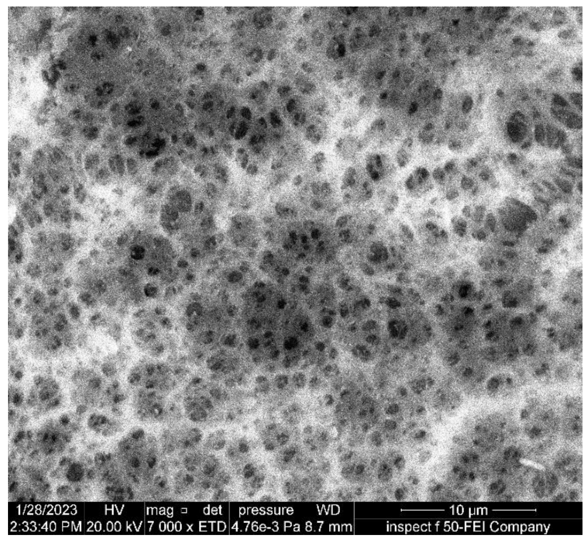

d. 10 μm inspect,5 µm pore size

Figure (4.10): Surface SEM images of membrane types, 10 μm inspect.

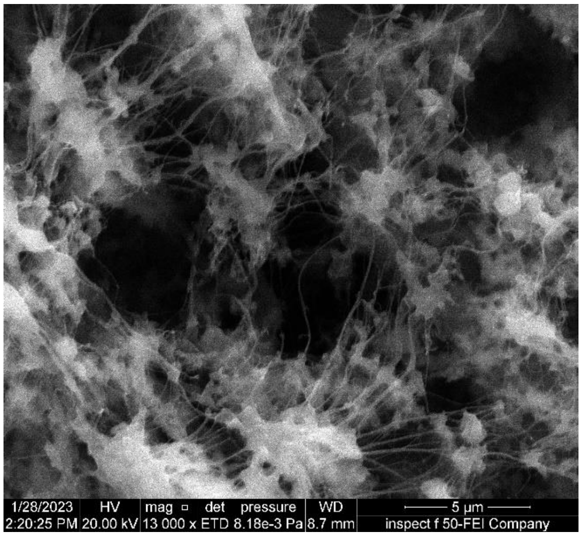

a. 5 μm inspect, 0.45 µm pore size

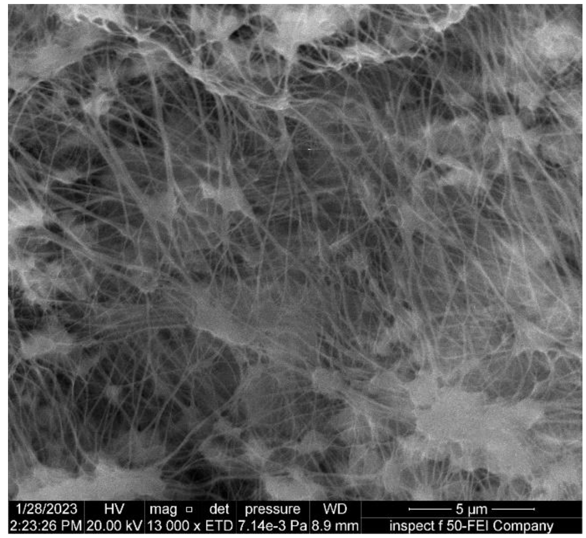

b. 5 μm inspect, 1 µm pore size

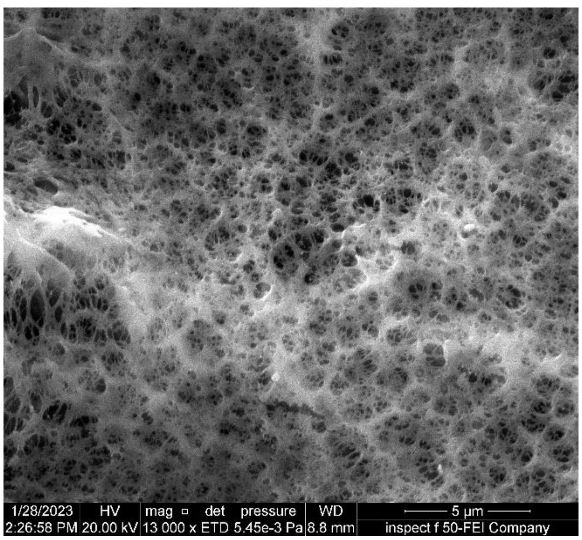

c. 5 μm inspect, 3 µm pore size

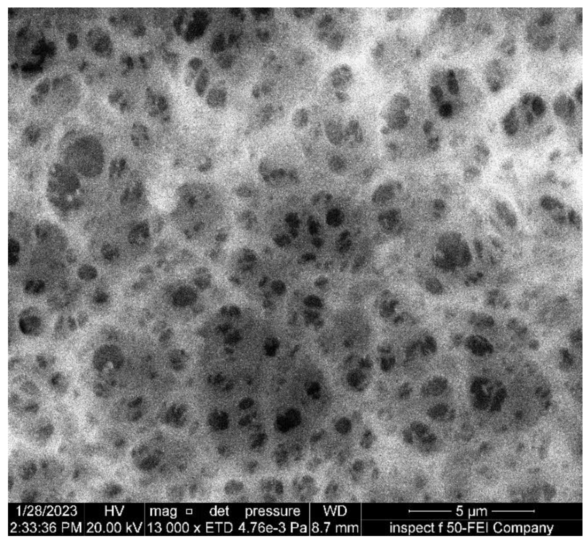

d. 5 μm inspect,5 µm pore size

Figure (4. 11): Surface SEM images of membrane types, 5 μm inspect.

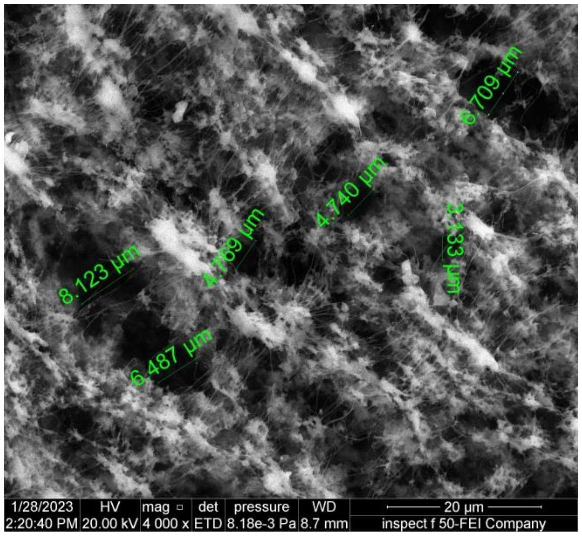

a. 20 μm inspect, 0.45 µm pore size

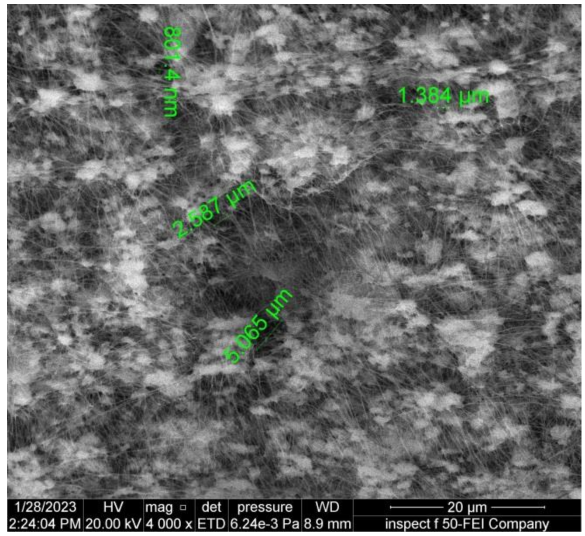

b. 20 μm inspect, 1 µm pore size

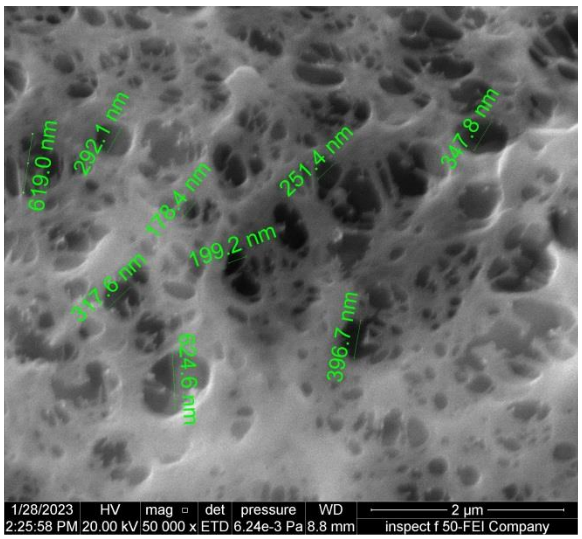

c. 2 μm inspect, 3 µm pore size

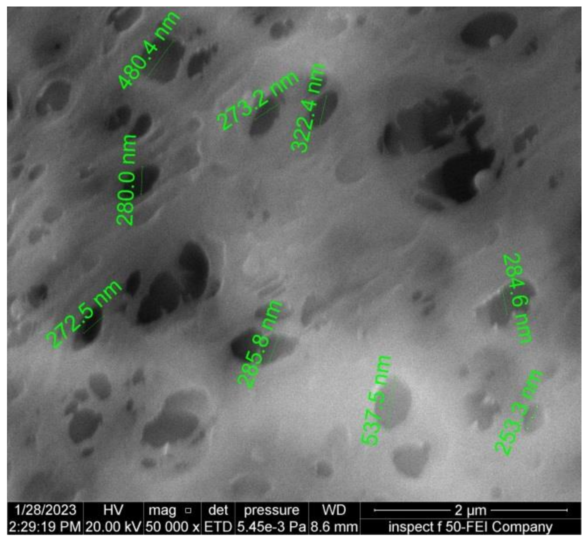

d. 2 μm inspect,5 µm pore size

Figure (4.12): Surface SEM images of membrane types for different inspects showing the wire diameters.

Table (4.3): Specifications of membrane

Filter media	**Hydrophobic PTFE, PVDE**
Pore size	PTFE : 0.45µm, 1µm PVDE : 3µm and 5µm
Bubble point	7 kPa
Flow rate	6 ml/min.Cm
Thickness	0.1 mm
PH Range	1-14

4.2.5 Additional Material

Additional materials are used to fabricate the test rig; these materials are:

4.2.5.1 hydrophlic Layer

The hydrophilic layer, of hole size 27 ×27 μm, and a wire diameter of 24 μm, is made of stainless steel of type 316. This layer is a water-loving layer that is used as an evaporation and condensation layer in the rig. Figure (4.13) shows the hydrophilic layer.

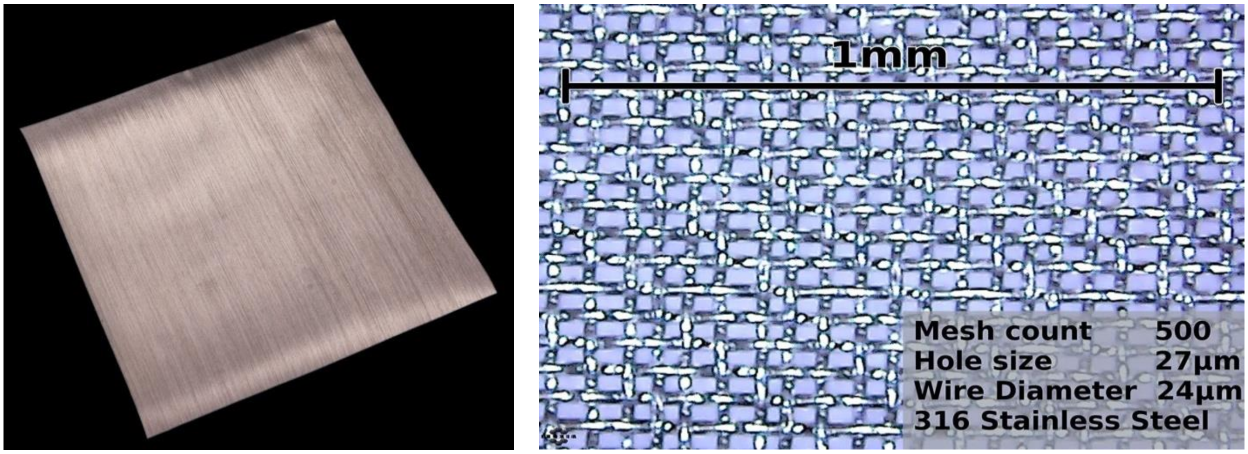

Figure (4.13): The hydrophilic layer.

4.2.5.2 The Polymer Mesh Layer

The polymer mesh aims to create space between the hydrophobic and hydrophilic layers. This layer can generate pressure differences; as a result, the driving force of vapor can pass through the membrane. Figure (4.14) shows the polymer layer.

4.2.6 The Steel Frame

The 5 test rigs, the three halogens lumps, the infusion pump, and the instruments are installed on a steel frame of 1100 mm long, 240 mm wide, and 1330 mm height for indoor testing. The outdoor devices are also installed on a steel frame of 1100 mm long, 670 mm wide, and 1100 mm height. The structure comprises angle and rectangular steel tubes of 25× 25× 3 mm dimensions. Figures (4.3) and (4.18) show the steel frame.

4.3 THE OUTDOOR PMD RIG.

From the result of the indoor test, the best membrane pore size is selected to perform the outdoor test rig. The outdoor test rig layer is the same as that for the indoor rig, but the dimensions of the layers are equal to the dimensions of the PV panel, which is 670 mm ×540 mm ×46 mm and the tube was inserted into the opposite side of the inlet water, serving as an outlet for the water from the first layer as shown in Figure 4.17. Two identical solar PV panels of type FRS-50W are used to build the outdoor rig. The first rig is a standard rig which is the PV panel not cooled, while the second rig is equipped with a PMD system. The power of the PV panel is 50 W, the maximum power current is 2.8A, the maximum power voltage is 18V, the short circuit current is 3.7A, and the open circuit voltage is 22V. The specification of the solar panel is shown in Table 4.5. Figure (4.15) shows the PV panel.

The two rigs, the infusion pump, and the instrumentation are installed on a steel frame of dimensions 1100 length, 670 mm width, and 1000 mm height. The two solar panels are installed on a movable frame of 1100×670 mm. The frame's tilt angle can be adjusted to match the solar altitude angle of about 35°. Figures 4.16 and 4.18 show the outdoor test rig.

Table (4.4): Summarizes the Dimensions of the Indoor and Outdoor rigs.

No.	Components	Simulation device	Outdoor experimental
1	solar panel	140 mm×165 mm×17mm	670 mm ×540 mm ×46 mm
2	Membrane	110mm×140 mm×0.1mm	580 mm×500 mm ×0.1 mm
3	Aluminum plate	110mm×140 mm×0.7mm	580 mm×500 mm ×0.7 mm
4	Stainless steel mesh	110mm×140 mm×1mm	580 mm×500 mm ×1 mm
5	Polymer layer	110mm×140 mm×2.5mm	580 mm×500 mm ×2.5 mm
6	Tube of inlet water	Dim.= 3.7 mm ,L= 50mm	Dim.= 3.7mm , L=1 50 mm

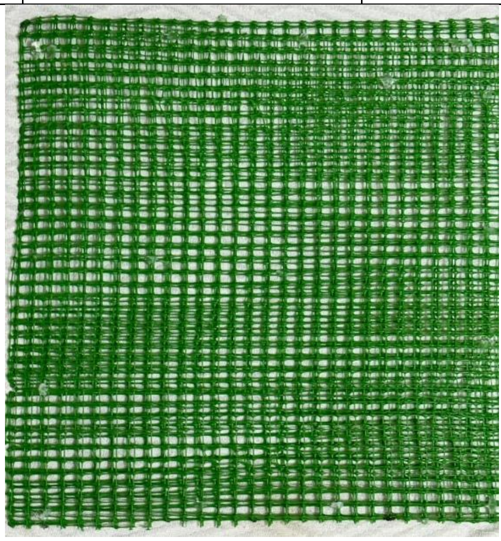

Figure (4.14): Polymer layer.

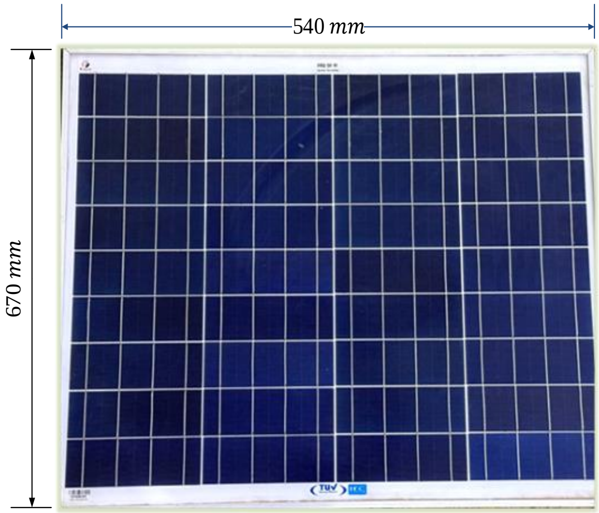

Figure (4-15): The solar PV panels.

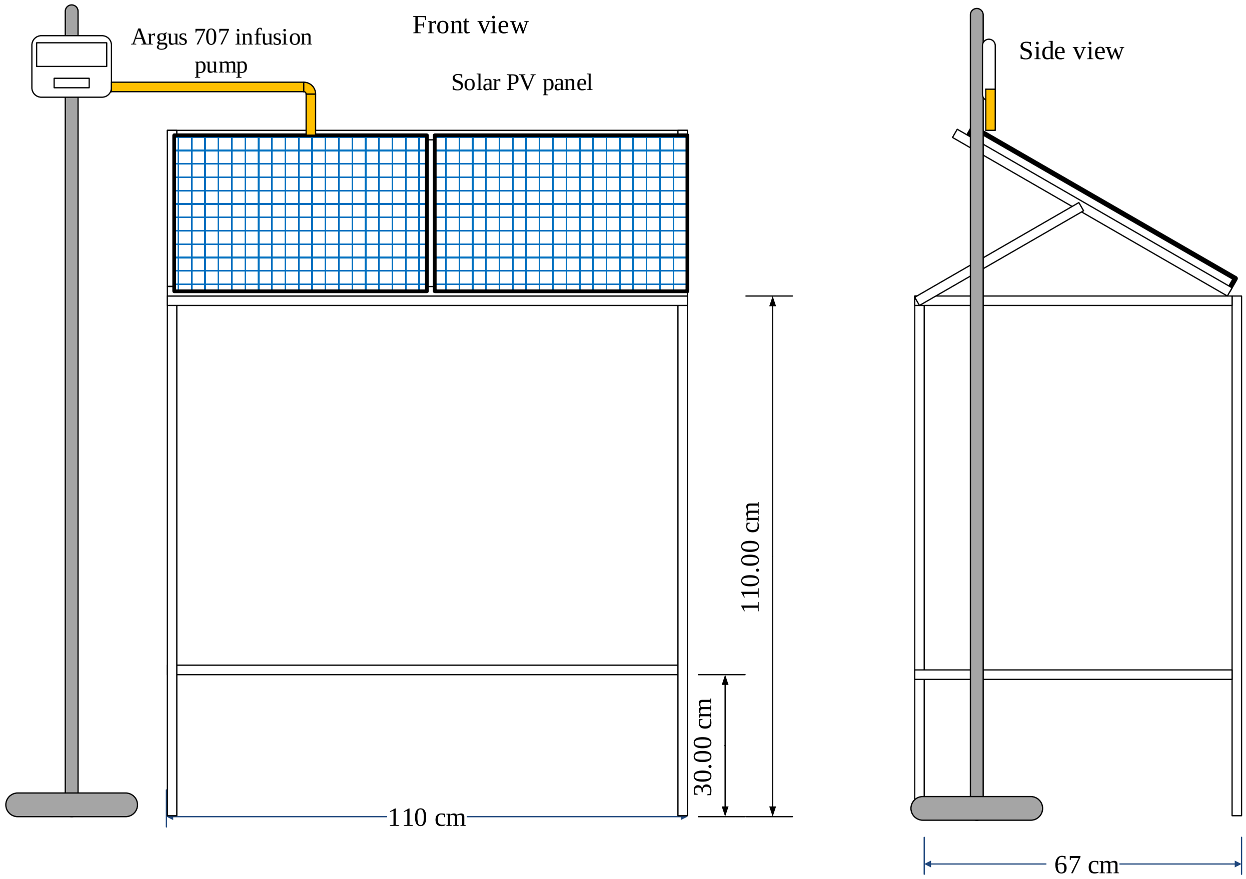

Figure (4.16): Schematic diagram of the outdoor test rig.

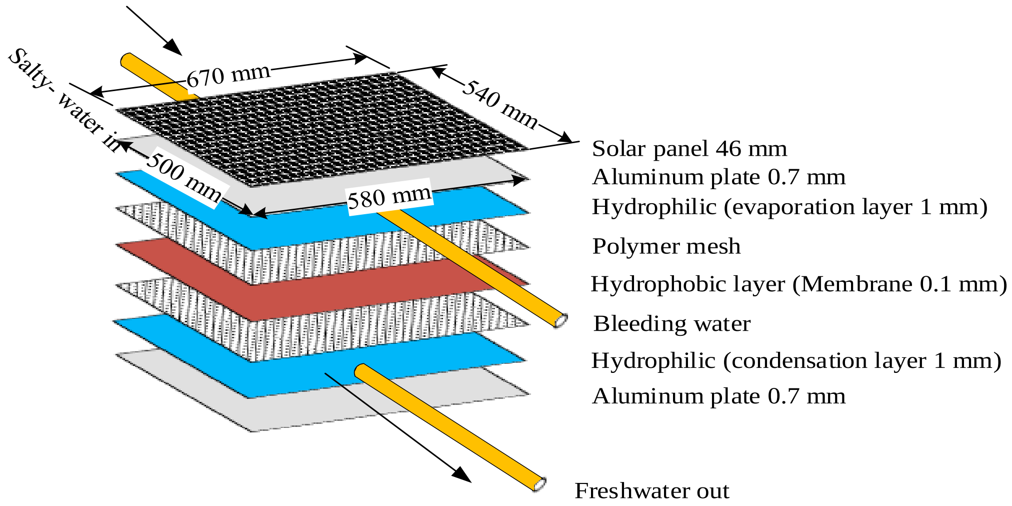

Figure (4.17): The layers of the PMD system outdoors.

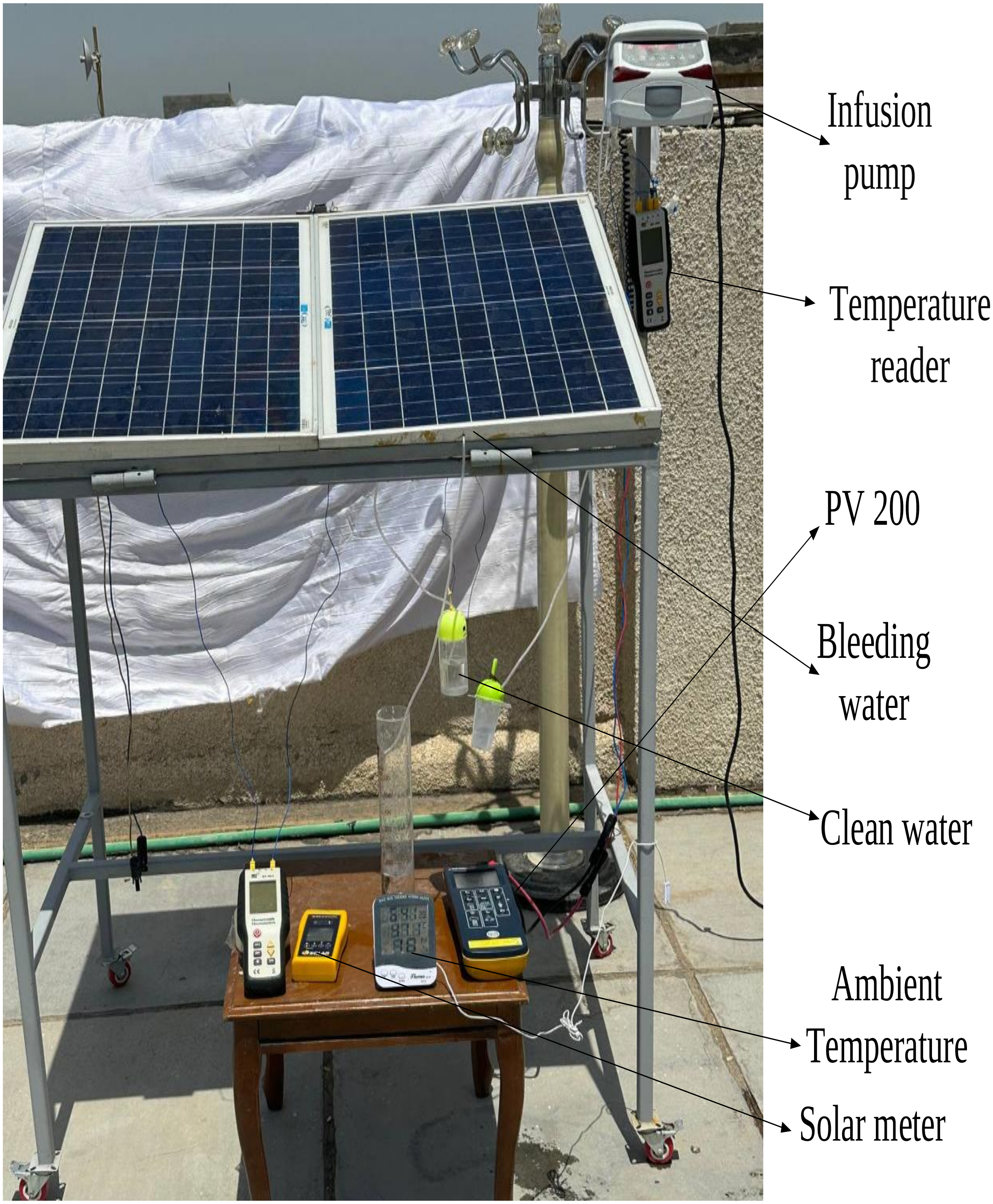

Figure (4.18): A photograph of the outdoor test rig.

Table (4.5): Specifications of solar panels.

Model	**FRS-50W**
Rated maximum power (p_{max})	50W
Current at Pmax (I_{mp})	2.80A
The voltage at Pmax(V_{mp})	18 V
Short Circuit Current (I_{sc})	3.17 A
Open Circuit Voltage (V_{oc})	22 V
Nominal Operation Cell Temp	45 ^{0}C ± 2 ^{0}C
Temperature Coefficient (p_{max})	0.45 %/°C
Temperature Coefficient (V_{oc})	0.34 **%**/ °C
Temperature Coefficient (I_{sc})	0.05 %/°C
Application Class	Class A
Weight	3.5 kg
Dimensions	670*540*46 (mm)
Total Number Of Cell	36 (4*9)

** Standard test conditions: Irradiance 1000 W/m^2, cell temperature 25°C, AM 1.5*

*** Normal operating cell temperature: Irradiance 800 W/m^2, Ambient temperature 20°C, AM 1.5 wind speed 1 m/s.*

4.4 MEASUREMENT AND INSTRUMENTATIONS

The temperature of different locations of the PV panels, the outdoor temperature, solar radiation, and the PV panel performance are measured using different instrumentations. A brief preview of the instrumentations is introduced bellows.

4.4.1 Temperature measurement

Thirteen thermocouples type-K (Nickel 10%, Chromium versus 5% Aluminum, Silicon) in the range of -200 to 1250°C were used to measure the temperature distributions in the Photovoltaic-membrane distillation during the period of the experiment. A digital temperature reader of type HT 9815 type-K, shown in Figure (4.19), was used to read the temperature value. These thermocouples have been calibrated, and the calibration details are mentioned in Appendix B.

The thermocouples have been installed at different locations; the measuring point locations are illustrated in Fig. (4-20). Three thermocouples are used in each rig to measure the solar cell surface back temperature (T1), the evaporation layer temperature (T2), and the condensation layer temperature(T3).

4.4.2 Solar PV Performance

The performance of the solar PV is measured using PV 200 device. PV 200 can measure the field performance of the PV panel and compare the result with that of the standard panel operation. The PV 200 can perform the following measurements; AC / DC voltage using the 4mm terminals, open circuit module, string, or array voltage, short circuit module, string, or array current, module, string, or array insulation resistance at 250V, 500V, and 1000VDC, probe to probe insulation resistance at 250V, 500V, and 1000VDC, AC or DC Operating current (with AC/DC clamp), and String I-V curve test. The results can be displayed on the mobile. Figure 4.21 shows the PV 200.

4.4.3 Solar Irradiance Measurement

The solar power meter is a tool to measure the intensity of solar energy. Solar power meter type SOLAR SURVEY 200R. The measuring range is 0-1500 W/m^2; the resolution is 1 W/m^2; the temperature range is -30 to 125°C; the resolution is 1°C; Compass Bearing Range is 0° to 360°; the resolution is 1° and Inclinometer Range 0° to 90. The Dimensions of the device are 14.8 x 8.0 x 3.3cm. Figure (4.22) shows the Solar irradiance measure.

Figure (4.19): Digital temperature reader.

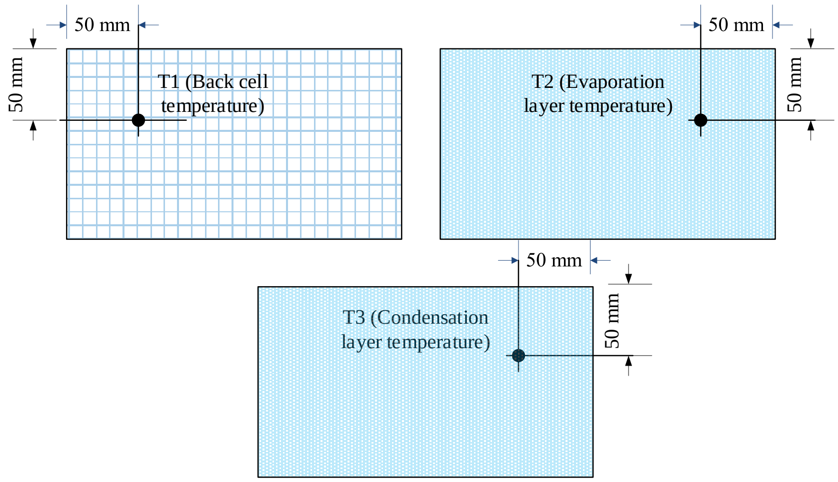

Figure (4-20): The locations of thermocouples.

PV200 PV200 Complete Kit

Figure (4.21): PV 200 with accessories.

Figure (4.22) The Solar irradiance measure.

4.5 EXPERIMENT KEY VARIABLES AND TEST PROCEDURE

4.5.1 Experimental Key Variables

1. The mass flow rate of water: Two methods cool the PMD solar cell; the first is to supply an amount of water in the range of 1.243 to 1.796 $kg/h.m^2$[30], a part of the water is evaporated, and the rest is bleeding (outdoor experimental). The second is called the dead state method [31], in which the water supply to the cell is totally evaporated. The mass flow rate of water in the dead stat method ranges from 0.43 to 1.298 $kg/h.m^2$ (indoor experimental).
2. The Solar intensity: The solar radiation in Baghdad depends on the relevant date. However, the solar radiation does not exceed 950 Watts per square meter, so the simulated solar radiation in the current work ranges from 300 to 600 W/m^2.
3. The remembrance pore sizes: Four membrane pore sizes are studied, namely; 0.45, 1, 3, and 5μm.

4.5.2 Data Collected

The data collected are:

1. Cell surface temperature (T1).
2. Evaporation layer temperature (T2).
3. Condensation layer temperature (T3).
4. The mass flow rate of produced fresh water.
5. Solar intensity.

4.5.3 Test Procedures

As mentioned before, indoor and outdoor tests are performed.

1. Indoor tests: the data are collected manually every 15 min. and extended to 1 hour until the steady state temperature of the cell is reached.
2. Outdoor test: the data are collected manually every 30 min, from 7 am to 6 pm.

4.6 UNCERTAINTY PROPAGATION. (Error analysis)

The obtained uncertainty of the variables is displayed in Table(4.6). The uncertainty propagation is analyzed using Engineering Equation Solver (EES) software for the investigated parameters. The results are shown in Appendix C. Result from EES the uncertainty of the efficiency of solar panels (0.005053), of the pressure of condensation layers (1.306e-9), and for evaporation layers(1.45e-9).

Table (4.6): Absolute Accuracy.

No	Measuring devices	Accuracy error
1	Temperature Sensor	± 1° C
2	Solar radiation	0.05 W/m^2
3	Current	0.01 A
4	Voltage	0.01 V

4.7 ELECTRICITY EFFICIENCY

The performance of the PV panels is used to estimate the system's electrical efficiency. Electrical efficiency is defined as the ratio of the actual electrical output to the solar irradiation that is incident on the area of the PV module.

$$W = I * V \tag{4.1}$$

$$Q_{abs} = G.A.\alpha \tag{4.2}$$

$$\eta_{solar\ panel} = \frac{W}{Q_{abs}} \tag{4.3}$$

Where**:**

$\eta_{solar\ panel}$ Is the electricity efficiency

Chapter Five

Results and Discussion

Chapter Five

Results and Discussion

5.1 INTRODUCTION

This chapter reviews the current study's three methods: numerical simulation and indoor and outdoor tests. After reviewing the three method results, the system performance is determined.

It is worth noting that all the cases reviewed have two factors that affect the performance of the cell, the first is the cell temperature, and the second is the water productivity. Although the two factors are essential, cell temperature is considered to be the critical factor.

The weather conditions of Baghdad (33.3152° N, 44.3661° E), in which the experiments were conducted, are shown in Figure 5.1.

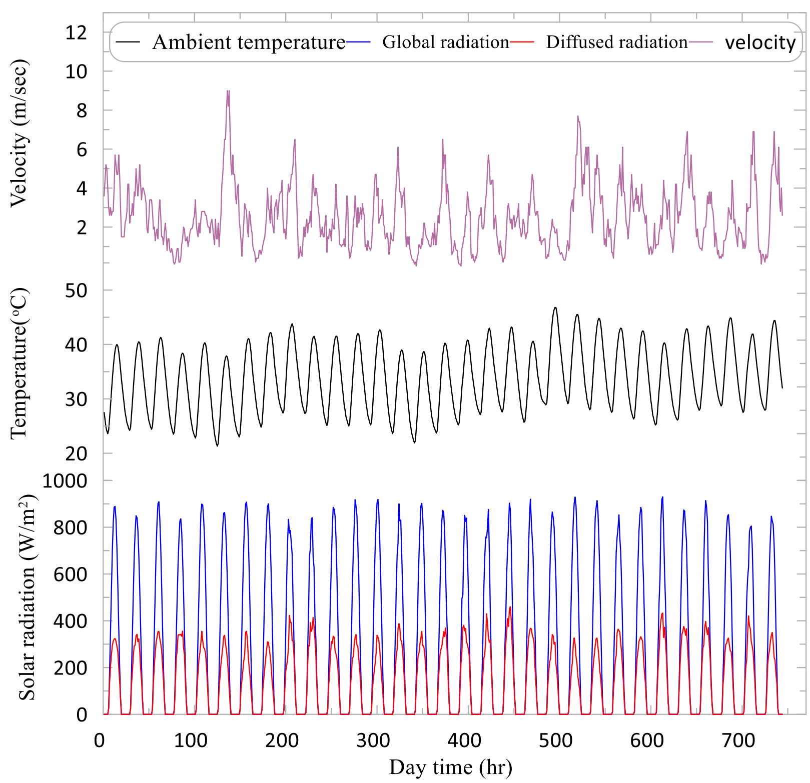

Figure (5.1): Baghdad Weather conditions.

5.2 NUMERICAL SIMULATION RESULTS

The effect of the membrane thickness on the system performance was studied. In the current study, the thickness of the membrane ranges from 100 to 1000 μm was investigated in detail. Figure 5.2 shows the effect of membrane thickness on the temperature polarization calculated by Equation 3.8 for the condensation and evaporation layer. The mass flow rate of the supply water is selected to be 0.856 kg/m^2.h depending on the work of Wang *et al.*[34]. From this figure, it can be seen that as the membrane thickness increases, the temperature polarization also increases. It is worth noting that temperature polarization tends to reduce the difference in vapor pressure across the membrane, leading to a decrease in the vapor flux across the membrane.

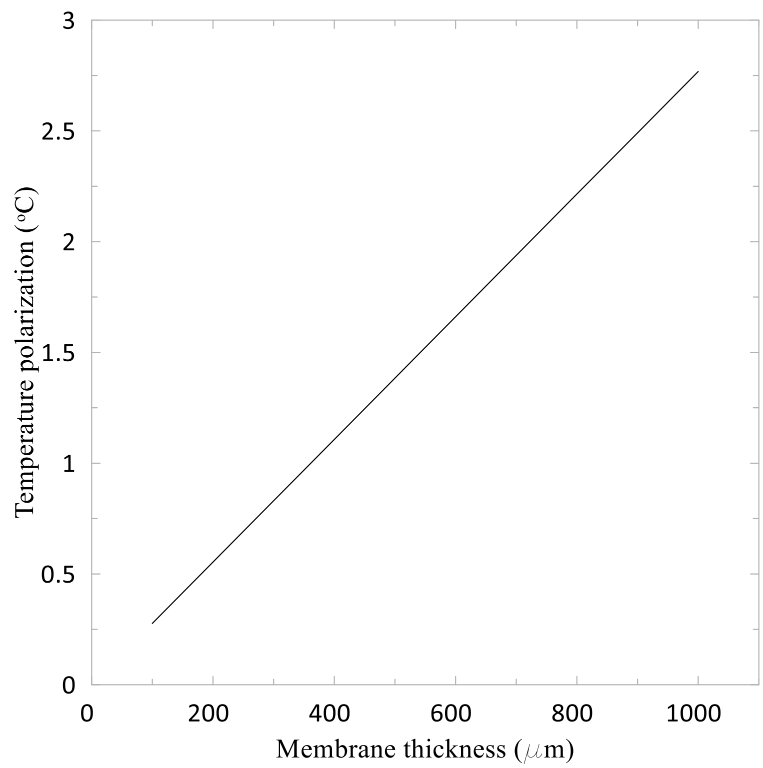

Figure (5.2): The effect of membrane thickness on the temperature polarization (°c).

Figure 5.3 shows the relation between the membrane thickness and the membrane coefficient, representing the mean vapor permeability through the membrane. It can be seen from the Figure that the thin membrane has a higher membrane coefficient. The higher the membrane coefficient, the more vapor passes through the membrane, as shown in Figure 5.3. Since the membrane thickness of 100 μm gives the minimum, temperature gradient, and maximum membrane coefficient, so, it is recommended to keep the membrane thickness at 100 μm. Equation 3.13 calculates the membrane coefficient.

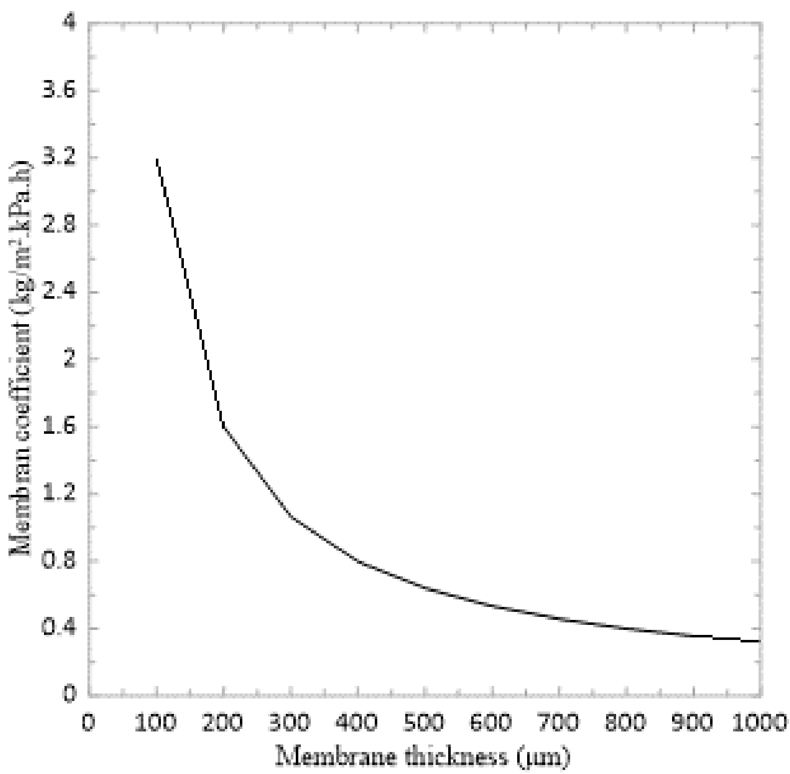

Figure (5.3): The relation between the membrane thickness and membrane coefficient.

The distance between the evaporation and condensation layers is called the space thickness. Space thickness is the critical factor for generating the temperature difference between the evaporation and condensation layers, which generates the pressure difference that drives the water vapor to move from the evaporator to the condenser layer. This distance can be done in two ways: by placing hydrophobic membranes between them or by placing a mesh. The two methods are adopted to ensure space between the condenser and the evaporator layers.Figures 5.4 and 5.5 show the effect of space thickness between the evaporation and condensing layers on the evaporation and condensation temperature. Figure 5.4 shows that the space thickness affects the evaporation temperature more than the condensing temperature. However, the 2.5 and 3 mm space thickness shows a higher evaporation temperature; the same trends in the first half of the day are shown for the two air gap thicknesses mentioned. So, from an economic viewpoint, the air gap thickness of 2.5 mm is adopted in the current work.

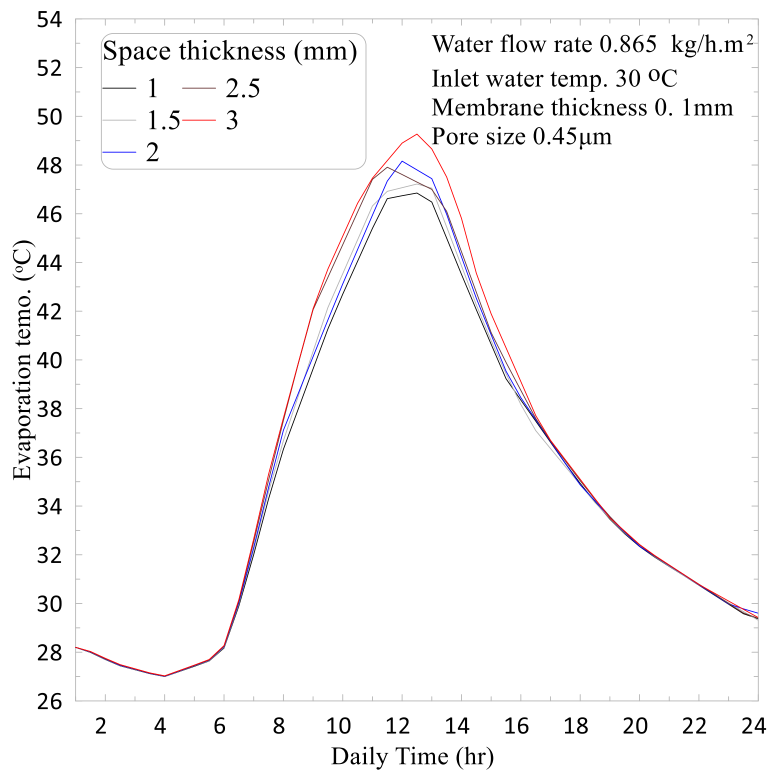

Figure (5.4): The effect of space thickness on the evaporation temperature

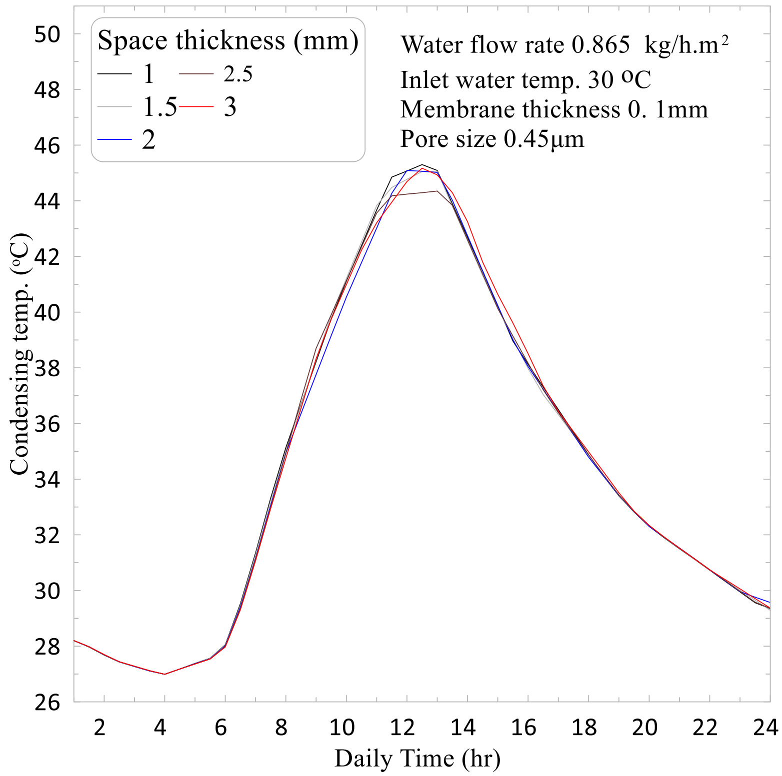

Figure (5.5): The effect of space thickness on the condensing temperature

Figure 5.6 shows the difference between the evaporation and condensing temperature for 2.5 mm air gap thickness. The Figure shows that at night time, there is no temperature difference between the evaporation and condensing temperatures. As the sun shines, the difference between the two temperatures starts and reaches the maximum at solar noon.

Figure 5.7 shows the effect of PMD on the cell surface temperature when the air gap thickness is 2.5 mm. It can be seen from the Figure that the maximum difference between the cooled and uncooled cell temperatures is about 7^{o}C at solar noon. The reduction in cell temperature is due to the water absorption of stored heat in the cell by the water supply to the cell.

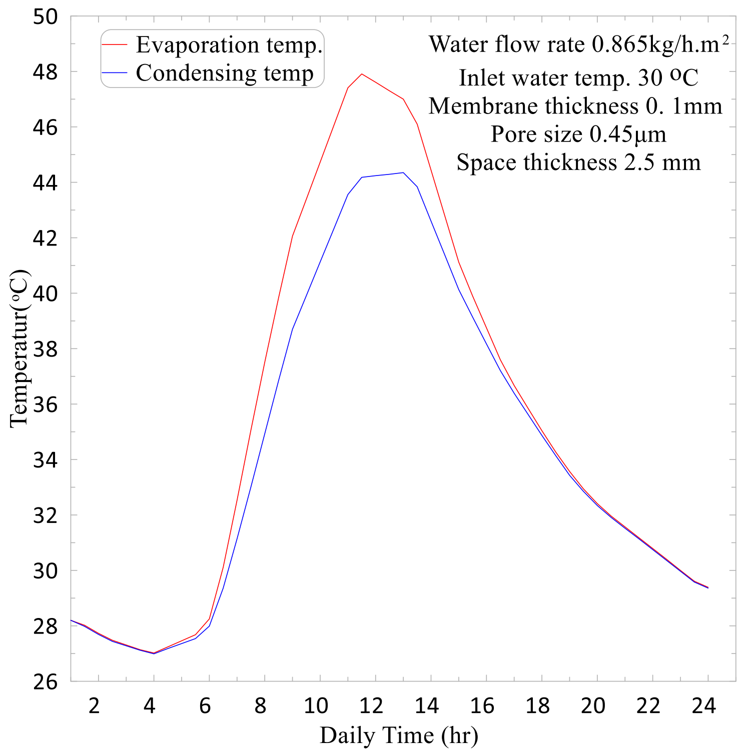

Figure (5.6): The difference between evaporation and condensing temperature at 2.5 mm space thickness

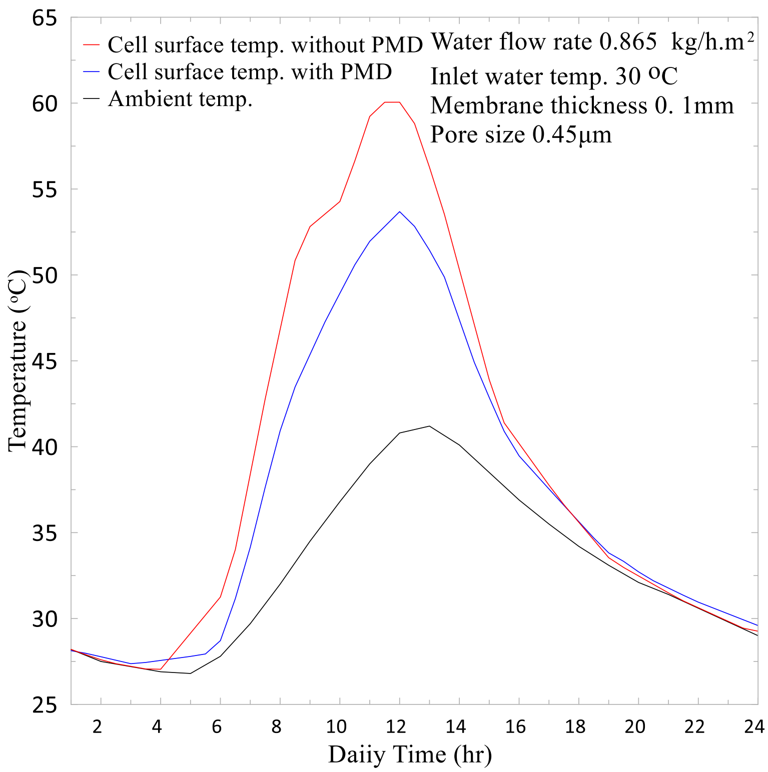

Figure (5.7): The effect of PMD on the cell surface temperature

To study the effect of fin height on the cell surface temperature and water productivity heat sink of 1 mm base thickness with five fins is attached to the last aluminum layer. The effect of fin height on the cell temperature is shown in Figure 5.8. It can be seen from the figure that the temperature of the cell decreases with the increase in the height of the fin due to the ability of the long fin. To dissipate heat more efficiently than the short fin. On the other hand, Figure 5.9 shows that increasing the height of the fin reduces water productivity due to the decrease in cell temperature. So a trade-off should be made between the two cases. A fin height of 2 cm is chosen to achieve a lower cell temperature and more water productivity.

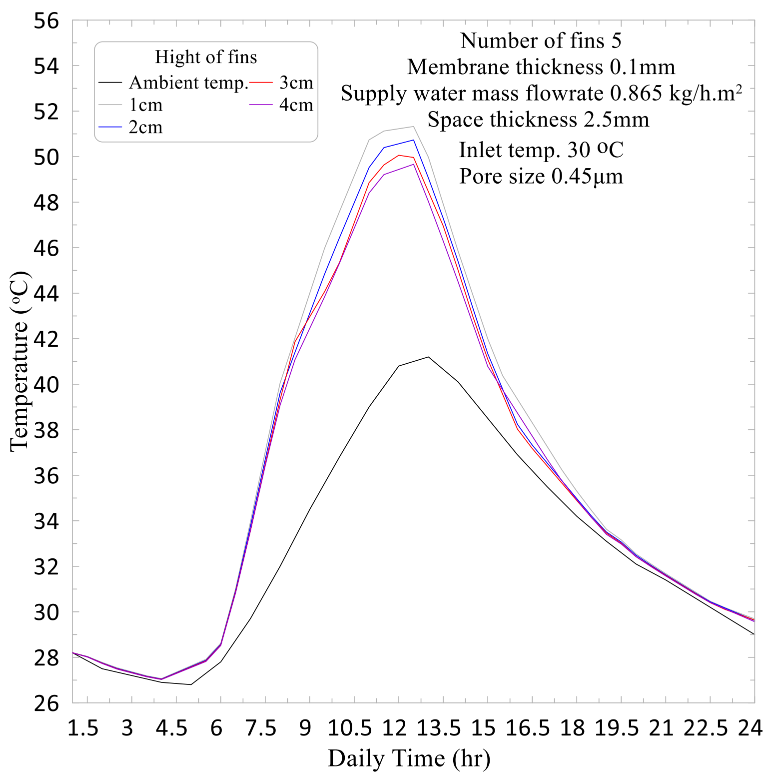

Figure (5.8): The effect of fin height on the cell temperature

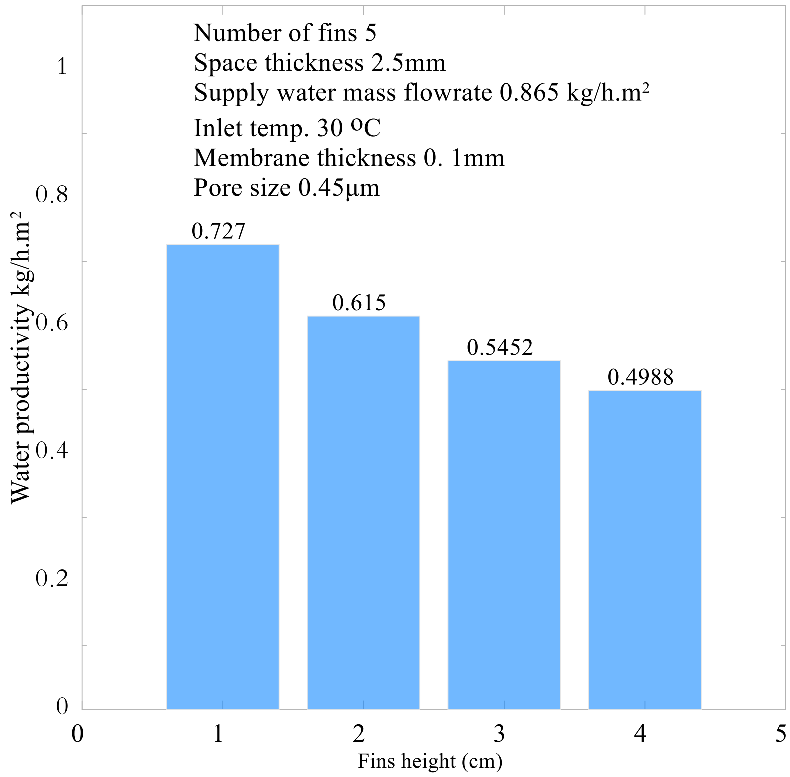

Figure (5.9): The effect of fin height on water productivity

The number of fins affects both the cell surface temperature and water productivity; increasing the number of fins reduces the cell temperature, as shown in Figure 5.10; on the other hand, the water productivity reduces as the number of fins increases, as shown in Figure 5.11. So, keeping the number of fins at five is recommended, from the economic point of view and the water productivity.

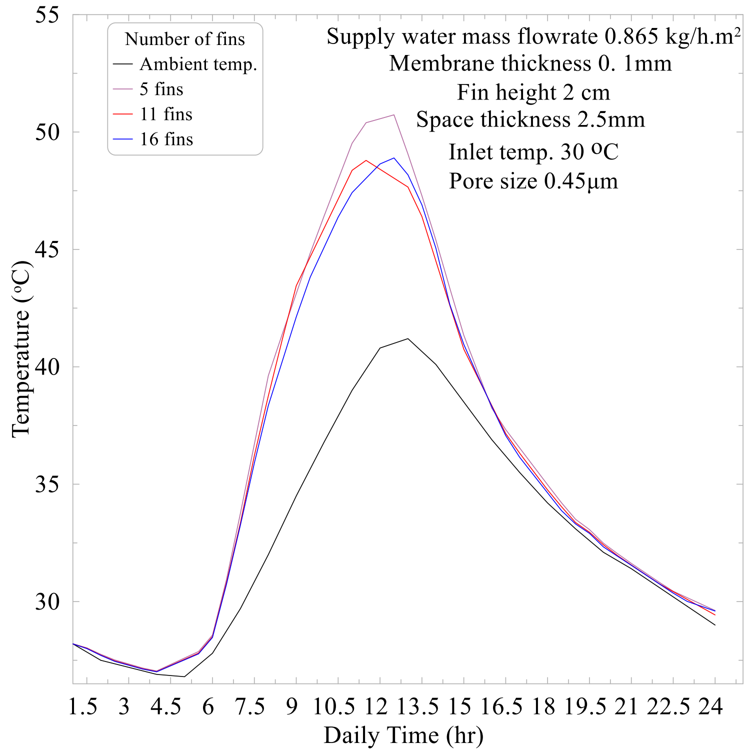

Figure (5.10): The effect of the number of fins on the cell surface temperature, fins height 2 cm**.**

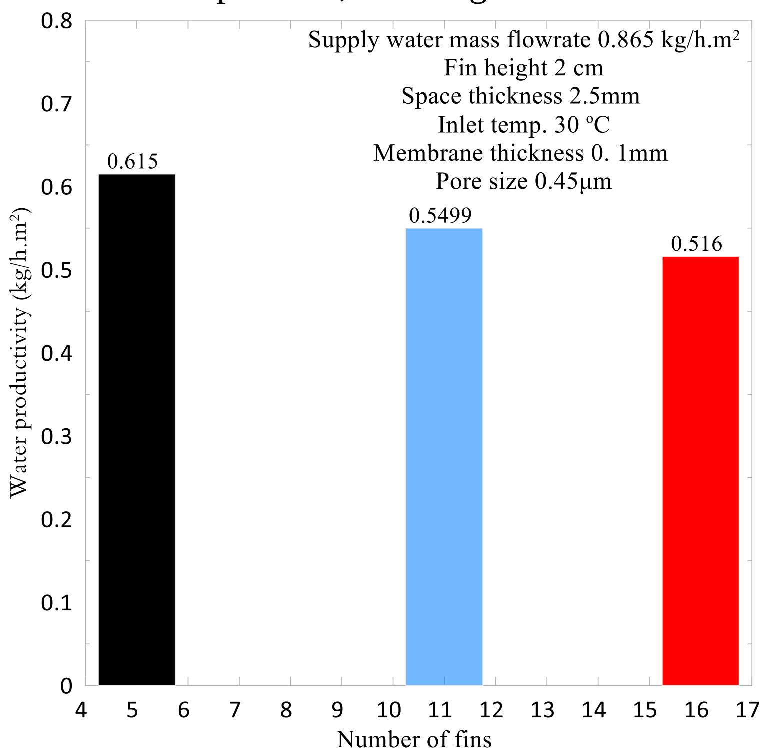

Figure (5.11): The effect of the number of fins on the water productivity, fins height 2 cm.

The inlet temperature of supply water significantly affects cell surface temperature and water productivity, as shown in Figures 5.12 and 5.13. Figure 5.12 shows that the cell surface temperature decreases as the inlet water temperature decreases. On the contrary, Figure 5.13 shows that low water temperature reduces water productivity. In any case, the water temperature factor is difficult to control as the water temperature relates to the surrounding weather conditions.

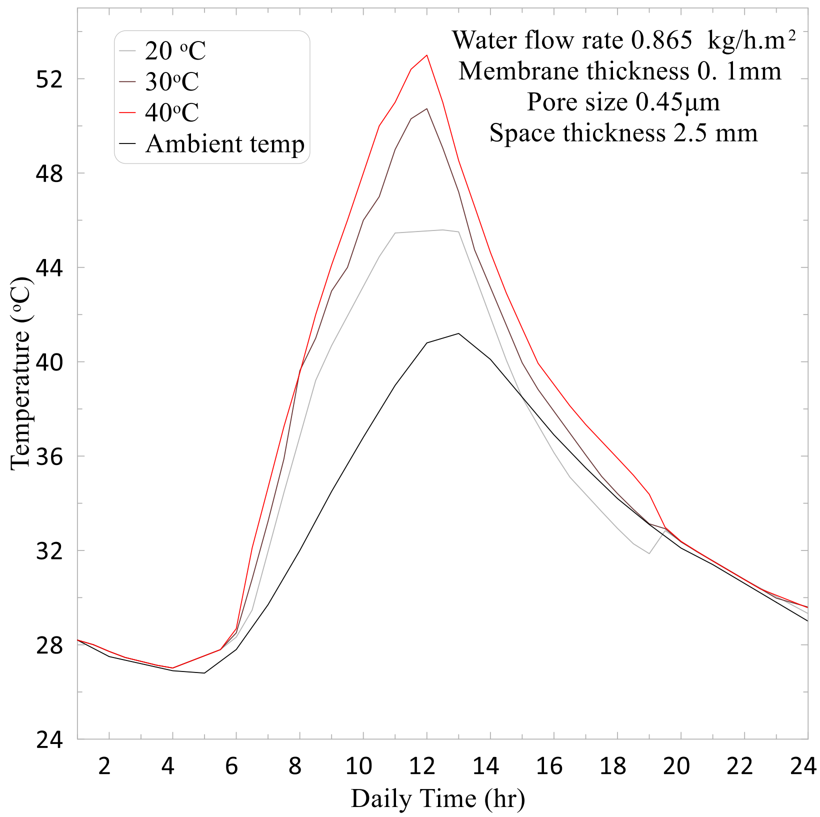

Figure (5.12): The effect of inlet water temperature on the cell surface temperature.

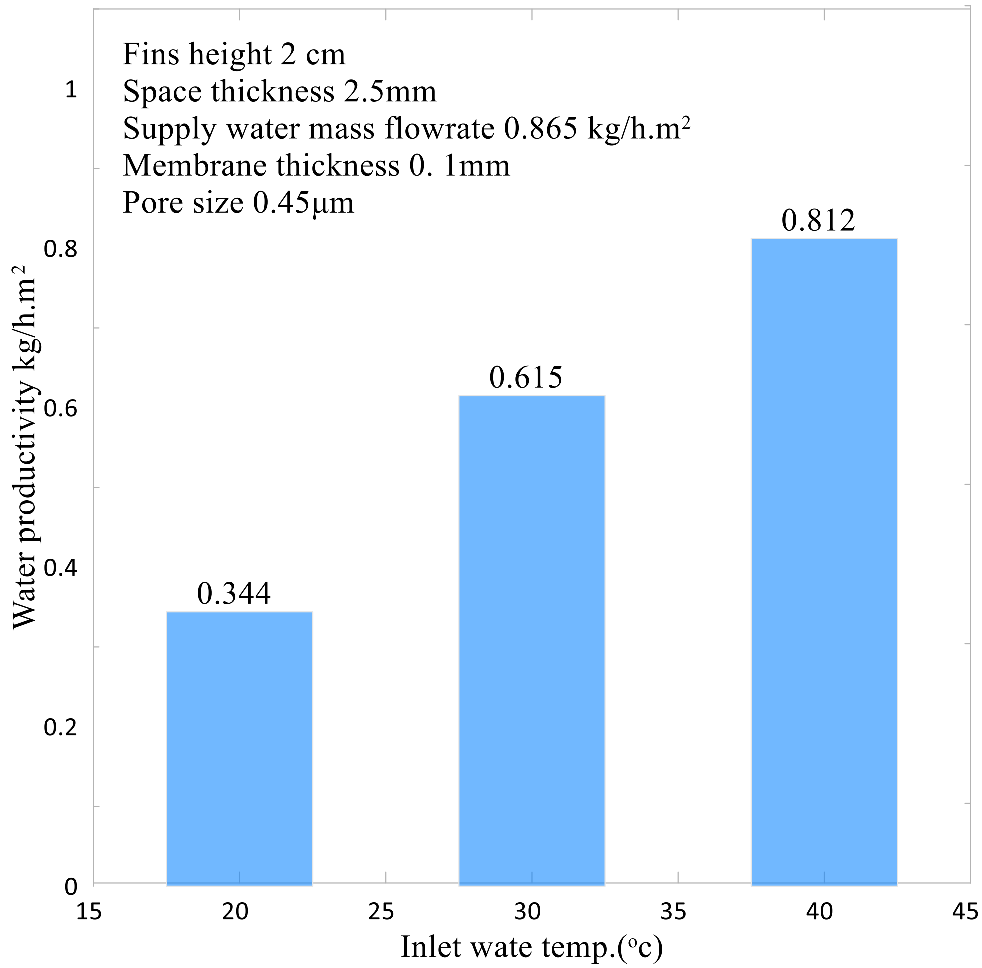

Figure (5.13): The effect of inlet water temperature on water productivity.

The current work is validated for two cases; the first with the results of the membrane coefficient of the present work with Alied[30], as shown in Figure 5.14; the deviation between the two works is about 8%.

Unfortunately, to our knowledge, in the second validation, no work analyzes the effect of adding PMD to the solar panel. So the current work is validated by Alqurashi, Altuwirqi, and Ganash, 2020 [68], who studied the performance of the uncooled solar panel in Riyadh using COMSOL software. Figure 5.15a shows the temperature distribution of the solar panel in Saudia Arabia, Riyadh, while Figure 5.15 b shows the temperature distribution for the same solar panel under Riyadh weather data (the wind speed is 10.28 m/s, the ambient temperature is 39℃ and the solar radiation is 750 w/m^2.). The figure shows a good agreement between the current work and the work of Alqurashi, Altuwirqi, and Ganash, 2020.

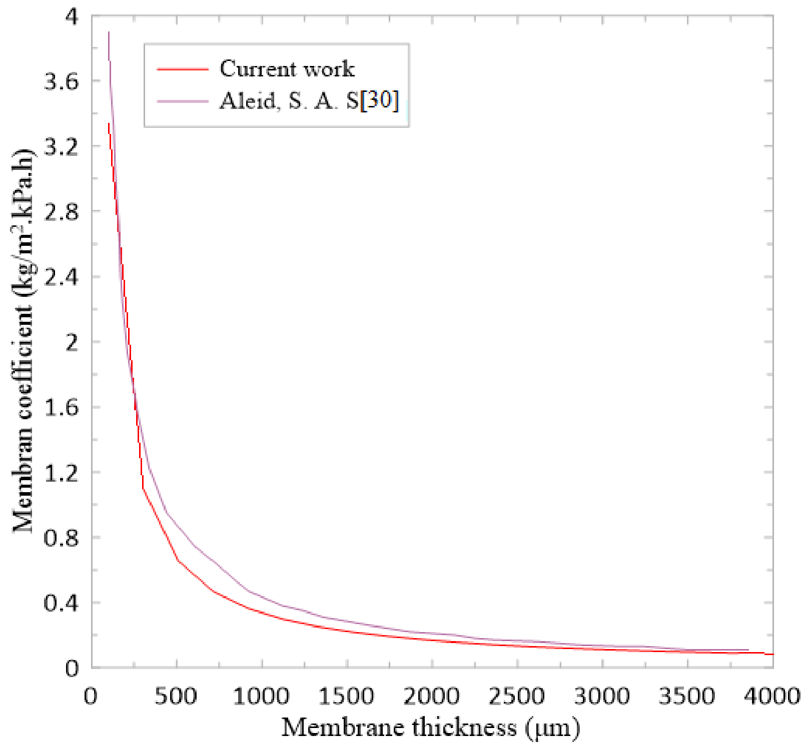

Figure (5.14): Validation of membrane coefficient.

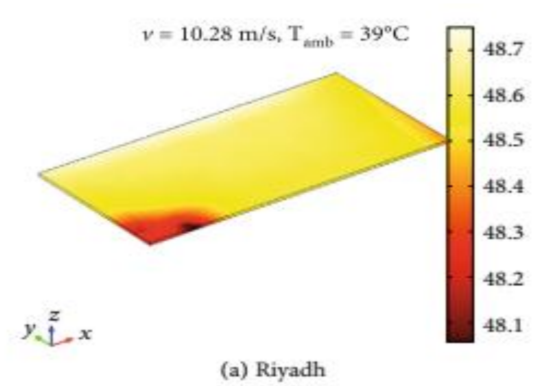

Figure 5.15a Temperature distribution of uncooled solar panel [68].

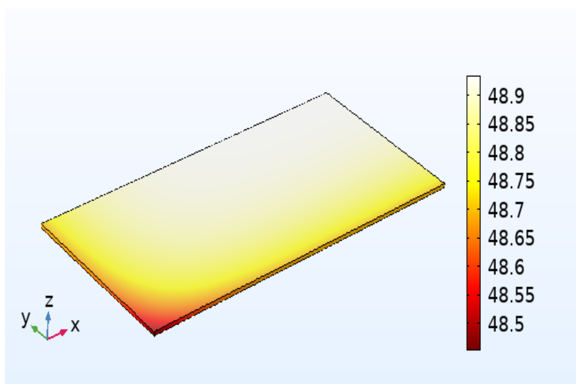

Figure 5.15b The current work.

Figure (5.15): Validation of uncooled solar panel.

5.3 INDOOR TEST RESULTS

The data obtained from the theoretical simulation shown in Table 5.1 are used to build the indoor test rig; thus, the following dimensions are used to construct the indoor test rigs.

Table (5.1): Theoretical simulation results used to build the indoor test rig

Membrane thick.	100 μm	The flow rate of supply water	0.865 $kg/m^2.h$
Space thickness	2.5 mm	Inlet water temp.	30^oC

The variable studied in the indoor test is the solar intensity in the range of 300 to 600 W/m^2 in the 100 W/m^2 steps. First study the effect of the mass flow rate of supply water on the cell temperature and water productivity was studied. The mass flow rate of supply was 0.432, 0.865, and 1.3 $kg/m^2.h$ studied, as shown in Figures 5.16 and 5.17. It can be seen from Figure 5.16 that as the solar intensity increases, the cell temperature increases also. The maximum cell temperature was at the minimum mass flow rate of supply and the maximum solar intensity. Increasing the mass flow rate of supply water reduces the cell temperature, so the minimum cell temperature was at the mass flow rate of supply water of 1.3 $kg/m^2.h$.

On the other hand, at lower solar intensity, the productivity of fresh water was produced as the mass flow rate of supply water increased, as shown in Figure 5.17. It can be seen from the Figure that the productivity was about 0.172 $kg/m^2.h$ at 300 and 400 W/m^2 of solar intensity and mass flow rate of supply water 1.3 kg/m^2. The mass flow rate of 0.865 shows a reasonable trend since this mass flow rate of supply water can improve the cell surface temperature and water productivity at a wide range of solar intensity.

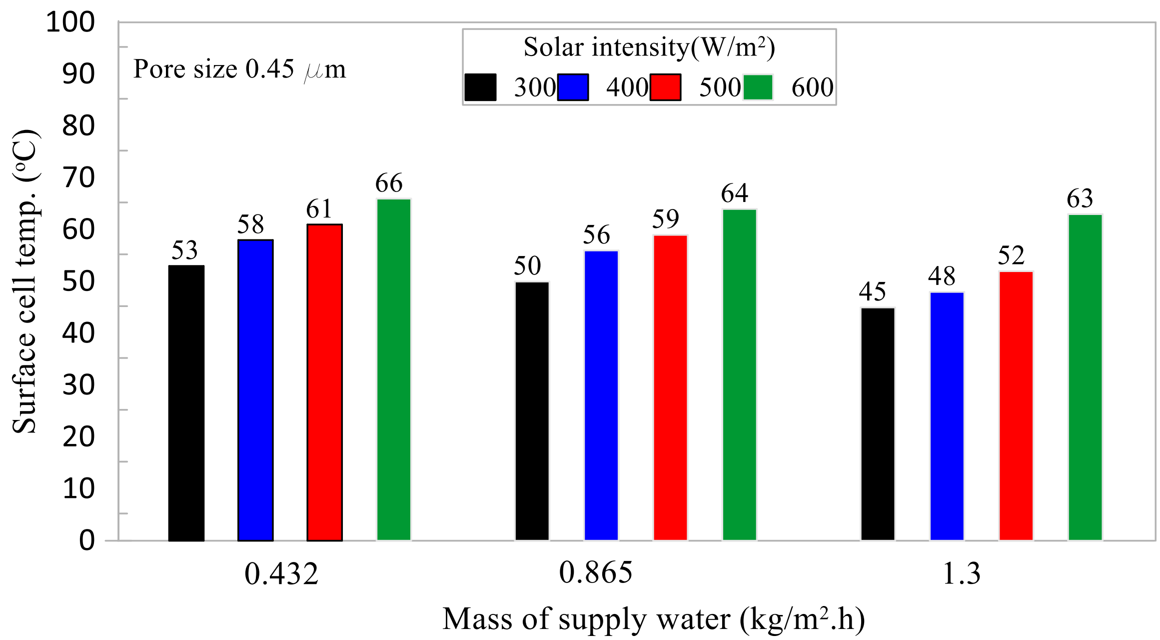

Figure (5.16): The effect of the mass flow rate of supply water and solar intensity on the cell surface temperature.

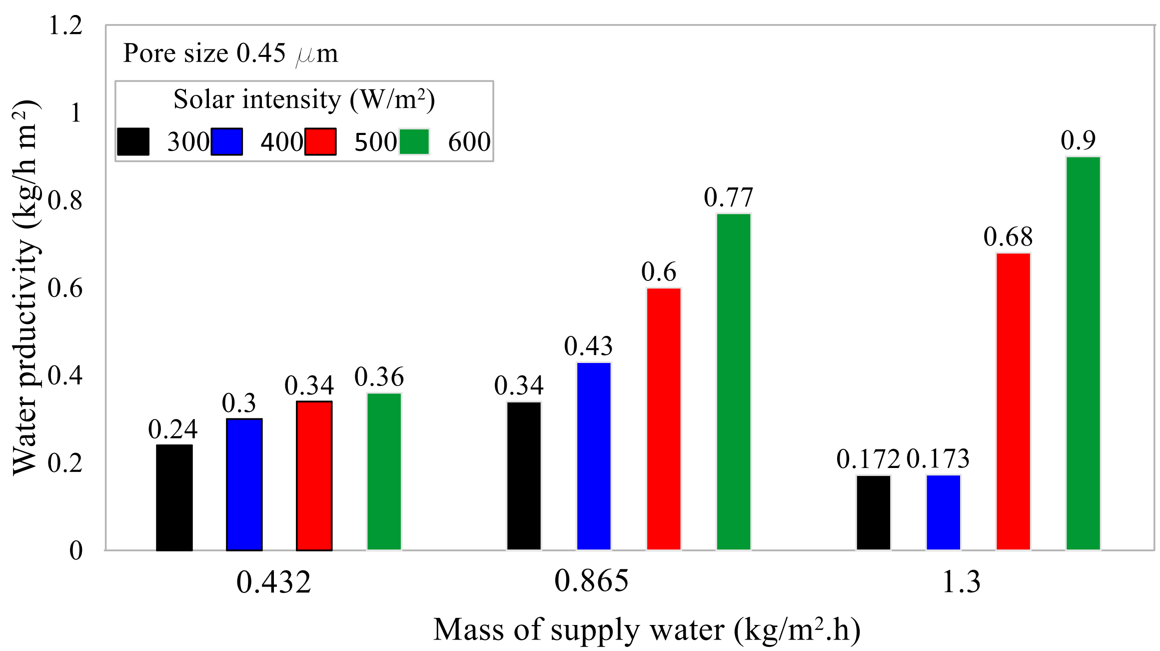

Figure (5.17): The effect of the mass flow rate of supply water and solar intensity on water productivity.

Figure 5.18 shows the effect of membrane pore size on the evaporation layer temperature when the solar intensity of 300 W/m^2 and the supply water flow rate of 0.865 kg/m^2.h. It can be seen from the figure that the minimum pore size is the minimum evaporation temperature. From Figure 4.9, it can be seen that a small pore size means a higher porosity. Decreasing the pore size of the membrane leads to the ease of passage of water vapor through the membrane. Thus the vapor pressure decreases, which necessarily leads to a decrease in the evaporation temperature. The reduction in evaporation temperature leads to reduce the condensing temperature, as shown in Figure 5.19; the figure shows that the maximum condensing temperature is for the pore size of 5 μm. The increase in evaporation temperature reflects negatively on the cell surface temperature, as shown in Figure 5.20. It can be seen from the figure that the minimum cell temperature is 50 ^{o}C for a pore size of 0.45 μm, which is less by about 10 ^{o}C than that of the uncooled cell.

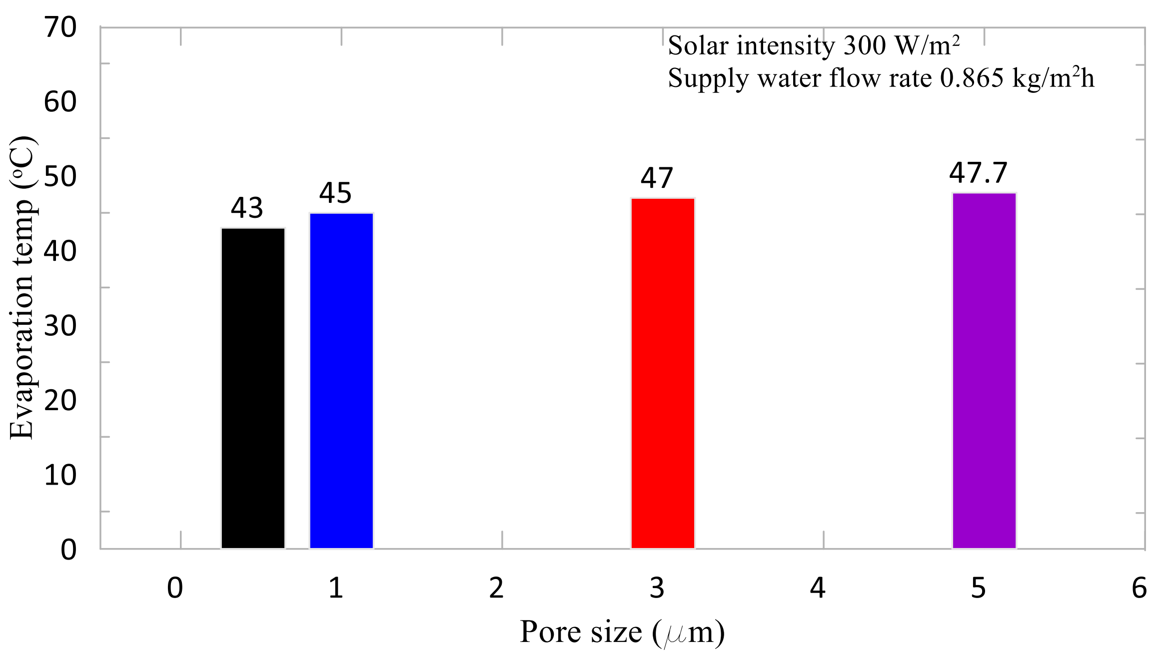

Figure (5.18): Effect of pore size on the evaporation temperature.

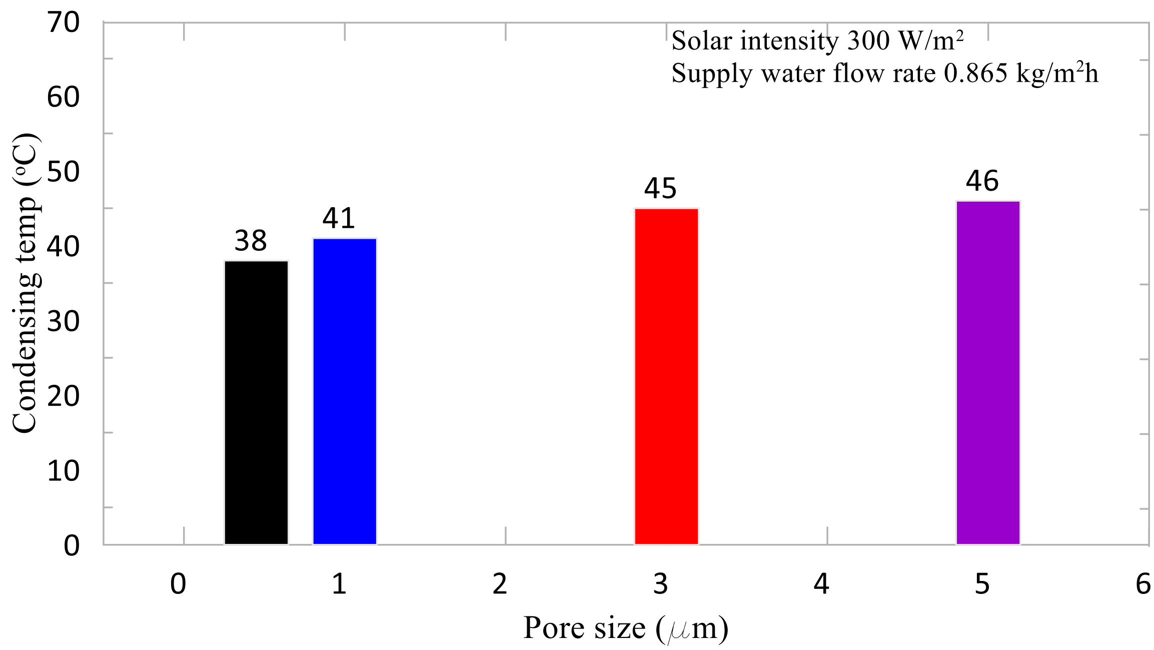

Figure (5.19): Effect of pore size on the condensing temperature.

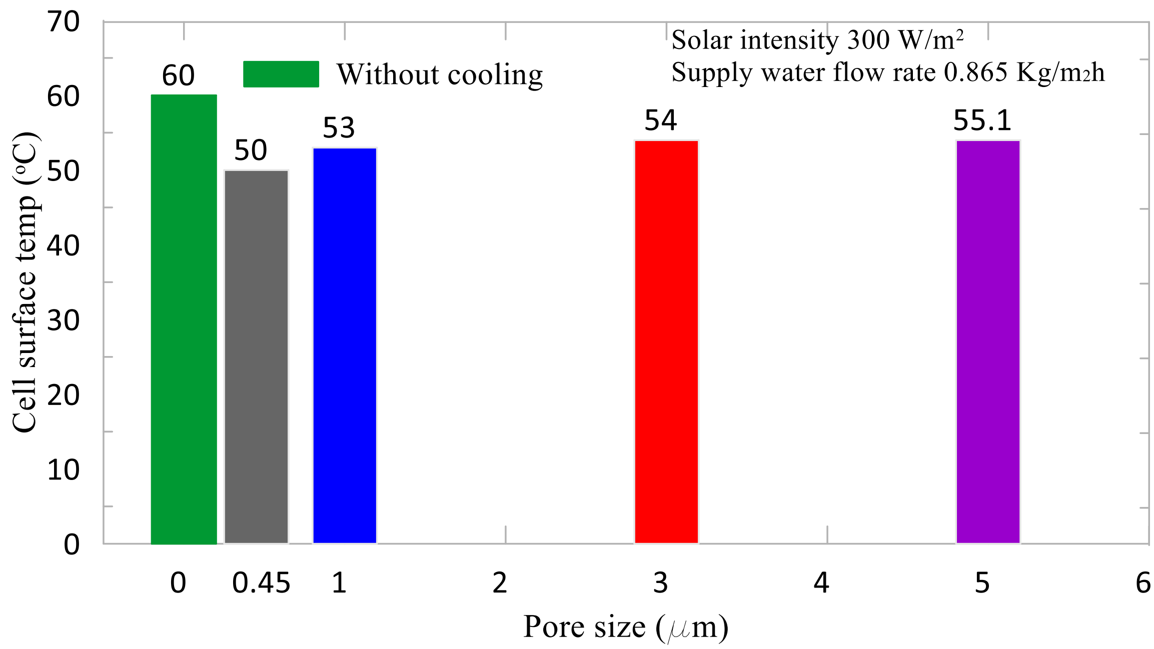

Figure (5.20): Effect of pore size on the cell surface temperature

The effect of pore size on water production is shown in Figure 5.21. Although the pore size had a weak effect on the cell temperature when the solar intensity is 300 W/m^2, but its effect on water production was highly effective, as the figure shows that the water production for 0.45 µm membrane pore size is about 18 times more than that of diameter 5 µm. This was because the porosity of the 5 µm membrane does not allow water vapor to pass easily.

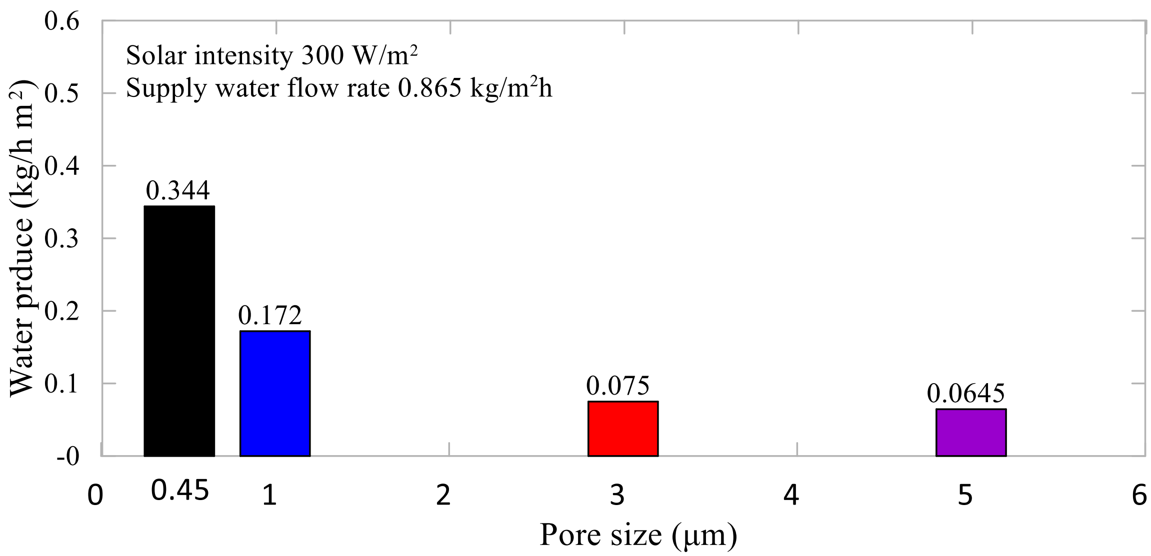

Figure (5.21): Effect of pore size on the water productivity

Figure 5.22 shows the variation of evaporation, condensation, and cell temperatures with time when the solar intensity was 300 W/m^2, pore size was 0.45 µm, and the supply water flow rate was 0.865 kg/m^2.h. When solar radiation incident on the cell surface, the cell temperature increases due to the heat gain by the cell. The transfer of heat gain from the cell to the evaporator layer leads to the evaporation of the water at a temperature lower than the cell temperature. The vapor permeates through the membrane and condenses at a temperature lower than the evaporator temperature.

From the results, it can be concluded that the best pore size for the membrane, which helps in cooling the cell and increases water productivity, is 0.45 μm.

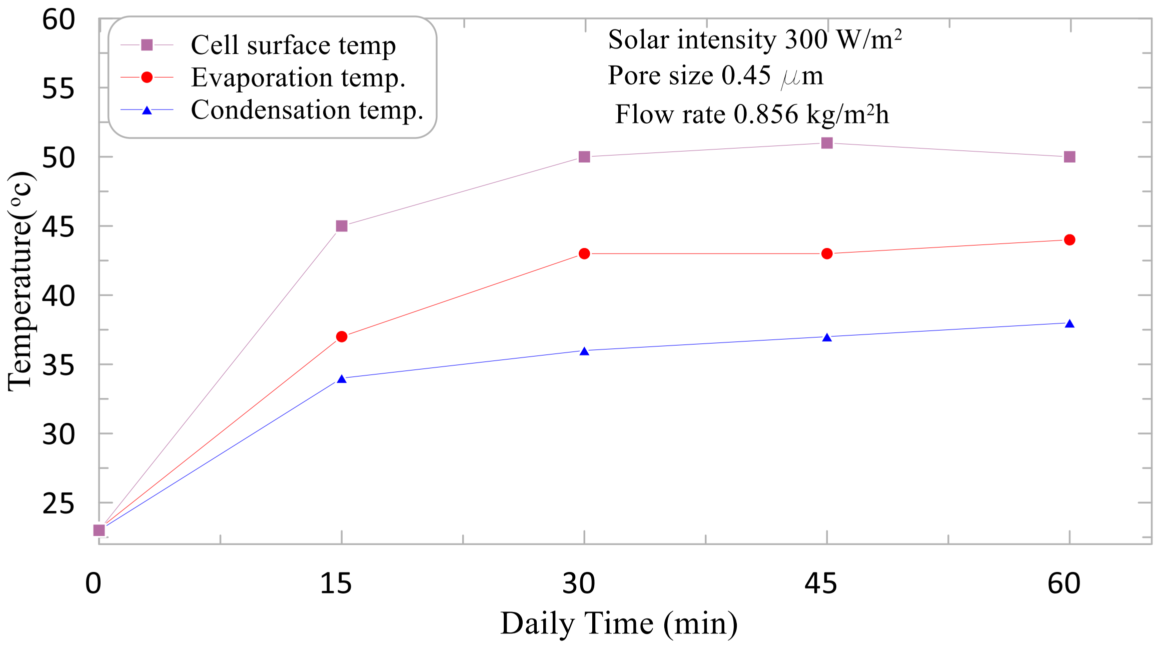

Figure (5.22): The variation of evaporation, condensation, and cell temperatures with time when the solar intensity is 300 W/m^2, pore size 0.45 μ*m*, and supply water flow rate is 0.865 kg/m^2.h

The effect of solar intensity on evaporation, condensation, cell temperatures, and water productivity are shown in Figures 5.23 to 5.26. Figure 5.23 shows the effect of solar intensity on the evaporation temperature when the pore size is 0.45 μm. It can be seen from the figure that the higher solar intensity gives a higher temperature for evaporation, condensing, and cell surface temperature, as shown in the figure. The increase in solar intensity increases water productivity significantly. As shown in Figure 5.26, it can be seen the double of solar radiation leads to an increase in the water productivity of solar intensity by 225%.

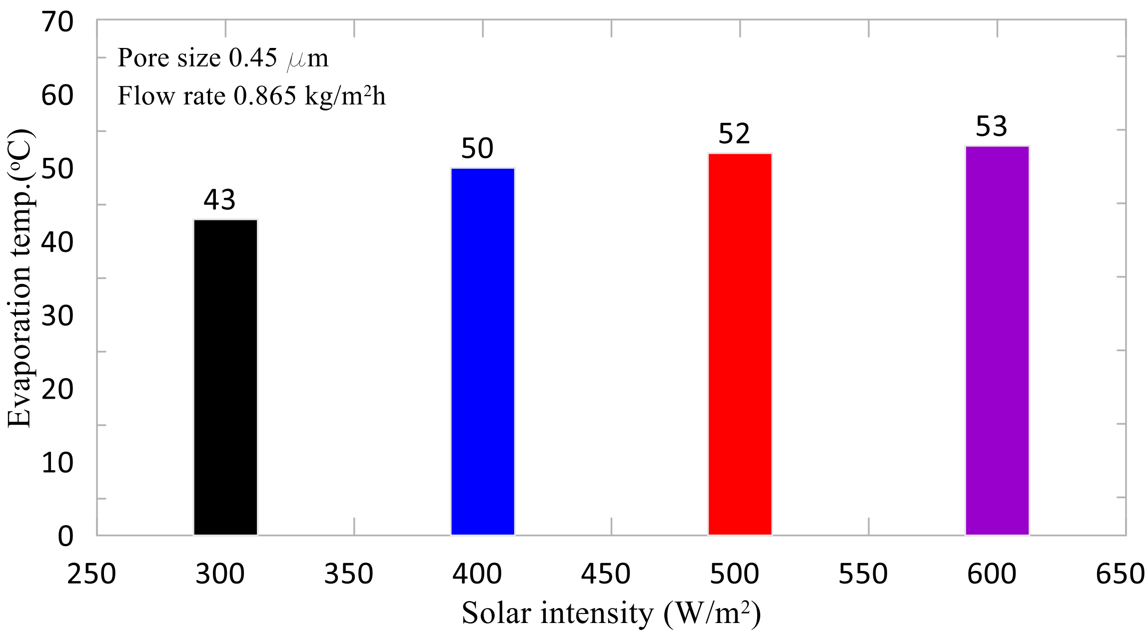

Figure (5.23): The effect of solar intensity on the evaporation temperature for pore size 0.45 μm and supply water flow rate 0.865 kg/m^2.h.

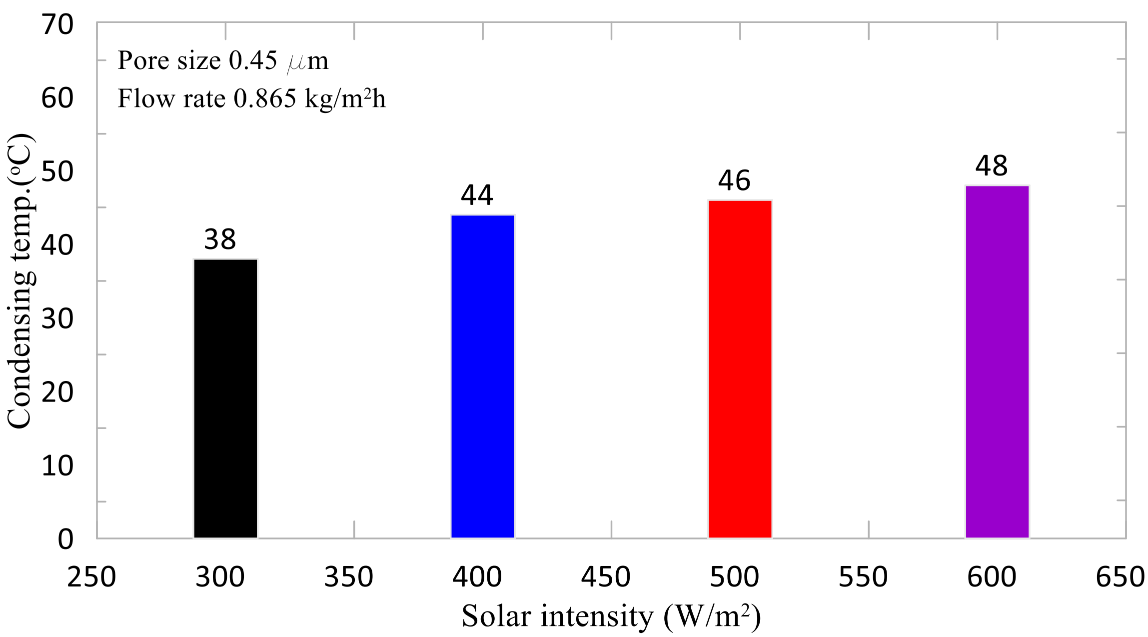

Figure (5.24): The effect of solar intensity on the condensing temperature for pore size 0.45 μm and supply water flow rate 0.865 kg/m^2.h.

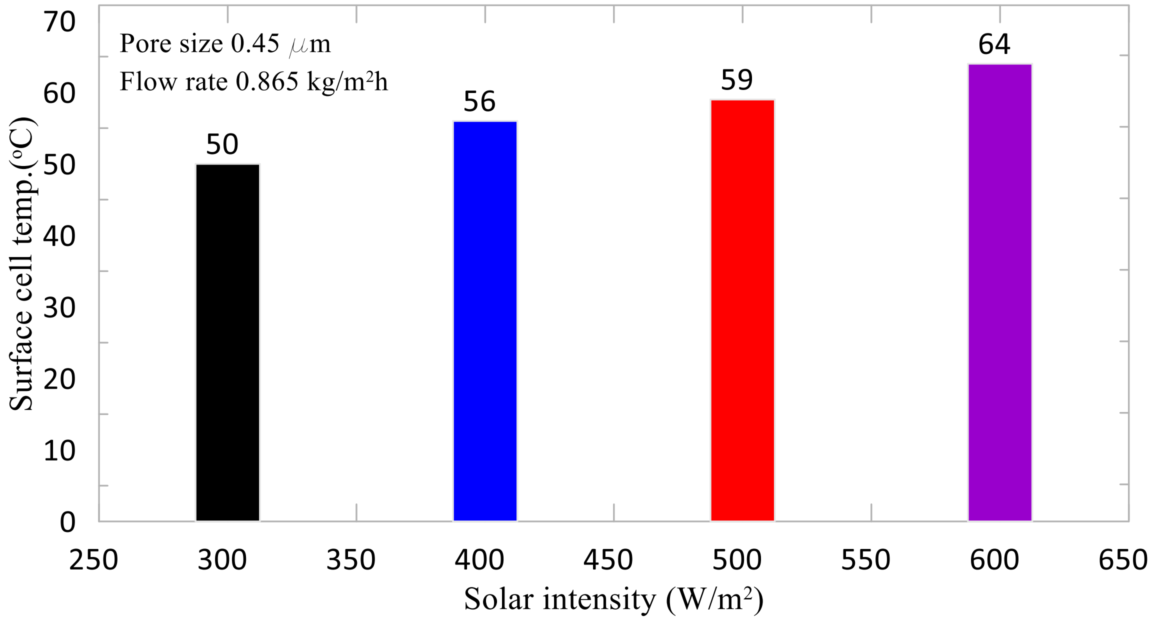

Figure (5.25): The effect of solar intensity on the surface cell temperature for pore size 0.45 μm and supply water flow rate 0.865 kg/m^2.h.

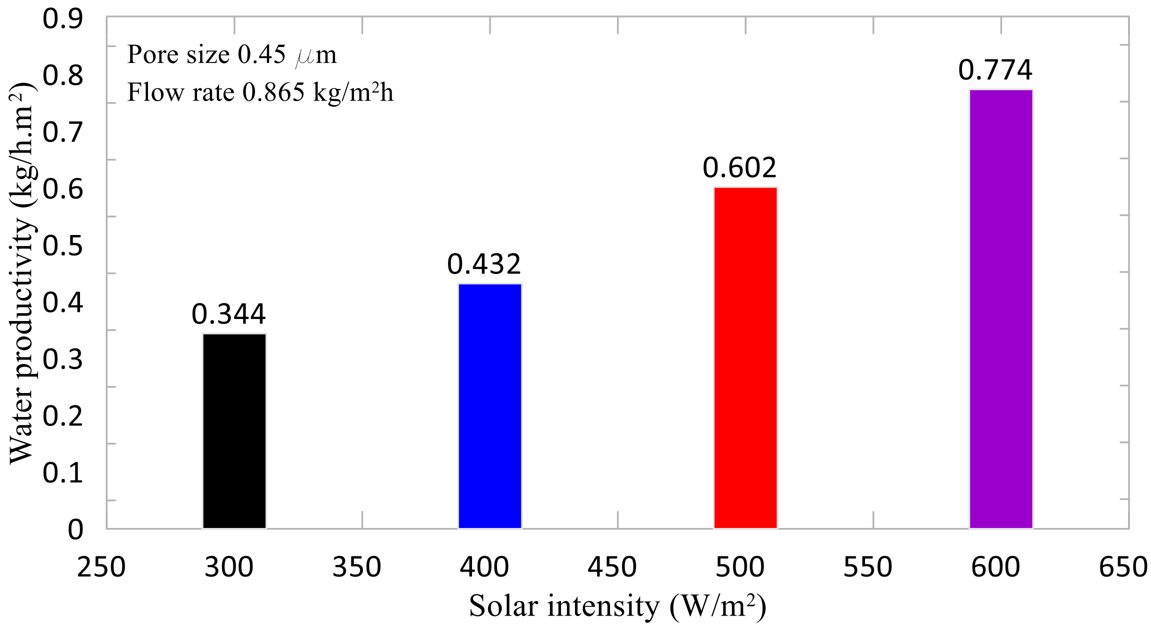

Figure (5.26): The effect of solar intensity on the water productivity for pore size 0.45 μm and supply water flow rate 0.865 kg/m^2.h.

5.4 OUTDOOR TEST RESULTS

The outdoor rig is constructed depending on the best PMD geometry obtained from the theoretical simulation and the best pore size of the membrane obtained from the indoor test. The effect of the mass flow rate of supply water on the cell temperature and the freshwater productivity is studied. The mass flow rate of supplying water to the solar panel is studied with values of 0.865, 1.104, 1.38, and 1.656 kg/m^2 h. The best mass flow rate for supplying water gives the lower cell temperature, and the maximum water is presented.As show in Appendix D.

Figure 5.27 shows the average hourly productivity of freshwater for different mass flow rates of supply water. It can be seen from the figure that the best mass flow rate of supply water that can produce about 0.208 kg/m^2 h of fresh water is at 1.656 kg/m^2.h.

Figure 5.28 shows the temperature differences between the ambient and cell temperatures for different mass flow rates. The figure shows a different trend between the previous studies, most theoretical or laboratory studies, and the current theoretical study conducted in the laboratory. All the above studies showed that increasing the amount of water supplied to PMD cells decreases the cell temperature and increases productivity. However, the current field study showed that increasing the supply water flow rate increases water productivity and cell temperature, although it is less than that of the uncooled one.

Figure 5.29 shows the difference between the evaporation and condensation layer for the mass flow rate of supply water to the cell of 0.829 kg/m^2.h. It can be seen from the figure that the maximum temperature is at the evaporation layer, followed by the condensation layer. The maximum temperature difference is at solar noon.

Figure 5.30 shows the effect of adding PMD to the PV panel cell temperature. It can be seen from the figure that there is always a temperature difference between the cooled and uncooled cells. As expected, the maximum temperature difference of 7°C is at solar noon.

Figure 5.31 shows the flow rates of supply, bleeding, and produced water; it can be seen from the figure that when the supply water was 0.829 $kg/m^2.h$ about 0.102 $kg/m^2.h$ of water is condensing as freshwater; this is about 12.3% of the total water. The rest of the water is bleeding outside the PV panel.

Figure 5.32 compares the experimental and theoretical results of the cell temperature with and without cooling. There is a little difference in the mass flow rate of supply water to the cell, the mass flow rate is 0.826 $kg/m^2.h$ for experimental work, and it is 0.865 $kg/m^2.h$ for the theoretical work. The difference between the two flow rates is that the theoretical work is achieved first, and it is difficult to get the same flow rate in the experimental work. The figure shows a good agreement between theoretical and experimental work for both cooled and uncooled cells in the first half of the day. However, after 12 pm, a divergence occurs between the theoretical and the experiment; it is believed this deviation is due to two reasons: the ambient, experimental temperature profile in the second half of the is different from that of the theoretical work. The second is the selection of the heat transfer coefficient by convection for the cell on the theoretical side needs some modification, as the divergence occurs in the period of heat loss from the cell.

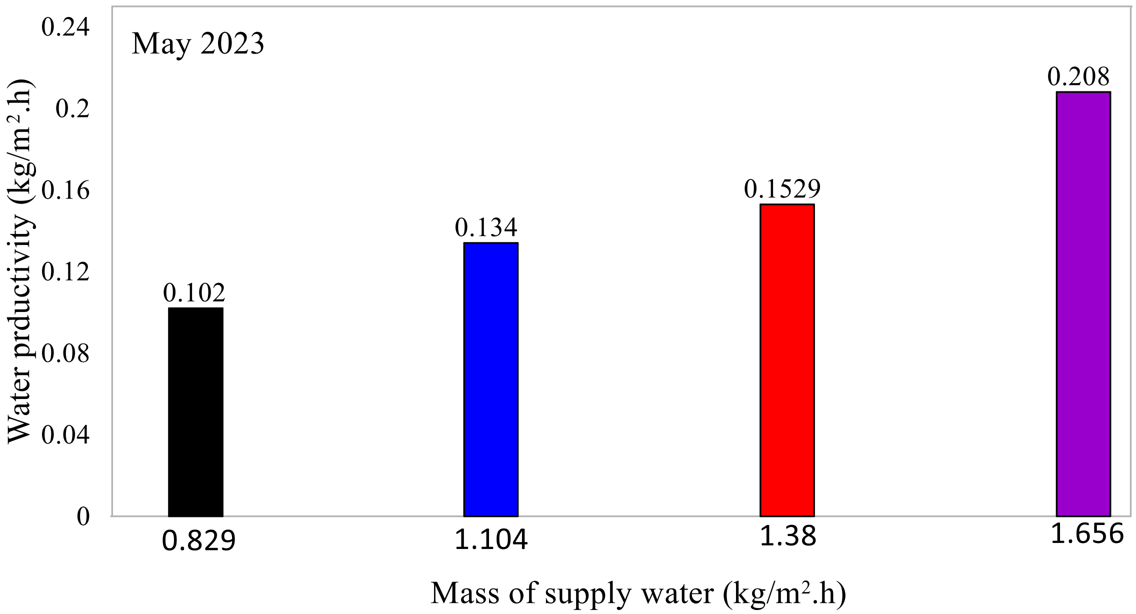

Figure (5.27): The effect of the mass flow rate of supply water on the water productivity

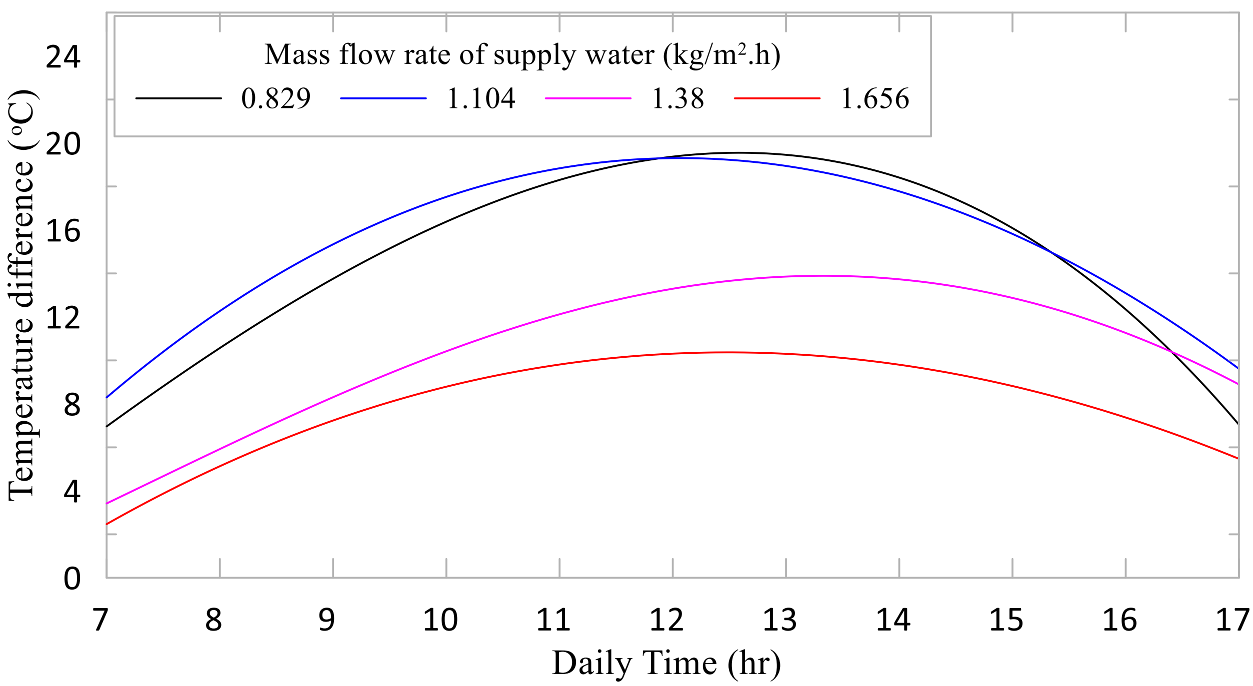

Figure (5.28): shows the effect of a mass flow rate of supply water on the temperature difference between the ambient and cell temperature

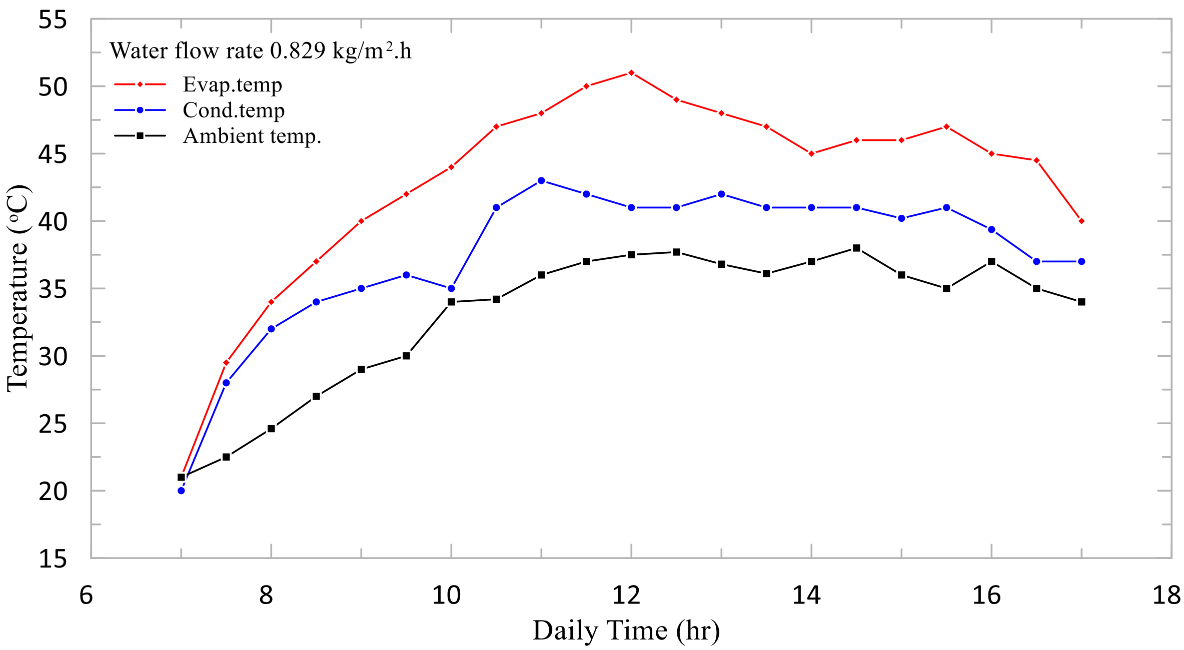

Figure (5.29): The variation of evaporation and condensing temperature with time for 0.829 kg/m^2.h mass flow rate of supply water

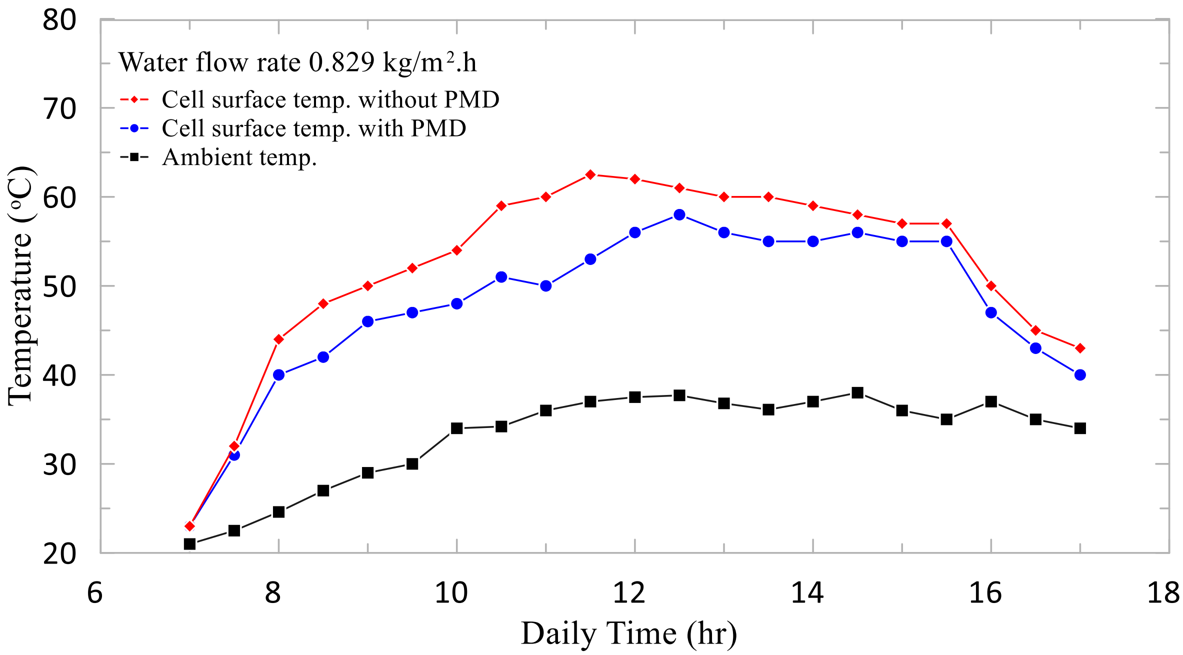

Figure (5.30): The effect of adding PMD to the PV panel on the cell temperature for 0.829 kg/m^2.h mass flow rate of supply water

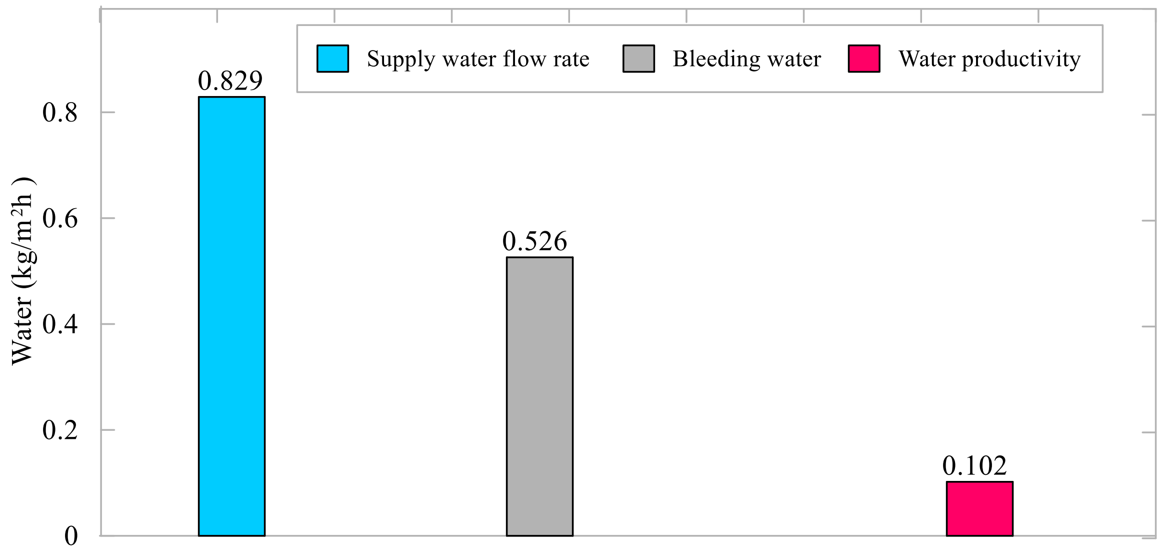

Figure (5.31): The flow rates of bleeding and produced water

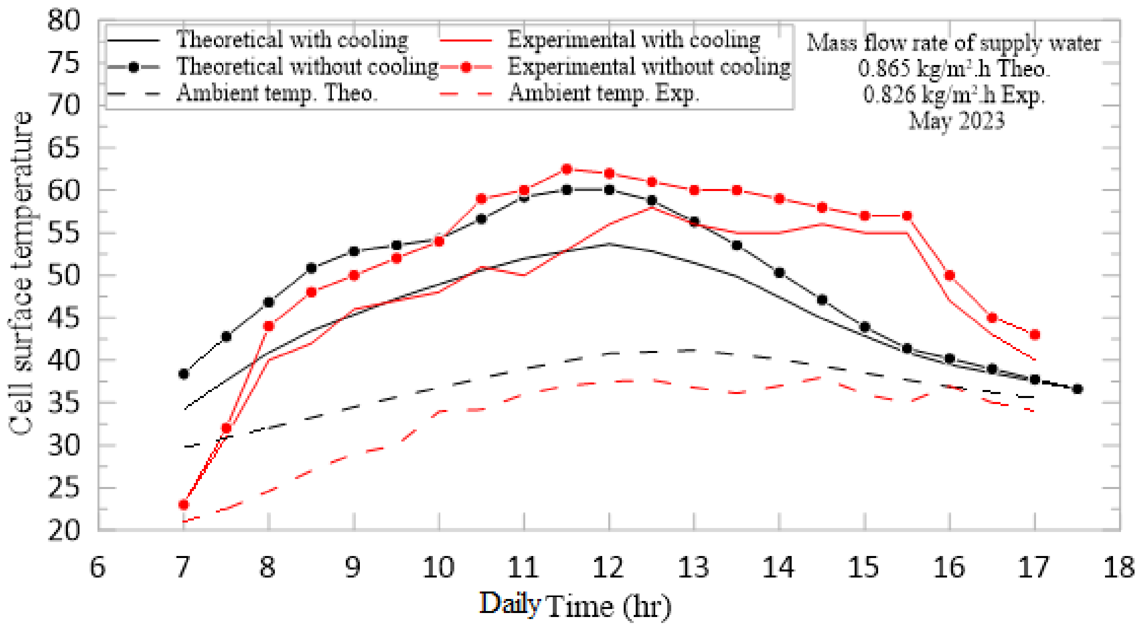

Figure (5.32): Comparison between the experimental and theoretical cell temperature with and without cooling.

5.5 THE PV CHARACTERISTIC CURVES

The characteristic curves of the panel under outdoor test are measured using Seaward PV200 Solar PV Testing Kit. The power produced by the solar panel is a function of PV voltage and PV current. The performance curve can show two curves: I- V, which is the relation between current and voltage, and the second is P-V curve which is the relation between the power generated and the current. The standard curves of the PV panel are drawn by the PV-200 either by storage data of the given panel or by introducing the PV data manually.

Figure 5.33 shows the standard, cooled, and uncooled PV panel performance curve. The figure shows that the maximum power generated by the PV panel in the standard condition is 50 W, while it decreases to 45.5 W when the cell is cooled, and the output deteriorates significantly to become 29 W by the uncooled panel; this is due to the high temperature of the cell, which is 56.4 ^{o}C for uncooled cell While it is 48 for the cooled cell and as shown in Table 5.2.

The effect of solar radiation on the I-V performance is shown in Figure 5.34. The figure shows the maximum power point (MPP) of the cooled panel; the location of the MPP changes with the daytime, as its highest value at solar noon decreases before and after this time, and the MPP is approximately equal at 11 and 13 hr.

Figure 5.35 shows the P-V curve of the solar panel at different daytime. The figure shows that the maximum power production of the cooled panel is about 45.4 W at the solar noon and reduces before and after the noon, as it is about 36.7 and 36.3 W at 11 and 13 hr, respectively.

Figure 5.36 shows the effect of daytime on the efficiencies of standard, cooled, and uncooled panels. It can be seen from the figure that.

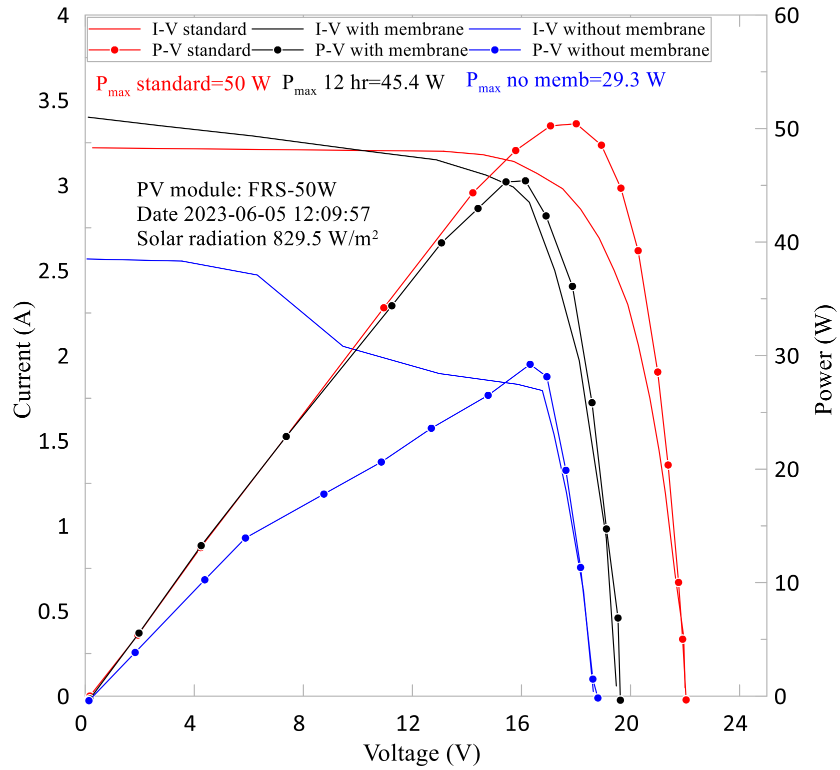

Figure (5.33): PV characteristic curves for standard, cooled, and uncooled panel.

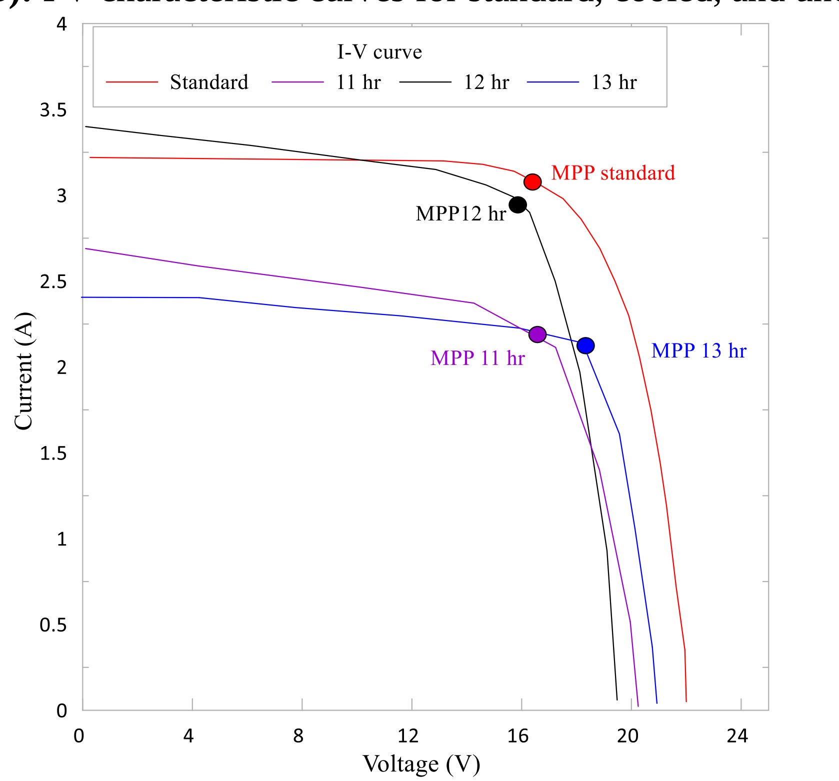

Figure (5.34): The I-V curve of the solar panel under different daytime

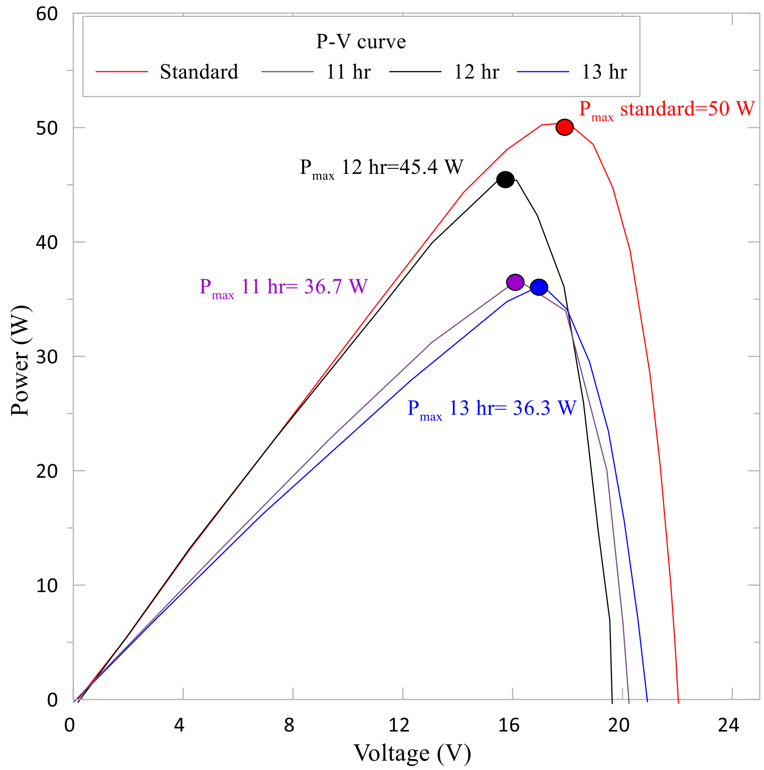

Figure (5.35): The P-V curve of the solar panel at different daytimes

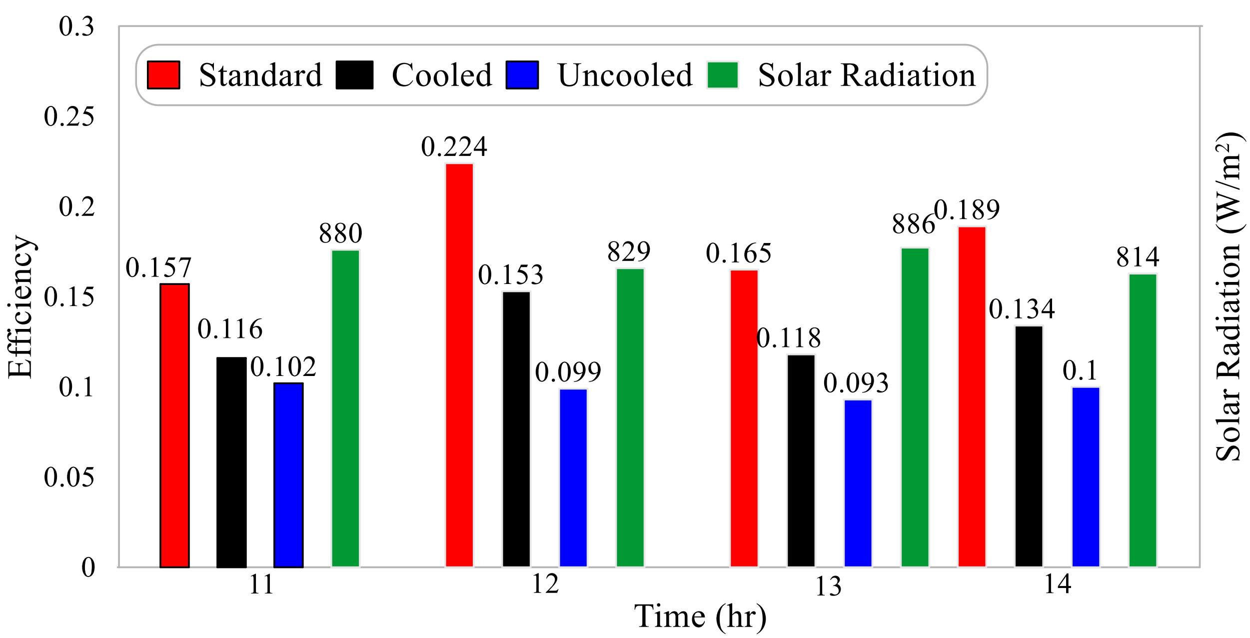

Figure 5.36 The effect of daytime on the PV panel efficiency

Table (5.2): The performance data for the cooled and uncooled panels at different daytime

The cooled panel, 2023-06-05 12:2:37					
	Measured	Nominal		Measured	
Voc:	19.9V	22V	Irr:	829.5	W/m^2
Isc:	3.08A	3.17A	Tcell:	48.08	^oC
Vmpp:	1 5.76V	18V	Ambient Temperature:	42.61	^oC
Impp:	2.92A	2.8A	Fill Factor:	75.24	%
Pmpp:	46.0W	50.4W	Irr Change:	1 8.74	%
The uncooled panel, 2023-06-05 12:09:57					
	Measured	Nominal		Measured	
Voc:	18.9V	22V	Irr:	831.4	W/m^2
Isc:	2.58A	3.17A	Tcell:	56.38	^oC
Vmpp	16.68V	18V	Ambient Temperature:	42.61	^oC
Impp:	1.81A	2.8A	Fill Factor:	61.98	%
Pmpp:	30.1 W	50.4W	Irr Change:	0.67	%
The cooled panel, 2023-06-05 11:06:52					
	Measured	Nominal		Measured	
Voc:	20.9V	22V	Irr:	825.1	W/m^2
Isc:	2.26A	3.17A	Tcell:	46.72	^oC
Vmpp:	16.93V	18V	Ambient Temperature:	42.76	^oC
Impp:	2.18A	2.8A	Fill Factor:	77.97	%
Pmpp:	36.9W	50.4W	Irr Change:	5.01	%
The cooled panel, 2023-06-05 13:01:09					
	Measured	Nominal		Measured	
Voc:	20.2V	22V	Irr:	880.3	W/m^2
Isc:	2.56A	3.17A	Tcell:	45.6	^oC
Vmpp:	16.62V	18V	Ambient Temperature:	41.68	^oC
Impp:	2.24A	2.8A	Fill Factor:	71.95	%
Pmpp:	37.1 W	50.4W	Irr Change:	4.93	%

Chapter Six

Conclusions and Recommendations

Chapter Six

Conclusions and Recommendations

6.1 CONCLUSIONS

From the three results of the three branches' work, it can be concluded that:

6.1.1 Theoretical Results

1. The best geometry of the PMD is as follows
   - A space thickness is 2.5 mm.
   - Membrane thickness of 100 μm.
   - Fin height 20 mm.
   - The number of fins is 5.
   - The best supply water flow rate is 0.865 $kg/m^2.h$.
2. The geometry of the PMD mentioned above achieved the following
   - Maximum freshwater productivity is 0.615 kg/m^2h.
   - The temperature difference between the uncooled and cooled panels is 10 ^oC.
3. The deviation between the previous and current work for the membrane coefficient is about 8%. Good agreement for the cell temperature distribution with the previous work.

6.1.2 Indoor Test

1. The best membrane pore size is 0.45 μm, which can achieve the following:

- Freshwater productivity of 0.774 kg/m^{2}h, when the solar intensity is 600 W/m^2.
- The surface cell temperature is 64 ^{o}C when the solar intensity is 600 W/m^2.

6.1.3 Outdoor Test

- Contrary to previous studies, the current study showed that increasing the supply water flow rate leads to a rise in cell temperature and increased water productivity.
- The best mass flow rate of the supply water is 0.829 kg/m^2.h, which gives a 7 ^{o}C temperature difference between uncooled and cooled cells and water productivity of 0.102 kg/m^2.h.
- The maximum solar panel efficiency is at noon, equal to 15.3% for cooled panels and 9.93% for uncooled panels.
- The efficiency of uncooled panels decreases with the increase of solar radiation.

6.2 RECOMMENDATION

1. Freshwater productivity can be increased by adding a multi-stage of PMD to the solar panel.
2. Studying the method of removing crystallization of the salt on the evaporation layer that leads to the blockage of the membrane.

References

REFERENCES

[1] Center for Sustainable Systems-University of Michigan, "Photovoltaic Energy Factsheet," *Center for Sustainable Systems, University of Michigan*, vol. CSS07-08. 2022.

[2] "Rooftop solar installation price will temporarily increase in 2022, says GlobalData." https://solarmagazine.com/2022/02/rooftop-solar-installation-price-will-temporarily-increase-in-2022-globaldata/ (accessed Dec. 24, 2022).

[3] V. J. Fesharaki, M. Dehghani, J. J. Fesharaki, and H. Tavasoli, "The Effect of Temperature on Photovoltaic Cell Efficiency," *Proceeding 1st Int. Conf. Emerg. Trends Energy Conserv.*, no. November, pp. 20–21, 2011.

[4] "Intro - Meteonorm (de)."

[5] W. Wang, "The Design and Fabrication of the Multistage-Membrane Distillation Device Integrated with Solar Cell for Simultaneous Water and Electricity Production via Sunlight Dissertation by," 2020.

[6] V. G. Gude, "Renewable Energy Powered Desalination Handbook, 1st ed. Elsevier Inc.," 2018. https://books.google.iq/books?hl=ar&lr=&id=4mpQDwAAQBAJ&oi=fnd&pg=PP1&dq=+V.+G.+Gude,+Renewable+Energy+Powered+Desalination+Handbook:+Application+and+Thermodynamics.+2018&ots=wFAcYB4gRg&sig=djC_y7OKHEf8MLg9vJj73aneF7Q&redir_esc=y#v=onepage&q=V. G. Gude%2C

[7] H. Sharon and K. S. Reddy, "A review of solar energy driven desalination technologies," *Renew. Sustain. Energy Rev.*, vol. 41, pp. 1080–1118, Jan. 2015, doi: 10.1016/J.RSER.2014.09.002.

[8] A. Gabelman and S. Hwang, "Hollow ® ber membrane contactors," vol. 159, 1999.

[9] B. W. Reed, M. J. Semmens, and E. L. Cussler, "Membrane contactors," 1995.

[10] J. Larsson, "Membrane Distillation Study of Membrane Distillation unit at the Duke Smart Home .," 2010.

[11] A. Kullab and A. Martin, "Membrane distillation and applications for water purification in thermal cogeneration plants," *Sep. Purif. Technol.*, vol. 76, no.

3, pp. 231–237, Jan. 2011, doi: 10.1016/J.SEPPUR.2010.09.028.

[12] S. Bonyadi and T. S. Chung, "Highly porous and macrovoid-free PVDF hollow fiber membranes for membrane distillation by a solvent-dope solution co-extrusion approach," *J. Memb. Sci.*, vol. 331, no. 1–2, pp. 66–74, 2009, doi: 10.1016/j.memsci.2009.01.014.

[13] M. M. Teoh and T. S. Chung, "Membrane distillation with hydrophobic macrovoid-free PVDF-PTFE hollow fiber membranes," *Sep. Purif. Technol.*, vol. 66, no. 2, pp. 229–236, 2009, doi: 10.1016/j.seppur.2009.01.005.

[14] H. Lee, F. He, L. Song, J. Gilron, and K. K. Sirkar, "Desalination with a cascade of cross-flow hollow fiber membrane distillation devices integrated with a heat exchanger," *AIChE J.*, vol. 57, no. 7, pp. 1780–1795, Jul. 2011, doi: 10.1002/AIC.12409.

[15] R. Schwantes, K. Chavan, D. Winter, C. Felsmann, and J. Pfafferott, "Techno-economic comparison of membrane distillation and MVC in a zero liquid discharge application," *Desalination*, vol. 428, pp. 50–68, Feb. 2018, doi: 10.1016/J.DESAL.2017.11.026.

[16] A. Winter, D. Koschikowski, J. Gross, F. Maucher, D. Düver, D. Jositz, M. Mann, T. Hagedorn, "Comparative analysis of full-scale membrane distillation contactors - methods and modules," *J. Memb. Sci.*, vol. 524, pp. 758–771, Feb. 2017, doi: 10.1016/j.memsci.2016.11.080.

[17] S. U. Schwantes, R. Seger, J. Bauer, L. Winter, D. Hogen, T. Koschikowski, J. Geißen, "Characterization and assessment of a novel plate and frame md module for single pass wastewater concentration–feed gap air gap membrane distillation," *Membranes (Basel).*, vol. 9, no. 9, p. 118, Sep. 2019, doi: 10.3390/membranes9090118.

[18] L. M. Camacho Makki, Adham Omer, Siddig Sabir, Hisham, "Advances in membrane distillation for water desalination and purification applications," *Water (Switzerland)*, vol. 5, no. 1, pp. 94–196, 2013, doi: 10.3390/w5010094.

[19] B. Jiao, A. Cassano, and E. Drioli, "Recent advances on membrane processes for the concentration of fruit juices: A review," *J. Food Eng.*, vol. 63, no. 3, pp. 303–324, 2004, doi: 10.1016/j.jfoodeng.2003.08.003.

[20] A. M. Alklaibi and N. Lior, "Membrane-distillation desalination: Status and potential," *Desalination*, vol. 171, no. 2, pp. 111–131, 2005, doi: 10.1016/j.desal.2004.03.024.

References

[21] J. Zhang, N. Dow, M. Duke, E. Ostarcevic, J. De Li, and S. Gray, "Identification of material and physical features of membrane distillation membranes for high performance desalination," *J. Memb. Sci.*, vol. 349, no. 1–2, pp. 295–303, 2010, doi: 10.1016/j.memsci.2009.11.056.

[22] E. Curcio and E. Drioli, "Membrane distillation and related operations - A review," *Sep. Purif. Rev.*, vol. 34, no. 1, pp. 35–86, 2005, doi: 10.1081/SPM-200054951.

[23] J. Koschikowski, M. Wieghaus, M. Rommel, V. S. Ortin, B. P. Suarez, and J. R. Betancort Rodríguez, "Experimental investigations on solar driven stand-alone membrane distillation systems for remote areas," *Desalination*, vol. 248, no. 1–3, pp. 125–131, 2009, doi: 10.1016/j.desal.2008.05.047.

[24] Y. Wang, Z. Xu, N. Lior, and H. Zeng, "An experimental study of solar thermal vacuum membrane distillation desalination," *Desalin. Water Treat.*, vol. 53, no. 4, pp. 887–897, 2015, doi: 10.1080/19443994.2014.927187.

[25] S. R. Selvi and R. Baskaran, "Solar photovoltaic-powered membrane distillation as sustainable clean energy technology in desalination," *Curr. Sci.*, vol. 109, no. 7, pp. 1247–1254, 2015, doi: 10.18520/v109/i7/1247-1254.

[26] P. Yang, Peihua Liu, Kang Chen, Qian Li, Jia Duan, Jiangjiang Xue, Guobin Xu, Zisheng Xie, Wenke Zhou, Jun., "Solar-driven simultaneous steam production and electricity generation from salinity," *Energy Environ. Sci.*, vol. 10, no. 9, pp. 1923–1927, 2017, doi: 10.1039/c7ee01804e.

[27] Li X Min X Li J Xu N Zhu P Zhu B Zhu S Zhu J "Storage and Recycling of Interfacial Solar Steam Enthalpy," *Joule*, vol. 2, no. 11, pp. 2477–2484, 2018, doi: 10.1016/j.joule.2018.08.008.

[28] E. Chiavazzo, M. Morciano, F. Viglino, M. Fasano, and P. Asinari, "Passive solar high-yield seawater desalination by modular and low-cost distillation," *Nat. Sustain.*, vol. 1, no. 12, pp. 763–772, Dec. 2018, doi: 10.1038/s41893-018-0186-x.

[29] A. Manuscript, "Energy & Environmental Science," pp. 0–15, 2018, doi: 10.1039/C8EE00220G.

[30] S. Ali and S. Aleid, "Design and Fabrication of Multi-functional Photovoltaic-Membrane Distillation-Evaporative Crystallizer for Water Desalination, Electricity Generation, Salt Crystallization and Solar Cell Cooling ." M.sc *thesis/ King Abdullah Univ. Sci. Technol. Thuwal, Kingdom*

Saudi Arab., 2019.

[31] Wang, Wenbin Shi, Yusuf Zhang, Chenlin Hong, Seunghyun Shi, Le Chang, Jian Li, Renyuan Jin, Yong Ong, Chisiang Zhuo, Sifei Wang, Peng "Simultaneous production of fresh water and electricity via multistage solar photovoltaic membrane distillation," *Nat. Commun.*, vol. 10, no. 1, Dec. 2019, doi: 10.1038/s41467-019-10817-6.

[32] G. Li and L. Lu, "Modeling and performance analysis of a fully solar-powered stand-alone sweeping gas membrane distillation desalination system for island and coastal households," *Energy Convers. Manag.*, vol. 205, no. November 2019, p. 112375, 2020, doi: 10.1016/j.enconman.2019.112375.

[33] Deng, Hongling Yang, Xiaohong "Modeling and optimization of solar thermal-photovoltaic vacuum membrane distillation system by response surface methodology," *Sol. Energy*, vol. 195, no. November 2019, pp. 230–238, 2020, doi: 10.1016/j.solener.2019.11.006.

[34] Wang, Wenbin Shi, Yifeng Zhang, Chenlin "Integrated solar-driven PV cooling and seawater desalination with zero liquid discharge," *Joule*, vol. 5, no. 7, pp. 1873–1887, Jul. 2021, doi: 10.1016/j.joule.2021.05.010.

[35] Chen, Qian Burhan, Muhammad Akhtar, Faheem Hassan Ybyraiymkul, Doskhan Shahzad, Muhammad Wakil Li, Yong Ng, Kim Choon, "A decentralized water/electricity cogeneration system integrating concentrated photovoltaic/thermal collectors and vacuum multi-effect membrane distillation," *Energy*, vol. 230, p. 120852, 2021, doi: 10.1016/j.energy.2021.120852.

[36] S. Liang, H. Zheng, X. Ma, F. Liu, G. Wang, and Z. Zhao, "Study on a passive concentrating photovoltaic-membrane distillation integrated system," *Energy Convers. Manag.*, vol. 242, p. 114332, 2021, doi: 10.1016/j.enconman.2021.114332.

[37] A. T. Diaby, P. Byrne, P. Loulergue, O. Sow, and T. Maré, "Experimental study of a heat pump for simultaneous cooling and desalination by membrane distillation," *Membranes (Basel).*, vol. 11, no. 10, 2021, doi: 10.3390/membranes11100725.

[38] A. A. B. Baloch, H. M. S. Bahaidarah, P. Gandhidasan, and F. A. Al-Sulaiman, "Experimental and numerical performance analysis of a converging channel heat exchanger for PV cooling," *Energy Convers. Manag.*, vol. 103, pp. 14–27, 2015, doi: 10.1016/j.enconman.2015.06.018.

References

[39] C. G. Popovici, S. V. Hudişteanu, T. D. Mateescu, and N. C. Cherecheș, "Efficiency Improvement of Photovoltaic Panels by Using Air Cooled Heat Sinks," *Energy Procedia*, vol. 85, no. November 2015, pp. 425–432, 2016, doi 10.1016/j.egypro.2015.12.223.

[40] A. A. Monjezi Monjezi, Alireza Abbassi Chen, Yingxue Vepa, "Development of an off-grid solar energy powered reverse osmosis desalination system for continuous production of freshwater with integrated photovoltaic thermal (PVT) cooling," *Desalination*, vol. 495, no. July, p. 114679, 2020, doi 10.1016/j.desal.2020.114679.

[41] Q. Zhao, H. Zhang, Z. Hu, and S. Hou, "A solar driven hybrid photovoltaic module/direct contact membrane distillation system for electricity generation and water desalination," *Energy Convers. Manag.*, vol. 221, no. March, p. 113146, 2020, doi: 10.1016/j.enconman.2020.113146.

[42] M. Rabie, M. F. Elkady, and A. H. El-Shazly, "Hybrid membrane distillation/high concentrator photovoltaic system for freshwater production," *Energy Reports*, vol. 8, pp. 112–119, 2022, doi: 10.1016/j.egyr.2021.11.067.

[43] U. Kumar, *Integration of Membrane Distillation and Solar Thermal Systems for Co-production of Purified Water and Heat*. 2015.

[44] H. Xu, X. Ji, L. Wang, J. Huang, J. Han, and Y. Wang, "Performance study on a small-scale photovoltaic electrodialysis system for desalination," *Renew. Energy*, vol. 154, pp. 1008–1013, 2020, doi: 10.1016/j.renene.2020.03.066.

[45] Koretsky M.D., *Engineering and Chemical Thermodynamics*, 2nd Editio. Wiley, 2012.

[46] Y. Shi Yusuf Li, Renyuan "A 3D Photothermal Structure toward Improved Energy Efficiency in Solar Steam Generation," *Joule*, vol. 2, no. 6, pp. 1171–1186, 2018, doi: 10.1016/j.joule.2018.03.013.

[47] A. Tiwari and M. S. Sodha, "Performance evaluation of solar PV/T system: An experimental validation," *Sol. Energy*, vol. 80, no. 7, pp. 751–759, Jul. 2006, doi: 10.1016/J.SOLENER.2005.07.006.

[48] Suparyanto dan Rosad (2015, *Heat Transfer book*, vol. 5, no. 3. 2020.

[49] M. Khayet, "Membranes and theoretical modeling of membrane distillation: A review," *Advances in Colloid and Interface Science*, vol. 164, no. 1–2. Elsevier B.V., pp. 56–88, May 11, 2011. doi: 10.1016/j.cis.2010.09.005.

[50] J. Li, Z. Lei, C. Li, and B. Chen, "Comments on special distillation

processes," *Korean J. Chem. Eng.*, vol. 22, no. 4, pp. 617–618, 2005, doi: 10.1007/BF02706653.

[51] C. Rectangular, M. Li, K. A. Hummer, and K. Chang, "Theoretical and Experimental Study of the" vol. 39, no. 8, pp. 1158–1166, 1991.

[52] H. C. Duong, L. Xia, Z. Ma, P. Cooper, W. Ela, and L. D. Nghiem, "Assessing the performance of solar thermal driven membrane distillation for seawater desalination by computer simulation," *J. Memb. Sci.*, vol. 542, pp. 133–142, 2017, doi: 10.1016/j.memsci.2017.08.007.

[53] J. Zhang Jianhua Li, Jun De., "Modelling of vacuum membrane distillation," *J. Memb. Sci.*, vol. 434, pp. 1–9, 2013, doi: 10.1016/j.memsci.2013.01.048.

[54] A. Alkhudhiri, N. Darwish, and N. Hilal, "Membrane distillation: A comprehensive review," *Desalination*, vol. 287, pp. 2–18, 2012, doi: 10.1016/j.desal.2011.08.027.

[55] J. Phattaranawik, R. Jiraratananon, and A. G. Fane, "Heat transport and membrane distillation coefficients in direct contact membrane distillation," *J. Memb. Sci.*, vol. 212, no. 1–2, pp. 177–193, 2003, doi: 10.1016/S0376-7388(02)00498-2.

[56] L. D. Tijing Leonard D. Woo, Yun Chul Shim., "Superhydrophobic nanofiber membrane containing carbon nanotubes for high-performance direct contact membrane distillation," *J. Memb. Sci.*, vol. 502, pp. 158–170, 2016, doi: 10.1016/j.memsci.2015.12.014.

[57] "Ethanol - Density and Specific Weight vs. Temperature and Pressure." https://www.engineeringtoolbox.com/ethanol-ethyl-alcohol-density-specific-weight-temperature-pressure-d_2022.html (accessed Oct. 09, 2022).

[58] P. Taylor, J. Mericq, S. Laborie, and C. Cabassud, "Desalination and Water Treatment Vacuum membrane distillation for an integrated seawater desalination process," no. February 2013, pp. 37–41, 2012.

[59] Z. Ding, R. Ma, and A. G. Fane, "A new model for mass transfer in direct contact membrane distillation," *Desalination*, vol. 151, no. 3, pp. 217–227, 2003, doi: 10.1016/S0011-9164(02)01014-7.

[60] C. Camperi-ginestet, "Etude de faisabilité d'un module plan intégrant distillation membranaire et collecteur solaire pour le dessalement autonome et décentralisé d'eau de mer : conception, modélisation et optimisation pour une application aux petites communautés isolées," 2019.

[61] A. O. Imdakm and T. Matsuura, “A Monte Carlo simulation model for membrane distillation processes: Direct contact (MD),” *J. Memb. Sci.*, vol. 237, no. 1–2, pp. 51–59, 2004, doi: 10.1016/j.memsci.2004.03.005.

[62] S. Srisurichan, R. Jiraratananon, and A. G. Fane, “Mass transfer mechanisms and transport resistances in direct contact membrane distillation process,” *J. Memb. Sci.*, vol. 277, no. 1–2, pp. 186–194, 2006, doi: 10.1016/j.memsci.2005.10.028.

[63] M. . Abbot, J. . Smith, and H. . Van Ness, *Introduction to Chemical Engineering Thermodynamics (in SI Units)*. 2010.

[64] W. Z. Leow, W. Z. Irwan, Y. M. Safwati, I., “Simulation study on photovoltaic panel temperature under different solar radiation using computational fluid dynamic method,” *J. Phys. Conf. Ser.*, vol. 1432, no. 1, 2020, doi: 10.1088/1742-6596/1432/1/012052.

[65] J. M. Smith, “Introduction to chemical engineering thermodynamics,” *J. Chem. Educ.*, vol. 27, no. 10, p. 584, 1950, doi: 10.1021/ed027p584.3.

[66] T. L. Bergman, A. S. Lavine, F. P. Incropera, and D. P. DeWitt, “Fundamental of Heat and Mass Transfer,” *Fluid Mech. its Appl.*, pp. 321–338, 2011.

[67] B. M. Ekman, G. Brooks, and M. Akbar Rhamdhani, “Development of high flux solar simulators for solar thermal research,” *Sol. Energy Mater. Sol. Cells*, vol. 141, pp. 436–446, Oct. 2015, doi: 10.1016/J.SOLMAT.2015.06.016.

[68] M. M. Alqurashi, R. M. Altuwirqi, and E. A. Ganash, “Thermal Profile of a Low-Concentrator Photovoltaic: A COMSOL Simulation,” *Int. J. Photoenergy*, vol., 2020, doi: 10.1155/2020/8814572.

Appendix A
Infusion Pump

Appendix A

Infusion Pump ARGUS 707 V and 708 V – Technical Data File

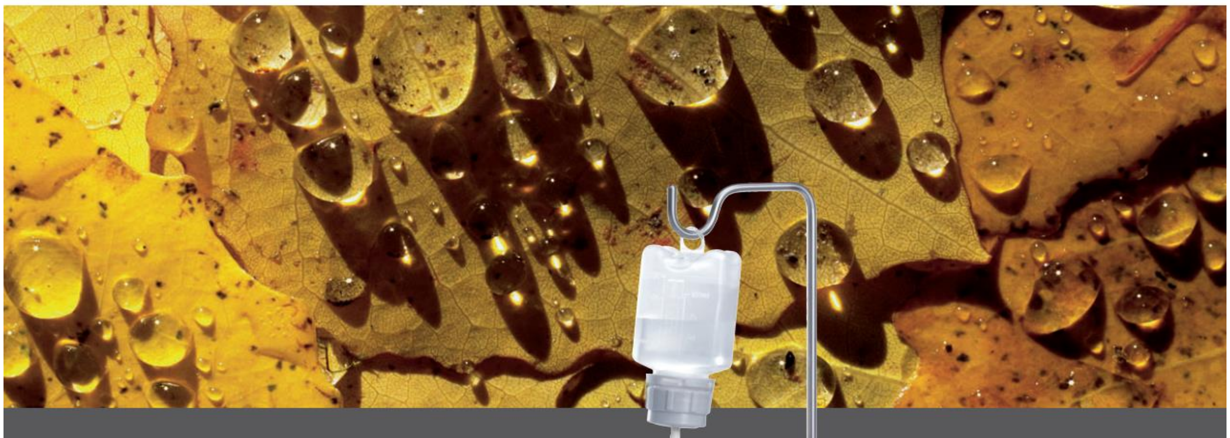

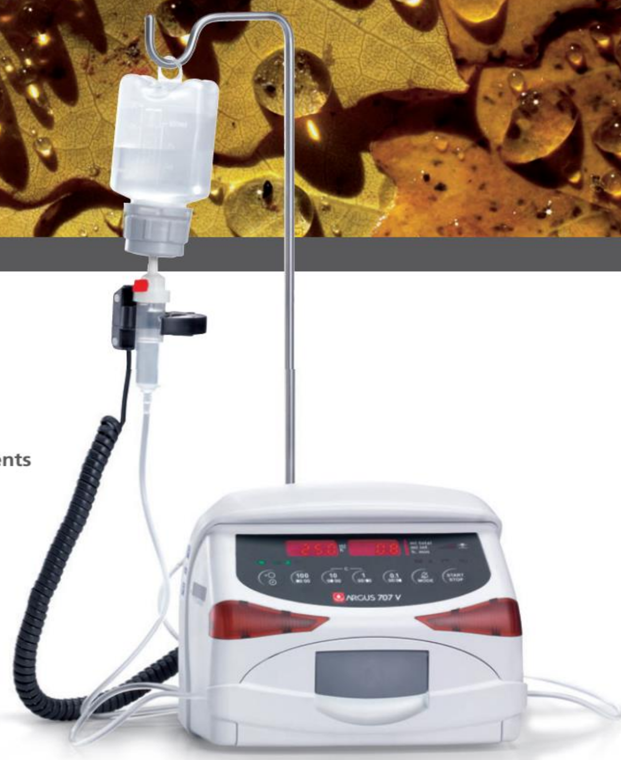

Flexible application
Intuitive to use
Safe in every way
Easily adaptable to therapeutic requirements

CODAN ARGUS AG, Oberneuhofstrasse 10, CH-6340 Baar
Phone +41 41 785 09 44, Fax +41 41 785 09 40, info@codanargus.com
www.codanargus.com

CODAN ARGUS

Infusion Pump ARGUS 707 V and 708 V

Technical data	Software 4.3X	Remarks
Performance Data		
Special application area	neonatal care, blood transfusion, nutrition	
Infusion rate	0.1 – 999.9 ml/h	in 0.1 ml/h steps
Infusion volume (VTBI)	0.1 – 999.9 ml (plus 1000 – 9999 ml)	in 0.1 ml steps (in 1.0 ml steps)
Infusion time	1 min – 99 h 59 min	in 1 min steps
Programming	rate in ml/h and volume in ml	
Automatic rate calculation	on total volume + time	total volume in ml, time in hours and minutes
Bolus Function	manual or automatic function	
Bolus rate	0.1 – 1200 ml/h	no flow interruption
Bolus volume	0.1 – 999 ml	no flow interruption
Set fill (prime) rate	0.1 – 999 ml/h	
Accuracy	± 5% depending on IV set	technical deviation < 1%
KVO - Keep Vein Open rate	0.1 – 3.0 ml/h	depending on flow rate; deactivation possible
Occlusion pressure	100 – 1000 mbar (mmHg, kPa, cmH2O, Psi)	10 adjustable steps, no flow interruption
History and Interface		
History	400 events saved in real time	graphic illustration with ARGUS *service* software
Nurse call	connectable to a staff alerting system	24 V / 0.2 A; static or dynamic; potential free change over contact
RS-232 Interface	option: galvanic isolated	connectable to Patient Data Management Systems (PDMS)
Operation		
Display	two big 4-digit LED displays	plus pictograms with LED and LED bar graph; adjustable brightness
Control Panel	4 numeric and 4 function keys	
Menu configurations	by PC	easy to use software tool ARGUS *service* ; customized configuration on request
Data-lock	all keys are lockable	
IV-Sets	version A707 V: all leading brands	configuration of four different sets
	version 708 V: dedicated Codan set	set with integrated Anti-Free-Flow system
Safety		
Pressure reduction (KVO)	automatic pressure release after occlusion	
Air Bubble Detector	single air bubbles accumulated air bubbles	adjustable between 50 – 1000 µl adjustable between 100 – 2000 µl within 8 – 64 min.
Drop Detector	10 – 65 drops / ml	adjustable, plus for transport use
Alarms	audible and visual	see list below; adjustable volume
Medication library	160 pre-programmed plus 32 user specific	listed and displayed
Power Supply		
Battery	NiMH	maintenance free
Battery operation	5 h @ 25 ml/h	
Battery charge time	16 h	
Mains power supply	230 VAC ±10%, 50 – 60 Hz ;	option: 115 VAC ±10%, 50 – 60 Hz
External power supply	20 VDC / 0.3 A	
Power consumption	12 VA maximum	
Product Specification		
Dimensions	190 x 160 x 130 mm (W x H x D)	excluding clamp
Housing	ASA	high performance plastic
Operating temperature	5° – 40° C	
Medication temperature	18° – 30° C	
Relative humidity	20 – 90% no condensation	
Weight with battery	2.0 kg	
Conformity		
IP-Protection	IPX2	protected against dripping, 15° tilted
Protection class	II	
Applied part	Type CF	
MDD classification	IIb	
Regulations + Electrical Safety	EN 60601 (-1-1 / -1-4 / -2-24)	
Electromagnetic compatibility	EN 61000-3 (-2 / -3), EN60601-1-2	
Certification	CE 0120	CODAN ARGUS AG: ISO 9001, ISO 13485, Directive 93/42/EEC
Optional Accessories		
Docking Stations	A100 for 3 infusion or A60 for 2 infusion pumps (plus combinations with syringe pumps)	version M: interface for barcode, staff alert and data transfer version P: power supply only
Fixation systems	multifunctional clamps	to be used on ceiling pole or standard rail systems
IV-Stand	two pole system with extra stability	allows mounting of one A100 and one A60 docking station
Barcoding	barcode reader and label software	to be used with docking stations A100 M or A60 M
Software	ARGUS*fluid*	fluid management system

Alarms and pre-alarms: audible and visual
occlusion upstream - downstream / air bubble / drops missing / too many drops / container empty / end of infusion / stand-by / low battery – empty battery / service / technical failure

Display
flow rate / infused volume / volume to be infused / volume balance / infusion time / remaining time / pressure bar graph / battery capacity / occlusion level / medication name

A707 V: Ref.No. 18.1110 (230 VAC) / 18.1111 (115 VAC)
A708 V: Ref.No. 19.1110 (230 VAC) / 19.1111 (115 VAC)

Marketed by

Appendix B

Calibration of the Thermocouples

Appendix B

The thermocouples and the instruments were calibrated before being used for measurement. The thermometers were calibrated using four standard Points, namely, the boiling and freezing point of water, which is equal to 100 and 0 ℃, respectively. The boiling point of methanol and ethanol is 65 and 78°Crespectively

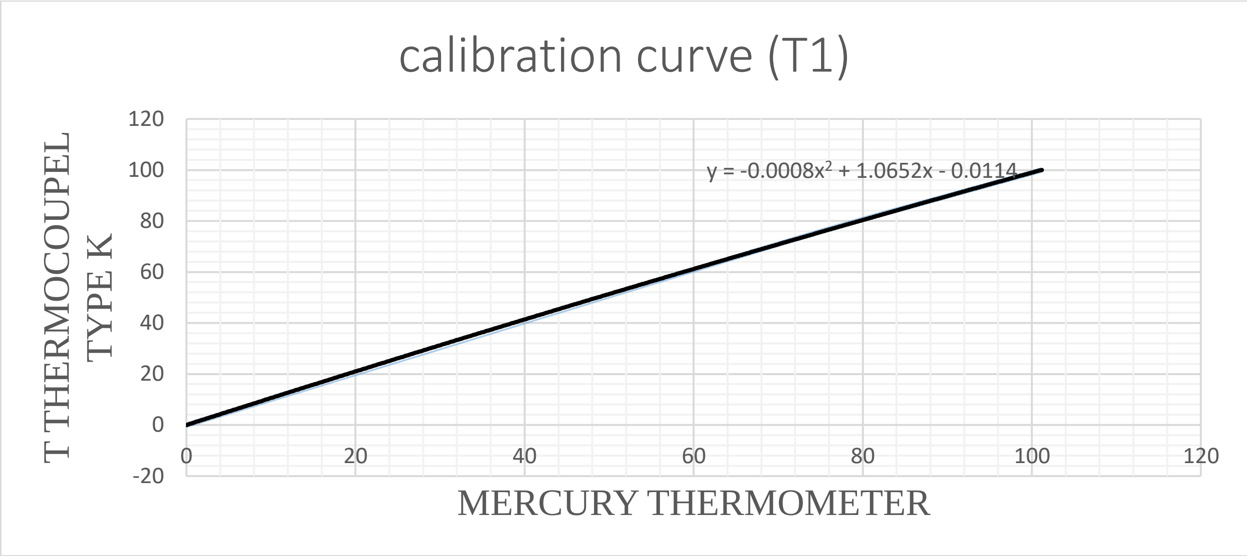

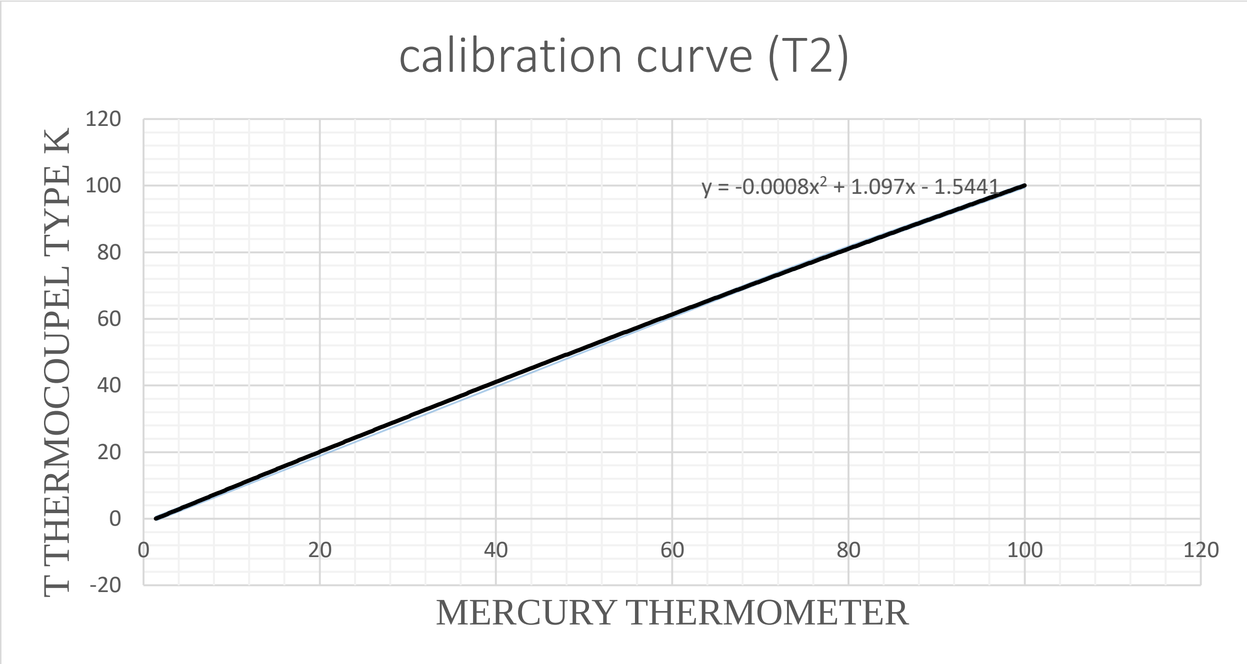

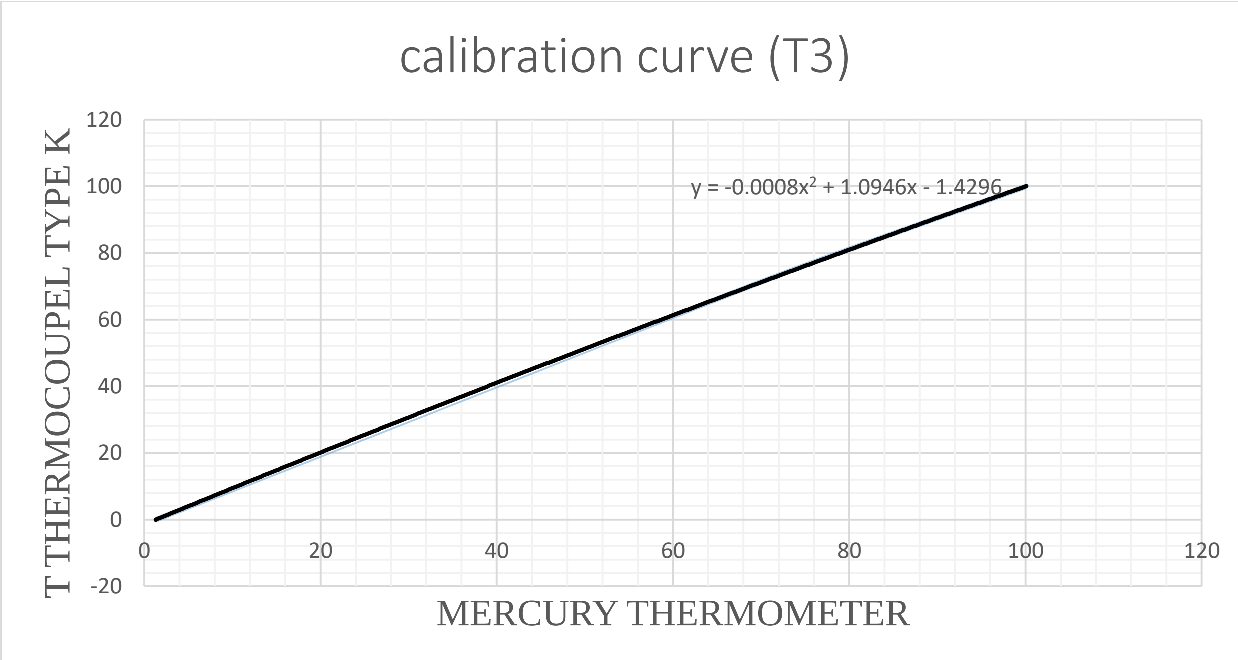
calibration curve (T3)
y = -0.0008x² + 1.0946x - 1.4296
T THERMOCOUPEL TYPE K
MERCURY THERMOMETER
120
100
80
60
40
20
0
-20
0
20
40
60
80
100
120

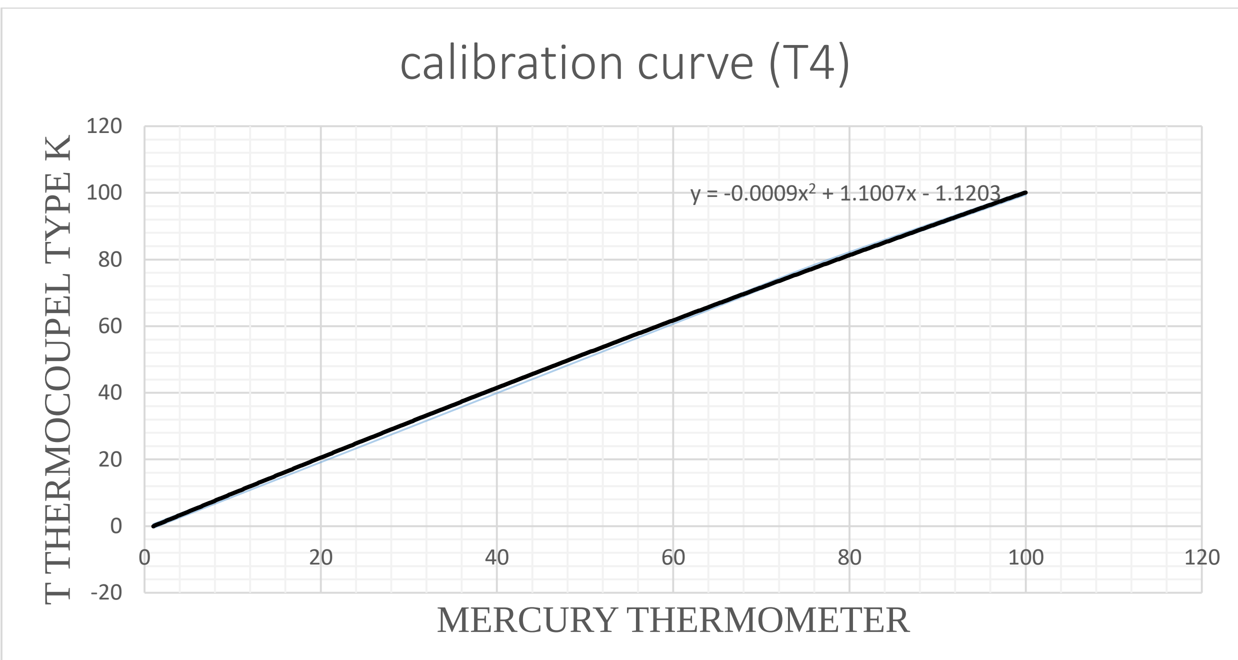
calibration curve (T4)
y = -0.0009x² + 1.1007x - 1.1203
T THERMOCOUPEL TYPE K
MERCURY THERMOMETER
120
100
80
60
40
20
0
-20
0
20
40
60
80
100
120

Appendix C
Error analysis

Appendix C

```
u_I=0.01[amper]
I=2.8[amper]
U_v=0.01[volt]
V=18[volt]
G=1000[W/m^2]
u_G=0.05[w/m^2]
A=(54*67)*0.0001
eta=(I*V)/(G*A)
u_eta=uncertaintyof(eta)
u_t=0.022
t[1]=321[k]
t[2]=318[k]
a1=11.6832
b=3816.44
c=-46.13

(p[1])=exp(a-b/(c+t[1]))
(p[2])=exp(a-b/(c+t[2]))

u_p1=uncertaintyof(p[1])
u_p2=uncertaintyof(p[2])
```

Unit Settings: SI C kPa kJ mass deg

Variable±Uncertainty	Partial derivative	% of uncertainty
η = 0.1393±0.0005035		
G = 1000±0.05 [W/m^2]	$\partial\eta/\partial G$ = -0.0001393	0.02 %
I = 2.8±0.01 [amper]	$\partial\eta/\partial I$ = 0.04975	97.62 %
t_1 = 321±0.022 [K]	$\partial\eta/\partial t_1$ = 0	0.00 %
t_2 = 318±0.022 [K]	$\partial\eta/\partial t_2$ = 0	0.00 %
V = 18±0.01 [volt]	$\partial\eta/\partial V$ = 0.007739	2.36 %
p_1 = 0.00000134±1.489E-09 [bar]		
G = 1000±0.05 [W/m^2]	$\partial p_1/\partial G$ = 0	0.00 %
I = 2.8±0.01 [amper]	$\partial p_1/\partial I$ = 0	0.00 %

t_1 = 321±0.022 [K]	$\partial p_1 / \partial t_1$ = 6.770E-08	100.00 %
t_2 = 318±0.022 [K]	$\partial p_1 / \partial t_2$ = 0	0.00 %
V = 18±0.01 [volt]	$\partial p_1 / \partial V$ = 0	0.00 %

p_2 = 0.00000115±1.306E-09 [bar]

G = 1000±0.05 [W/m^2]	$\partial p_2 / \partial G$ = 0	0.00 %
I = 2.8±0.01 [amper]	$\partial p_2 / \partial I$ = 0	0.00 %
t_1 = 321±0.022 [K]	$\partial p_2 / \partial t_1$ = 0	0.00 %
t_2 = 318±0.022 [K]	$\partial p_2 / \partial t_2$ = 5.937E-08	100.00 %
V = 18±0.01 [volt]	$\partial p_2 / \partial V$ = 0	0.00 %

No unit problems were detected.

A = 0.3618	$a1$ = 11.68	b = 3816	c = -46.13
η = 0.1393	G = 1000 [W/m^2]	I = 2.8 [amper]	p_1 = 0.00000134 [bar]
p_2 = 0.00000115 [bar]	t_1 = 321 [K]	t_2 = 318 [K]	u_η = 0.0005035
u_G = 0.05 [W/m^2]	u_I = 0.01 [amper]	u_{p1} = 1.489E-09	u_{p2} = 1.306E-09
u_t = 0.022	U_v = 0.01 [volt]	V = 18 [volt]	

No unit problems were detected.

Arrays Table: Main

	p_i [bar]	t_i [K]
1	0.00000134	321
2	0.00000115	318

Appendix D

time	evap	cond	T_A
7	21	20	21
7.5	29.5	28	22.5
8	34	32	24.6
8.5	37	34	27
9	40	35	29
9.5	42	36	30
10	44	35	34
10.5	47	41	34.2
11	48	43	36
11.5	50	42	37
12	51	41	37.5
12.5	49	41	37.7
13	48	42	36.8
13.5	47	41	36.1
14	45	41	37
14.5	46	41	38
15	46	40.2	36
15.5	47	41	35
16	45	39.37	37
16.5	44.5	37	35
17	40	37	34

time	T_A	t with cooling	t_cot
7	21	23	23
7.5	22.5	31	32
8	24.6	40	44
8.5	27	42	48
9	29	46	50
9.5	30	47	52
10	34	48	54
10.5	34.2	51	59
11	36	50	60
11.5	37	53	62.5
12	37.5	56	62
12.5	37.7	58	61
13	36.8	56	60
13.5	36.1	55	60
14	37	55	59
14.5	38	56	58
15	36	55	57
15.5	35	55	57
16	37	47	50
16.5	35	43	45
17	34	40	43

الخلاصة

الالواحُ الشمسيةِ عادةً ما تُبردُ سلباً دون الاستفادة من ميزةِ الحرارةِ المخزونةِ في الخلية. وقد وجدت هذه الدراسة احدى الطرق الفعالة التي يتم فيها تبريد الخلية بالماء و الحصول على ماء صالح للشرب من ماء التبريد.

تتكون هذه الدراسة من ثلاث خطوات للحصول على افضل معدل لكتلة ماء التبريد, و حجم مسام الغشاء لتقطير الغشاء الكهروضوئي.

المرحلة الاولى عبارة عن محاكاة نظرية للنظام باستخدام برنامج كومسول 5.6, اذ تم دمج لوح شمسي 160×160 ملم مع وحدة الغشاء الكهروضوئي للتقطير الذي يتكون من سبعة طبقاتٍ, الطبقة الاولى والاخيرة من الالمنيوم, شبكتان من البوليمرات, وغشاء نافر من الماء, طبقة محبة (مبخر) , و, طبقة محبة (**مكثف**). تمت دراسة سمك الفراغ, وسمك الغشاء, وارتفاع الزعانف, وعدد الزعانف, و درجة حرارة الماء الداخل لإيجاد افضل نموذج للغشاء الكهروضوئي للتقطير.

المرحلة الثانية هي الاختبار الداخلي, الذي يتم اجراؤه على منظومة صغيرة الحجم عبارة عن لوح شمسي 165×140 ملم مع سبع طبقات لإنشاء منظومة التقطير بالغشاء الكهروضوئي. وقد تم انشاء خمس منظومات, الاولى عبارة عن لوح كهروضوئي بدون تبريد, و الاربعة الاخرى تختلف بعضها عن البعض الاخر بحجم المسام للغشاء. و تم استخدام اربعة احجام للمسام وهي:0.45,1, 3 و5 مايكرومتر. وقد اخترنا افضل حجم للمسام من خلال الاختبار الداخلي.

المرحلة الثالثة تتمثل في انشاء لوح شمسي كامل الحجم يتم دمجه مع منظومة التقطير بالغشاء الكهروضوئي لغشاء حجم مسامه 0.45 مايكرومتر.و تم اختبار الوحدة الخارجية تحت معدلات تدفق كتلية مختلفة لماء التبريد. تم استخدام برنامج ميتينورم الاصدار الثامن لاختيار بيانات الطقس.

وتبين من خلال هذه الخطوات التي قمنا بها ايجاد افضل اداء للتقطير بالغشاء الكهروضوئي عندما كانت المسافة بين التبخير والغشاء 2.5 ملم, سمك الغشاء 100 مايكرومتر, و ارتفاع الزعنفة 20 ملم, و عدد الزعانف 5. وتم تحقيق انتاجية مياه عذبة للنظام المذكور اعلاه تبلغ 0.651 كغم/م^2.ساعة. و فرق درجة الحرارة بين اللوح غير المبرد و المبرد 10 درجة مئوية. بينما وُجدَ من الاختبار الداخلي ان افضل حجم مسام للغشاء 0.45 مايكرومتر الذي ينتج مقدار 0.774 كغم/م^2.ساعة من المياه العذبة و فرق درجة الحرارة بين اللوح غير المبرد و المبرد 14 درجة مئوية عند شدة اشعاع 600 واط/م^2. من الاختبار الخارجي, و بعكس الدراسات السابقة,

الخلاصة

أظهرت الدراسة الحالية ان زيادة معدل تدفق الماء المضاف يؤدي إلى ارتفاع درجة حرارة الخلية وزيادة إنتاجية المياه. أفضل معدل تدفق للماء المضاف هو 0.829 كغم/م^2.ساعة, الذي يعطي فرق في درجة الحرارة بمقدار 7 درجة مئوية بين الخلايا المبردة وغير المبردة وإنتاجية المياه تبلغ 0.102 كغم/م^2.ساعة.اما عن الفرق بين الدراسة الحالية والدراسات السابقة ، تم تحقيق ما يعادل 8 بالمئة لمعامل الغشاء توافق جيد لتوزيع درجة حرارة الخلية بالمقارنة مع الاعمال السابقة ,إذ اظهرت هذه المقارنة بين النتائج النظرية لدرجة حرارة الخلية مع و بدون التبريد عملية توافق جيد

جمهورية العراق
وزارة التعليم العالي والبحث العلمي
الجامعة التقنية الوسطى
الكلية التقنية الهندسية – بغداد

التحقق من تبرِيد الالواح الشمسية الكهرِوضوئية وتحلية المياه المالحة بالاغشية التنافذية

رسالة الماجستير المقدمة

لمجلس الجامعة التقنية الوسطى، الكلية التقنية الهندسية – بغداد، كجزء من متطلبات نيل درجة الماجستيرالتقني في تقنيات هندسة الحراريات

تقدم بها

حسين علي عبد الكريم جابر

بإشراف

د.عبدالهادي نعمة خليفة
استاذ

د. احمد جاسم الحمد
استاذ

ذو الحجة 1444

تموز 2023